UNIVERSITÀ DEGLI STUDI DI PADOVA

CISAS "G. COLOMBO"

STUDY AND DEVELOPMENT OF THROTTLEABLE HYBRID ROCKET MOTORS

Ph.D. School STMS

Space Sciences, Technologies and Measurements

Curriculum: Sciences and Technologies for Aeronautics and Satellite Applications (STASA)

head of ph.d. school:

Prof. Giampiero Naletto

supervisor:

Eng. Francesco Barato, Ph.D.

co-supervisor:

Prof. Daniele Pavarin

ph.d. student:

Alessandro Ruffin

CYCLE XXXI - 2018

Mighty oaks from little acorns grow

— Old Saying

ABSTRACT

In the last decades we are assisting to a shift of the space propulsion segment from a public business aiming at the highest performances to a privately funded one aiming to affordability. In this scenario hybrid rocket propulsive technology is very attractive and hence the interest around it is growing consistently. The characteristics that make hybrid rocket motors so attractive are simplicity, safety, low cost and reliability. Another characteristic that is often lauded when discussing hybrid rockets advantages is throttleability: the ability to modulate the performed thrust on demand, but as a matter of fact there is very little work published about it among the scientific community.

A throttleable rocket motor allows to increase trajectory efficiency (by reducing the required transfer Δv) and to perform some particular mission profiles such as soft landing. Current applications of hybrid technology are very peculiar. Among them there are sounding rockets, flying test beds, space tourism and speed world record automobiles. Most of them require throttling. Furthermore throttleability could be an interesting feature to implement on possible future applications such as launchers and in-orbit manoeuvre engines. Without throttleability hybrid rocket applications could be very limited, consequently it is paramount for a group who performs end-of-application research to have the capability to develop and investigate hybrid rockets motor throttling. Currently researchers are focused on solving the problems correlated with hybrids inherent disadvantages, maturing new methods of investigations and developing systems that rarely perform a variable thrust on demand. But in my opinion when the hybrid technology readiness will increase throttleability will be a paramount feature, if it is not already.

Hybrid rocket engines throttleability is the topic of the present research activity. This work is focused on the investigation and development of a general purpose throttleable hybrid rocket motor, in particular a 1 kN-class motor with a throttling ratio of 5:1. The engine will use high test peroxide as an oxidizer which will flow to the combustion chamber in a pressure fed fashion. The injection type will be gaseous and the hydrogen peroxide will be decomposed by means of a catalyst pack situated directly above the injection plate. The configuration downstream of the injection plate was not fixed at the beginning of the project, but it had to be a high performance and high regression rate configuration between two possible one: paraffin fuel grain and mixing post combustion chamber or swirled injection (vortex engine) and long chain hydrocarbons fuel grain. However the final dynamic throttling fire test campaign has been carried out with the second motor configuration.

In the past at University of Padova hybrid propulsion group other members studied throttleability both from a theoretical and experimental point of view, but this is the first time that dynamic throttling fire tests are carried out with a continuous thrust levels control, performed with an in house developed flow control valve. The recent availability of funds at the group gave us the possibility to develop and characterize new equipment. The tools employed during this doctoral research work are mainly experimental, the obtained results are then compared with the predictions from simplified analytical models.

Because throttling may induce moderate to severe performance losses, the first part of this thesis describes the losses associated with throttling. These considerations are made for a single circular port fuel grain that follow the Marxman power law regression rate model that is presented in chapter 2 as well. The entity of the losses depend on the throttling requirements, engine configuration and propellant formulation.

The pressure fed system is controlled by means of a flow control valve, this is a fundamental component in the feeding line of a throttleable hybrid rocket motor. The flow control valve was developed as part of the doctoral activities during this doctoral research period. The detailed design phase is discussed in chapter 3. The flow control valve is composed by valve body and actuation. The variable area cavitating venturi principle was selected for the valve body. Inside the valve a conical pointed pintle alters the throat area of a conventional venturi tube. The variable area cavitating venturi presents different advantages such as independence of the flow from the downstream pressure, uncoupling of tank and combustion chamber environments and precise flow control. The actuation controls the pintle axial position with respect to the venturi throat, an active closed control loop with a feedback on the pintle stroke guarantees the precise positioning. It is possible to implement the system with a control loop closed on the thrust but this strategy was not followed during this thesis.

The flow control valve underwent a complete characterization aimed to fully understand its behaviour and limits. The outcomes of this characterization are: characteristic curve, discharge coefficient trend, maximum allowed back pressure, cavitation instabilities peak frequencies, system rise and fall time and some transfer function points.

The flow control valve then has been integrated with the test motor, starting a series of fire test campaigns. The first step was to determine the motor behaviour for a series of discrete thrust levels in order to ascertain the motor regression rate power law and combustion chamber efficiency for a constant oxidizer mass flow. This preliminary fire test campaign was carried out for both the proposed motor configurations. Afterwards the dynamic throttling fire test campaign started, four tests were carried out. Three of them consisted in a sinusoidal wave thrust command profile to evaluate the dynamic motor behaviour with respect to a zero order model. The fourth test was the response to an impulse to evaluate the step response of the system. The experimental results are reported in chapter 4.

SOMMARIO

Negli ultimi decenni stiamo assistendo ad un cambiamento di trend nel settore dei sistemi a razzo per lo spazio. Da essere finanziato esclusivamente da organi governativi e alla ricerca delle massime performance a essere finanziato da società private che mirano a sostenibilità e convenienza. In questo scenario si inserisce agevolmente la tecnologia propulsiva ibrida e di conseguenza negli ultimi anni sta riscuotendo un rinnovato interesse. Le caratteristiche che rendono i motori a razzo ibridi così interessanti e attraenti sono semplicità, sicurezza d' utilizzo, basso costo e affidabilità. Un'altra caratteristica spesso decantata dei motori ibridi è la possibilità di modulare la spinta erogata dal motore (throttleabilità), ma di fatto il lavoro pubblicato sull'argomento è veramente limitato.

Un motore ibrido a spinta regolabile permette di aumentare l'efficienza della traiettoria di trasferimento, riducendo il salto di velocità totale richiesto (Δv), e di eseguire dei profili di missione molto particolari come per esempio il soft landing. Le applicazioni correnti della tecnologia proupulsiva ibrida sono peculiari di per se, tra loro ci sono razzi sonda, banchi di prova volanti, navicelle per il turismo spaziale e macchine da record di velocità. Molte di loro ad oggi sono dotate di controllo della spinta. Inoltre anche possibili applicazioni future come lanciatori e motori di manovra d'orbita potrebbero beneficiare della throttleabilità. Senza modulazione di spinta il range di applicazioni della tecnologia propulsiva ibrida è molto limitato, di conseguenza è fondamentale, per un gruppo di ricerca finalizzata all'applicazione, avere le capacità di sviluppare e studiare motori ibridi a spinta variabile. Attualmente i ricercatori sono focalizzati a risolvere i problemi intrinseci della tecnologia, creare nuovi metodi di analisi e misura e sviluppare sistemi che di rado richiedono una spinta modulabile. Ma nella mia personale opinione quando la maturità della tecnologia ibrida aumenterà la modulazione della spinta sarà una funzionalità fondamentale qualora non lo fosse già.

La modulazione della spinta nei motori ibridi è l'argomento principale della presente attività di ricerca. Questo lavoro è focalizzato nello studio e sviluppo di un motore ibrido multiuso a spinta variabile, in particolare questo avrà una spinta massima di 1 kN e un rapporto di spinta 5:1. Il motore utilizzerà una miscela acquosa di perossido di idrogeno ad alto titolo come ossidante, che sarà spinto verso la camera di combustione con un sistema di pressurizzazione a monte. L'iniezione nella camera di combustione sarà di tipo gassoso, l'ossidante viene decomposto cataliticamente per mezzo di un letto catalitico situato immediatamente a monte della piastra d'iniezione. A valle dell'iniettore la configurazione non è fissata, ne verranno studiate due con le quali è possibile ottenere

un'elevata efficienza e un alto regression rate: la prima consiste in un grano combustibile di paraffina e una post camera dotata di mixer, la seconda consiste in un'iniezione elicoidale che instaura un vortice all'interno della camera di combustione e un grano in idrocarburi a lunga catena, possibilmente polietilene ad alta densità. Ad ogni modo la campagna di test a spinta modulabile di continuo è stata effettuata con la sola seconda configurazione.

In passato al gruppo di propulsione ibrida dell'Università degli Studi di Padova altri ricercatori hanno studiato la throttleabilità sia da un punto di vista teorico che sperimentale, ma questa è la prima volta che dei test dinamici a spinta variabile con un livello continuo di discretizzazione vengono effettuati, e sono effettuati grazie ad una valvola che è stata sviluppata interamente "in casa" durante questa tesi. Questo è anche merito della recente disponibilità di fondi presso il gruppo per lo sviluppo di nuovo equipaggiamento. I metodi utilizzati in questo progetto di dottorato sono prevalentemente sperimentali, i risultati ottenuti sono ad ogni modo comparati con quelli provenienti da modelli analitici semplificati.

Poiché la modulazione della spinta potrebbe introdurre nei motori ibridi una più o meno grave riduzione delle performance, la prima parte della tesi analizza queste penalità. Le considerazioni fatte ipotizzano un grano combustibile a porta singola e circolare i cui consumo segue la legge esponenziale di Marxman per la regressione superficiale. Questo modello è presentato nel capitolo 2. La gravità delle perdite di performance dipende dal rapporto di spinta richiesto, dalla configurazione della camera di combustione e dalla formulazione propellente adottata.

Il sistema di alimentazione ossidante è controllato grazie ad una valvola di controllo di flusso, componente fondamentale in una linea fluidica per motori ibridi a spinta modulabile. Questa valvola è stata sviluppata interamente come parte del progetto di dottorato. I dettagli del design sono presentati nel capitolo 3. La valvola di controllo di flusso è costituita da corpo valvola e attuazione. Per la realizzazione del corpo valvola è stato sfruttato il principio del venturi cavitante ad area variabile, questo consiste in un classico tubo di venturi in cui l'area di gola è variata grazie ad una spina a punta conica a posizione regolabile. Il venturi cavitante ad area variabile presenta molti vantaggi tra cui l'indipendenza della portata dalla pressione a valle, il disaccoppiamento della camera di combustione dal serbatoio e la precisione di controllo della portata. L'attuazione della valvola controlla la posizione della spina rispetto alla gola del venturi. Un loop di controllo chiuso con un feedback sulla posizione permette il posizionamento preciso della spina. É possibile effettuare una chiusura del loop di controllo anche sulla spinta, tuttavia questa strategia non viene seguita nel presente lavoro.

La valvola di controllo di flusso è stata sottoposta ad una completa caratterizzazione. I risultati ottenuti con la caratterizzazione sono: la curva caratteristica, l'andamento del coefficiente di scarica, la contropressione massima accettabile, l'andamento delle

frequenze di picco della cavitazione con la pressione operativa e alcuni punti della funzione di trasferimento tra portata richiesta e portata ottenuta.

Successivamente all'integrazione della valvola col motore una serie di campagne sperimentali cominciò. Il primo passo è stato caratterizzare il comportamento del motore per le due configurazioni proposte per diversi livelli di spinta, mantenuta costante durante i singoli test in modo da poter stabilire la legge di regressione del combustibile e l'efficienza del motore. Successivamente la campagna di test di modulazione di spinta dinamica è stata condotta. Questa consisteva in quattro test, i primi tre rappresentano la risposta del sistema ad un comando ad onda sinusoidale, in modo tale da comparare i risultati con quelli aspettati da un modello di ordine zero. Il quarto test rappresentava la risposta del sistema ad un impulso rettangolare per determinare il tempo di salita e discesa della risposta. I risultati di queste campagne sperimentali sono riportati nel capitolo 4.

CONTENTS

LIST OF FIGURES

LIST OF TABLES

ACRONYMS

ADV   Ascending and descending vehicle

AMROC American Rocket Company

ATP   Ablative thermal protections

CAD   Computer aided design

CEA   Chemical Equilibrium and Applications

CFD   Computational fluid dynamic

CFG   Catalytic Fuel Grains

CV   Cavitating venturi

FCV   Flow control valve

FFT   Fast Fourier Transformation

FKM   Fluorocarbon monomer

FPGA   Field programmable gate array

HAST   High Altitude Supersonic Target

HDPE   High density polyethylene

HP   Hydrogen peroxide

HRM   Hybrid rocket motor

HTP   High test peroxide

HTPB   Hydroxyl-terminated polybutadiene

IRFNA Inhibited red fuming nitric acid

JPL   Jet Propulsion Laboratory

LMDE   Lunar module descent engine

LOX   Liquid oxygen

LRM   Liquid rocket motor

MABP   Maximum allowed back pressure

MEOP   Maximum estimated operative pressure

MON   Mixed oxides of nitrogen

PMMA Polymethyl methacrylate

PWM   Pulse width modulation

RFNA   Red fuming nitric acid

RTV   Room temperature vulcanizing

SRM   Solid rocket motor

VACV   Variable area cavitating venturi

VTVL   Vertical take-off vertical landing

NOMENCLATURE

A	Area
$a, a^I, a^{II}, a^{III}, a^{IV}$	Marxman law coefficient and exponent
B	Blowing coefficient
C_D	Discharge coefficient
C_f	Friction coefficient
C_{f0}	Friction coefficient without blowing
c	Specific heat
c^*	Characteristic velocity
c_p	Constant pressure specific heat
D	Diffusion coefficient, Diameter
d	Diameter
F	Force
f	Frequency
G	Specific flux
H	Transmission ratio
h	Enthalpy
I_{sp}	Specific impulse
L	Length
L_v	Latent heat of vaporization
m	Marxman power law length exponent
$\dot{m}$	Mass flow
n	Marxman power law flux exponent
o/f	Oxidizer to fuel ratio
p	Pressure
$\dot{q}$	Heat flux
R	Radius
r	Radius
$\dot{r}$	Regression rate
S_Φ	Source/Sink for the variable Φ
SN_g	Geometric swirl number
T	Thrust, Temperature, Torque
TR	Throttling ratio
t	Time
v	Velocity

x	Pintle stroke, fuel grain axial coordinate
α	Half pintle apex angle or cone apex angle
λ	Thermal conductivity
μ	Viscosity
ρ	Density
τ	Shear stress
Subscript	
0	Total or stagnation variables
c	Relative to cavitation
cat	At or due to the catalyst bed
cc	Relative to the combustion chamber
cond	Conductive
dry	Without lubricant of fuel/oxidizer
down	Downstream conditions often referred to the cavitating venturi throat
e	In a boundary layer referred to the edge of the boundary layer
fin	Final condition, after burning
flame	At the flame sheet
$f, fuel$	Relative to the combustion fuel
fr	Friction
in	Initial condition, before burning
inj	At or due to injection
loss	Referred to a loss
ox	Relative to the oxidizer
p	Fuel grain port
sat	Saturated fluid conditions
th	Cavitating venturi throat, nozzle throat
tot	Total
up	Upstream conditions often referred to the cavitating venturi throat
wall	at the wall, generally fuel grain wall

INTRODUCTION

Hybrid rocket motors are one of the three existent chemical rocket propulsive technologies: solid, liquid and hybrid. This classification type is defined by the physical phase to which the chemical reactants are stored in the rocket motor. In a solid rocket motor (SRM[1]) the fuel and oxidizer are in a solid form, usually an ammonium perchlorate based oxidizer is finely mixed along with aluminium powder in a polymeric matrix (generally HTPB[2]). This mixture is cast inside the combustion chamber to form the propellant grain. In a liquid rocket motor (LRM[3]) both fuel and oxidizer are in liquid form. But in general it is possible to include in this category also those motors which use gaseous and gelled reactants. With LRMs there are many possible fuel and oxidizer combinations which lead to a different propellant formulation. The reactants are generally stored in separate tanks and are injected in the combustion chamber using a feeding system. A hybrid rocket motor HRM[4] is defined as a rocket engine having one of the reactants stored in the liquid form inside a tank and the other reactant stored in solid phase inside the combustion chamber. The most common HRM configuration employs a liquid oxidizer and a solid fuel. This is particularly true since it led to define "reverse hybrids" those motors that employ a liquid fuel and a solid oxidizer. Reverse hybrids are not commonly used because the available solid oxidizers are fare less energetic than the liquid ones. An exception to this are the cryogenic solid oxidizers which in turn represent an intense technical challenge because of the storage inside of the combustion chamber. Moreover the range of available liquid oxidizers is much wider then the one fore the solid ones. Because of technical challenges, availability and poorer performances no particular advantage comes from the use of reverse hybrids. Figure 1.1 shows a typical HRM configuration. Here the

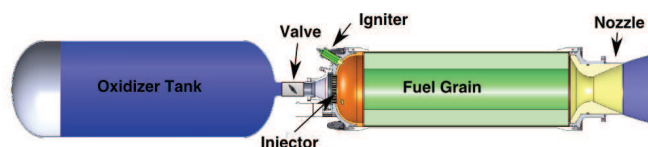Figure 1.1: A typical hybrid rocket motor configuration: it consists of pressurized tank, flow control valve, combustion chamber and nozzle.

liquid oxidizer is stored in a pressurized oxidizer tank. Oxidizer tank and combustion chamber are connected by means of a fluidic line, which in this case consists of a valve

---

1 Solid rocket motor
2 Hydroxyl-terminated polybutadiene
3 Liquid rocket motor
4 Hybrid rocket motor

and an injection plate. The fuel grain is stored inside the combustion chamber and the motor case walls are protected by means of ablative thermal protections (ATP[5]). At the aft end of the combustion chamber the nozzle converts the propellant enthalpy inside the combustion chamber to kinetic energy which generates the thrust.

The three above described chemical propulsive technologies (hybrids, solids and liquids) have been experimentally implemented about the same time at the beginning of the twentieth century. But because hybrids represented at the time a somehow more complex, scientific and technical challenge, liquids and solids advanced in their development to the point of reaching a well consolidated technology level with their relative applications, while HRMs development was limited for most part of this time. To this day hybrid rocket motors have a technology readiness level far lower that their liquid and solid counterparts. As a consequence of this, SRM and LRM have monopolized the rocket market leaving some niece applications for hybrids.

Solid rocket motors are very simple in design, compact, require small to none launch procedures and have the highest volumetric specific impulse achievable, because of the reactants density. This makes them ideal for the realization of military weapons, sounding rockets and boosters all applications where a high volumetric specific impulse is desired. Liquid rocket motors reach the highest achievable specific impulses, their thrust can be controlled and interrupted, making them the ideal solution for launchers and high required Δv missions in general. Hybrid rocket motors are somehow an intermediate solution between liquids and solids but without having the very high volumetric specific impulse required for military applications and the high specific impulse required for a space launcher. Furthermore hybrid rocket motors were disadvantaged by the time and the political-economical scene during which the greatest advancement of rocket propulsion were carried out. This is the 50s and the 60s. In that period there was no time to deeply analyse and study the inherent problems of hybrid rocket motors an hence the other two, most promising, propulsive technologies were chosen for extensive studies and development. Hybrid technology readiness has been strongly affected by its inherent problems and the cold war political-economical scene. However the space market is changed from the cold war. Today more attention is paid toward safety, reliability, cost and greenness (environmental friendliness). Many of this aspects are covered by the hybrid technology. This led to a renewed interest in hybrid rocket propulsion because of its peculiarities and inherent characteristics.

The peculiarities of hybrid rocket propulsion lay on the diffusive flame mechanism that dominates hybrid combustion. This combustion mechanism is quite different from the solid and liquid motors mechanisms. As previously noted in a solid rocket motor, oxidizer and fuel are finely mixed, during the mixing and casting process, the relative amount between oxidizer and fuel is controlled and set to the desired value. After ignition the

---

5 Ablative thermal protections

propellant grain burns with a flame very close to the grain surface[6]. Since both oxidizer and fuel are readily available to the flame the reaction between the two is kinetically limited, i.e. it is dependent on the chemical kinetic of the reaction. With these motors the oxidizer to fuel ratio o/f is fixed and the amount of propellant mass flow depends on the combustion chambers pressure. On the other hand in a liquid rocket motor the oxidizer and fuel are injected in the combustion chamber. An injector design normally forces the two reactants together in order to maximize mixing and atomization, the oxidizer to fuel ratio o/f depends on the relative amount of reactants that enter the combustion chamber. These are controlled using a set of flow control valves (FCV[7]) that regulates the reactant flow to the combustion chamber. Once again the reactants are forced together (this time by the injection plate). With both these technologies oxidizer to fuel ratio and propellant mass flow are independent variables and can be controlled. This is no longer true for HRMs. In this case only the oxidizer mass flow to the combustion chamber can be directly controlled.
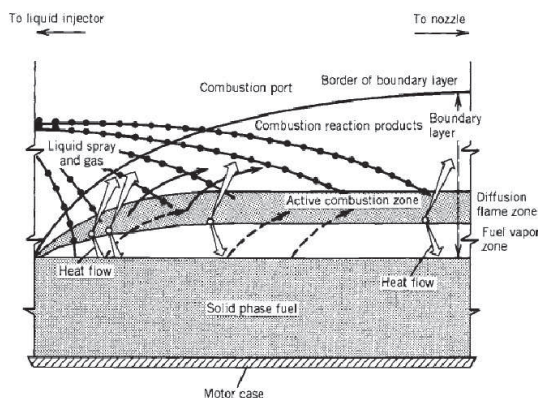
(a) Schematic from [4]

(b) Slab test from [42]

(c) Slab test from [28]

Figure 1.2: Diffusive flame mechanism (a) and visualizzation (b) & (c)

In the diffusive flame mechanism which develops inside the hybrid combustion chamber, the flame heats the surface of the fuel grain in order to sustain fuel decomposition. The sublimated fuel migrates from the surface toward the flame, on the other side of the flame oxidizing species move from the undisturbed layer region (combustion port) to the flame. When vaporized oxidizer and fuel mix an active combustion zone forms, this is the flame. Since the reactants are not premixed or forced together the reaction is limited by transport phenomena that govern the reactant migrating to the surface: diffusion. The fuel mass flow and hence the o/f, is dependent on the complex internal ballistic and combustion dynamic inside the combustion chamber. This correlation is difficult

---

6 The flame is so close to the grain surface that solid rocket motor experts, in particular at the Politechnic of Milan, speak of conductive heat when referring to the heat from the flame to the grain

7 Flow control valve

to predict and is also dependant on the motor size (including purposes of scalability)[8]. The diffusive flame mechanism is an added complexity with respect of the other two propulsive technologies. The diffusive flame mechanism is also responsible for HRMs lower performances because in many configurations reactant mixing is far from optimal. However the separation of the reactants implies also a series of intrinsic advantages. This is a description of hybrid rocket motors advantages:

SAFETY This advantage derives from the physical separation of the reactants and has many implications in terms of cost and operations. The fuel is made of inert material and unlike solid rocket grains it can be manufactured, shipped, and handled in a completely safe way. The system can be completely non-explosive if a non-explosive oxidizer is employed. Liquid oxygen (LOX[9]) is one of these. Some oxidizers classified as explosives are used in HRMs, mostly monopropellant as hydrogen peroxide solution (HTP[10]) and nitrous oxide N_2O. But it must be noted that in this case the reaction of the sole oxidizer is far less energetic than the one in which both the reactants are involved such as a SRM propellant grain. If a fuel grain cracks the combustion chamber pressure doesn't rise excessively, the oxidizer must infiltrate into the crack. On the other hand if a solid rocket grain cracks the pressure increase proportionally with the increase of the burning area, the cracked grain pressure can easily reach the MEOP[11]. If the grain cracks HRMs are less prone to catastrophic events. Much of the experimental research work that is carried out by the many universities involved in HRM development would not be possible if hybrid rocket motors were not so intrinsically safe. Let us just think of the solid rocket motors industry, most of the motor scale experimental activities are carried out by big companies with a long going history in developing this kind of engines.

RELIABILITY For what concerns the feeding section, a HRM requires just half of the components with respect to a LRM. This makes them less prone to fail and more reliable. A not perfectly cast grain, a grain with defects or a grain that cracks will be less liable to generate some unpleasant conditions inside the combustion chamber with respect to SRMs. For the reaction inside the combustion chamber is diffusion controlled, hybrid rockets are more tolerant to injection and manufacturing errors than liquids and solids. Additionally hybrid rocket designs are kept often as lean as possible in order to reduce the complexity of the system and increase reliability. It is hard to see a HRM with a complex regenerative system around the combustion chamber and fed by turbo-pumps.

---

8 The other two propulsive technologies are less prone to problem due to motor size scalability since o/f and propellant mass flow can be easily predicted.

9 Liquid oxygen

10 High test peroxide

11 Maximum estimated operative pressure

CONTROLLABLE OXIDIZER MASS FLOW It is possible, if desired, to control the oxidizer mass flow to the combustion chamber. Controlling the oxidizer mass flow have two major implications: firstly it is possible to command the thrust of the engine on demand, hence achieving throttling; Secondly the thrust can be terminated (the mission can be aborted) and, if a suitable ignition system is employed, the motor can be restarted and stopped several times. Throttleability and restartability can be achieved with a liquid system as well but, as already mentioned, the control system in a liquid motor is twice as mechanically complicate than in a hybrid system. These characteristics are difficult to reach in a solid rocket motors. SRM thrust termination systems are quite complex and the thrust can only be controlled by varying the combustion chamber pressure.

PROPELLANT VERSATILITY There are many propellant formulations available. The selection of liquid oxidizers and solid fuels accessible to a HRM designer is much wider then the one possible with solids and liquids. However the research community focuses its effort on few, selected, propellant formulations. Moreover it is possible to add to the fuel grain, high energetic particles, in order to increase flame temperature and the achievable specific impulse. This strategy is adopted commonly in solid rockets where aluminium nano-sized particles are added to the propellant grain in order to enhance the otherwise poor specific impulse. A direct advantage of propellant versatility is the possibility to tailor the fuel regression rate by using a mix of two hydrocarbons. This enables to have a fuel which is designed specifically for the application or mission.

TEMPERATURE SENSITIVITY The temperature effect on the fuel grain regression rate is small. This implies that the effects of ambient temperature on the operative combustion chamber pressure are negligible. The dependence between combustion chamber pressure and grain temperature is a concern among SRM designers because of the increase of pressure that could lead to overreach the MEOP. However there are some HRM configurations that are referred to as self pressurized that are highly sensible to a temperature variation, for the oxidizer is stored in the tank as a saturated liquid, the equilibrium pressure depends on the storage temperature. This problem can be controlled, if desired by using an in line flow control valve.

SPECIFIC IMPULSE AND VOLUMETRIC SPECIFIC IMPULSE The theoretical specific impulse achievable with an hybrid rocket is higher than the solid rocket one and it is extremely close to the one achievable with a LRM (Figure 1.3). It is worth to note that the maximum specific impulses are achieved when energy enhancing additives are included in the propellant formulation. In terms of volumetric specific impulse ($\rho\, I_{sp}$) the solid technology dominates the field, but with HRMs it is possible to have much higher $\rho\, I_{sp}$ than the one obtained with LRM. For what concern specific
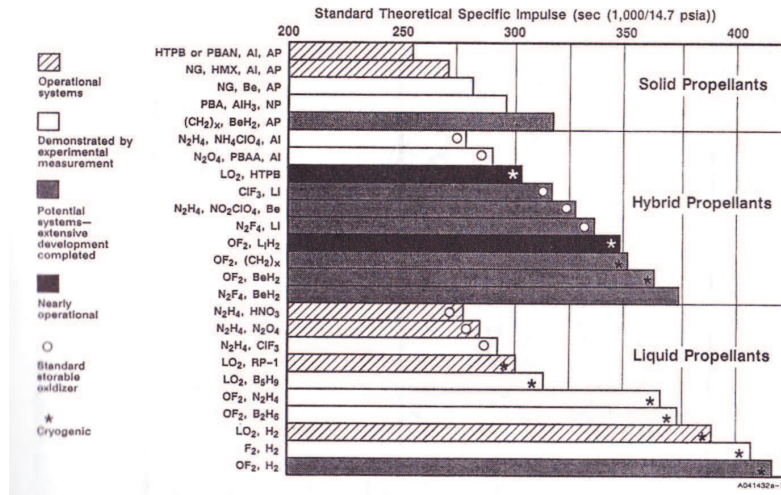
Figure 1.3: Comparison between theoretical specific impulses achievable with the three chemical propulsive technologies. [40]

impulse and volumetric specific impulse the hybrid propulsive technology is an intermediate configuration gathering together the advantages of both the traditional propulsive technologies.

LOW COST Hybrid rockets can be less expensive than traditional propulsive technologies for many reasons. Firstly, let us consider the mechanical parts composing hybrid rocket motors: the cost of an hybrid rocket must lay between the cost of a solid and of a liquid one. Secondly, the hybrid rocket present several advantages in terms of storability, handling and development. The operational costs benefits from the already discussed safety characteristics of hybrid rocket motors. A system that is non explosive and in which the reactants are hard to be put together is surely advantageous to handle during ground operations. Furthermore, the fuel grain being inert implies that the manufacturing cost are lower if compared to solid propellant manufacture. Since we do not cast an explosive mixture we do not require an ATEX manufacturing facility supplied with the proper equipment. The same concept applies, in a smaller scale, during development. It is possible to safely manufacture, assemble and test an HRM in an University environment, because of the contained safety requirements. Hybrid rocket motors reduced cost has been discussed by many authors, Matthias Grosse in [41] created a model to evaluate the manufacturing cost of a HRM, while Boardman et al. in [55] pointed out the reduced cost of the hybrid rocket booster development campaign carried out by AMROC[12].

ENVIRONMENTAL FRIENDLINESS Of the many available propellant formulation that make HRM so versatile several are green: they are friendly to the environment,

---

12 American Rocket Company

meaning no hazardous and toxic reactants and products are involved in the reaction process. In SRM ammonium perchlorate is the most used oxidizer, because it contain chloride, the fumes are not exactly green. It is true that the most green rocket propellant formulation is O_2/H_2 used in LRMs but it is not a storable formulation. One storable alternative used in liquid is hydrazine which in its undecomposed form is harmful. Hybrid rockets can be a green alternative in those applications were currently hazardous reactants are employed. At University of Padova we are proud to use hydrogen peroxide/hydrocarbons as a storable green propellant formulation.

Reactants separation and diffusive flame that make HRMs safer and cheaper, with respect to the other propulsive technologies, are also the cause for hybrids major disadvantages:

LOW REGRESSION RATE The surface regression rates found in hybrids are far lower than the ones found in solids. This is because the diffusive flame is more detached from the burning surface than the conductive flame in a SRM. A large burning area is required to achieve the desired fuel mass flow from the grain. The desired burning area with this characteristic of low regression rate often requires extreme fuel grain aspect ratios and designs. On the other hand the required web thickness is quite low, resulting in a very low fuel loading[13]. Adding up to the problem of scaling, in some hybrids configurations the regression rate decreases when the motor is scaled up. Many solutions to overcome this major problem have been proposed in the last decades and some of them are, as a matter of fact, very promising. Multiport grains
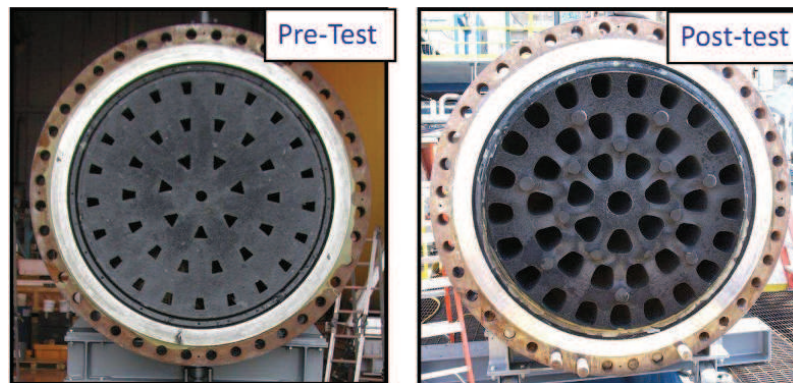
Figure 1.4: Multiport grain used in Lookheed Martin DARPA Falcon hybrid rocket

were the first solution used to overcome the extremely low regression rates. But this configuration comes several other problems like: high fuel residuals, different regression rates from port to port and structural issues requiring a structural web to hold the residual fuel slivers that forms near the end of the burn. Of course a multi

---

13 the fuel loading is defined as the portion of volume inside the combustion chamber occupied by the fuel grain

port grain is much more expensive to manufacture than a single port one. Another solution for the low regression rate problem introduced by Stanford University is the use of liquefying fuels to manufacture the fuel grain. Because of the low melting temperature a liquid layer is formed on the burning surface. Part of this layer is entrained in the main oxidizer flow due to the elevated mass fluxes. With the entrainment the inward fuel mass transfer is enhanced. Using liquefying fuels it is possible to manufacture single port grains with a reasonable aspect ratio. Moreover this fuels are less sensitive to the problems of scaling. A comprehensive review of this problematic and the proposed solutions is presented in [21].

VOLUMETRIC EFFICIENCY AND PACKAGING ISSUES Hybrid rocket motors are less flexible to be configured with respect to liquids and solids. Most part of the volume of a LRM is occupied by the propellant. This being liquid in nature can be shaped as pleased, with the proper tank design, in order to fill the required volume. The combustion chamber is relatively small. In a solid rocket the combustion chamber makes up most of the system. Since the regression rate is dependent on the combustion chamber pressure it is possible to have many propellant grain configurations with the same impulse requirements. This implying many different geometries and aspect ratios, the solid rocket is a flexible configuration as well when it comes to packaging. In a hybrid rocket the oxidizer is liquid, hence it can be stored with a packaging flexibility analogous to the liquid rocket one. The packaging issues arise when the combustion chamber design is considered. Because of the correlation between regression rate and oxidizer mass flux it is not possible to design many different fuel grain geometries that satisfy the same total impulse requirement [23]. Moreover this correlation is valid in a determined oxidizer flux range, outside which the regression rate start to be pressure dependant and far more difficult to predict. A constraint on the usable oxidizer mass flux implies that there is a limit between initial and final diameters which implies a further geometrical constraint. Normally hybrid rocket combustion chambers tend to be slender with a limit on the minimum aspect ratio achievable. This limitation goes against the possibilities unlocked by the fuel regression rate tailoring (which is possible by using a mixture of hydrocarbons). With this methodology it is possible, to some extent, to control the aspect ratio of the combustion chamber. As already noted, the dependency between oxidizer flux and regression rate also affects the volumetric efficiency of the combustion chamber. This result in a more cumbersome combustion chamber design, hence less prone to packaging flexibility. All the presented aspects lead to the conclusion that HRMs are less flexible in terms of packaging, and less prone to be integrated in a satellite system. This reduced flexibility leads to the impossibility

to design a propulsive unit that can be used on several systems, which is possible with both liquid and solid motors.

COMBUSTION EFFICIENCY AND o/f SHIFT   Unlike in solids and liquids, reactants are not intimately mixed or forced together in a hybrid rocket. This doesn't preclude the possibility to find, at the aft end of the combustion chamber, some unreacted oxidizer and fuel. Because of this incomplete diffusive combustion the achieved characteristic velocity (c^*) is quite lower than the theoretical one. Several techniques are used to complete the combustion. Between the most worth of note are the use of diaphragms, mixing plates and swirled injection [36], [16], [17]. Another cause for loss of combustion efficiency is the dependency of the oxidizer to fuel ratio from many combustion variables such as the port diameter and the oxidizer mass flow. As a consequence the o/f will shift with the burning time. Because there is only one o/f value corresponding to the maximum characteristic velocity, the maximum achievable theoretical c^* is always lower than the maximum one. This impossibility to maintain the o/f constant at the optimal value induce a loss in the combustion efficiency. The o/f shift losses can be reduced with a proper motor design.

SLOWER TRANSIENTS   The combustion chamber of a hybrid rocket is much bigger than the one of a liquid rocket with the same thrust, because it hosts the fuel grain. The internal gas volume also changes with the burning time because of fuel grain regression. This implies that the filling/emptying characteristic time is much higher with respect to LRMs. Ignition and throttling transients are slower. The slow transient nature of hybrids inhibit their use on some applications where a accurate, fast and repeatable response of the motor is required. For example motors operating in multipulse mode. Furthermore, because of flame propagation, the ignition time is lower with respect of SRMs which combustion chamber is bigger. Another problem that affects both hybrid and solid rocket motors with respect to LRMs and reduces response of the system is thermal lag[31].

Because hybrid rocket motors performances in term of specific impulse (I_{sp}) and volumetric specific impulse (ρI_{sp}) lay between solids and liquids, and because of the extensive amount of disadvantages, HRMs entry and spread in the rocket market was strongly limited. Performance penalties and low regression rate play a major role among negative attributes. As mentioned during this brief description of pros and cons there are many solutions that have been proposed by the scientific community in order to solve problem. But it must be noted that it is difficult to find a motor configuration to which each solution applies. It is equally true that all the claimed advantages are not likely possible for a single motor design. There are two promising configurations thanks to which it is possible to have a performing hybrid motor: the first one consists of an axial injection toward a high regression rate fuel and a mixing plate in the aft chamber; the second

one exploit a vortex injection and a low regression rate fuels. It is important to note, when discussing advantages and disadvantages, that some comparisons between HRMs and LRMs are overstated. It is possible to realize a regenerative cooling in a hybrid as well as it is possible to manufacture a liquid combustion chamber that is protected with ablative thermal protections. However because the fuel grain is of the same nature of an ATP, it is reasonable for the hybrid combustion chamber to be protected with this technology which will result in an overall cheaper combustion chamber. Another example of overstatement: HRMs are cheaper, simpler with respect to LRMs. Hybrids can be as complicated and expensive as they get. When designing a hybrid rocket system, it is important to consider that by introducing a new component, or an exotic solution to a disadvantage, the output design may result less reliable, complicated, less safe than a basic configuration.[14] In order to be competitive HRMs do not require any intricacy[32]. Safety, simplicity and low cost are the main advantages of an hybrid rocket motor. Such a system can be tested many times, because it is less expensive, with an higher test rate, because of the lower safety requirements, and because it is easier to test some upgrades and improvements can be made during the system commercial life. This characteristic is particularly important when the funding are limited. Because public funds are becoming meagre with time and because private funds are finalized to maximize the income, hybrid propulsive technology is becoming more and more popular for conventional space applications.

1.1 THE IMPORTANCE OF THROTTLEABILITY

Throttleability is the ability to control, or throttle, the provided motor thrust on demand. Throttleability is an aspect of hybrid rocket propulsion that is often cited when describing the propulsive technology advantages but rather present in terms of published works. Attending at the 7th European Conference for Aeronautics and Space Sciences, I had the pleasure to understand that this lack of publications about hybrid rocket motor throttleability was not a personal feeling but a generalized one. "Everyone says that hybrid rockets are throttleable but little published work can be found about it" was the expression used by a researcher during a presentation. The reason for this is that most researchers are focused on investigating the inherent problems of hybrid rocket technology (instabilities, poor performances, low regression rates, high throat erosion rates) or proposing new methods and models to aid the investigation and design of hybrid propulsive technology.

---

14 Adding an amount of oxidizer to the fuel grain formulation in order to increase the regression rate is not an appropriate solution to keep the system safe, low cost and simple because along with the regression rate the explosive class of the rocket is increased as well.

Rocket motor throttleability has a long history. In the beginning this characteristic was required by military systems in order to minimize the flight time from launcher to target or evade some defensive controls: a typical example is the boost sustain thrust profile. But an event caused throttling to move from trajectory performance enhancer to a method required to perform a peculiar mission profile: this is lunar soft landing. With the Apollo space program, which was finalized to land and return the first man to the Moon, the problem of landing on an atmosphere-less astronomical body arouse. In fact by then landings were performed by atmospheric entry which exploited the drag resistance of a blunt body (frontal heat shield) and parachute systems. Both systems exploit the atmospheric drag to decelerate the spacecraft to an acceptable impact velocity. The absence of atmosphere on the moon and the fact that the Apollo missions were manned, required the development of a new landing system: rocket powered soft landing.
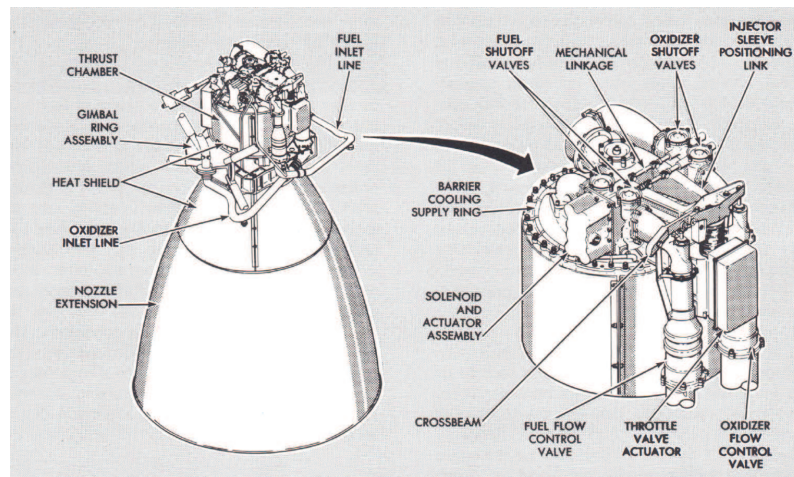
Figure 1.5: LMDE[15] flow control assembly.

The lunar module of Apollo missions used a descent engine (LMDE) [39], [13]. This is a bipropellant liquid rocket motor with a 45 kN maximum thrust and a throttling ratio of 10:1. The liquid engine employed Aerozine 50[16] and N_2O_4, this is an hypergolic mixture that was suited for a restartable low lagtime system.

Figure 1.5 shows the LMDE and in particular, on the right, the flow control assembly. This engine which is the highest example of throttleable engine, used two flow control valves (one for the fuel one for the oxidizer) and a variable area pintle injector. This throttling method that use flow control valves as well as variable area injection, as it will be explained later, is used when the pressure drop due to a fixed area injection plate cannot be accepted. The two identical valves are controlled with a single electromagnetic linear actuator, the different positioning of the FCV sleeve is realized with a crossbeam positioning link.

---

16 Aerozine 50 is a mixture of hydrazine and unsymmetrical dimethylhydrazine, the two components are present in equal concentration by weight.
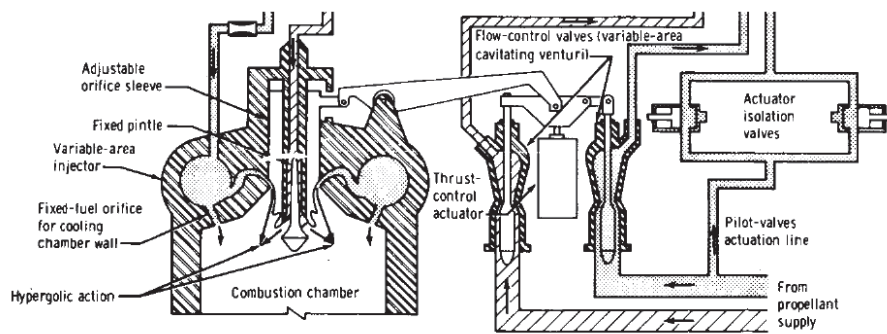
Figure 1.6: LMDE flow control scheme. [39]

For what concern hybrid rocket motors throttleability, it dates back to 1960s during studies for using hybrids rocket motors for sounding rockets, aerial target drones and tactical missiles. The first example of throttleable hybrid rocket is ONERA's LEX (Lithergol EXperimental) sounding rocket. The motor used a RFNA[17] / metatoluene diamine-nylon propellant formulation[53]. This rocket provided a boost-sustain like thrust profile, by means of a pneumatic solenoid which was actuated with a programmable timer. The achieved throttling ratio was 5:1 with a maximum thrust of 10 kN. Eight LEX sounding rockets where successfully launched, reaching an apogee of 100 km. Another relevant system that was developed in the same years is the Sandpiper aerial target drone. It used a hybrid rocket motor propelled with a mixture of nitric acid (25%) and nitrogen tetroxide (75%) for the oxidizer and a PMMA[18] fuel grain loaded with 10% of powdered magnesium. The motor was throttleable with a 8:1 throttling ratio and had a peak thrust of 2.3 kN[29],[5]. The throttling methodology used in the Sandpiper is the parallel feeding line, during the boost phase both feeding lines are open, while in the sustain phase only one feeding line provides the required oxidizer mass flow for the cruise flight. The amount of oxidizer flowing through each line is regulated by means of fixed cross-section orifices. The Sandpiper target drone flew successfully in 1968. Following the Sandpiper another aerial drone employing hybrid propulsion was developed in the USA. This was HAST[19]. This drone was an evolution of the Sandpiper, employing IRFNA[20] as oxidizer and a mixture of 80% polybutadiene-20% PMMA as fuel[18]. In this case the oxidizer flow to the combustion chamber was regulated by means of a FCV using a pintle actuated by means of a torque motor and a drivescrew. This valve was employed to have a ramp up boost phase starting from 50% of the thrust and reaching the 100% in 20 seconds. After the boost phase the valve position could be controlled manually via remote by an operator. HAST had a throttling ratio of 10:1 and a peak thrust of 5.3 kN. Program HAST concluded with a series of static fire tests but the developed propulsive system has

17 Red fuming nitric acid
18 Polymethyl methacrylate
19 High Altitude Supersonic Target
20 Inhibited red fuming nitric acid

been employed again in the new aerial target drone Firebolt [19]. Throttling has been a secondary features on other development program carried out by NASA and Lookheed Martin[10]. Recently hybrid rockets throttleability was developed and studied by several academic institutions. In 2010 Purdue University demonstrated:

- Throttle-down tests analogous to a powered vertical landing exhibited a 10:1 throttling ratio (see LMDE) with stable combustion across the entire range;

- Boost/Sustain/Boost thrust profiles representative of tactical solid rocket motors were tested with 75%, 50%, and lower sustain-to-boost chamber pressure ratios with rapid throttle-up achieved following the sustain period.

Their engine used 90% HP[21] and a wide range of fuels: PMMA, HTPB and their speciality CFG[22], which are fuel grains loaded with a catalytic material[22]. In 2010 the European funded program FP7 SPARTAN Project started [57]. This program was focused on the development of an ascending an descending vehicle that employed four hybrid rocket motors in parallel, in a clustering fashion. The motor used 87.5% HTP and HTPB, had a 10:1 throttling ratio and a maximum thrust of 1.6 kN. As an European funded program the project was a collaboration between industries and Universities coordinated by Thales Alenia-Space. The motor was manufactured by NAMMO[23],[34] the flow control valve was based on a variable area cavitating venturi and was developed by MOOG-Bradford. Both the engine and the flow control valve were tested and characterized by University of Padova's hybrid propulsion group [47],[15]. The program officially ended in 2012. In 2012 Utah State University developed and tested a closed loop controlled throttleable rocket setup using an off the shelf valve[56]. Their rocket employed N_2O-HTPB propellant formulation. Other than using N_2O as an oxidizer, which is not very common for a throttleable rocket motor they achieved stable combustion for a thrust range from 800 to 12 N. They also developed a concept for throttleable launch vehicle using the same technology[20]. Shortly after the end of SPARTAN project, the Beihang University started to develop a flow control valve that used the variable area cavitating venturi[50]. This valve is used in their experimental setup to characterize throttleable hybrid rocket motors [49]. Their engine employ 90% HTP and polyethylene as fuel. During their experimental test campaign they reached a throttling ratio of 5.32:1 and a maximum thrust of 1251 N. For what concern our research group, until this PhD work, the only dynamic throttling fire tests that were performed employed parallel feeding lines, in which the flow through each line is controlled by means of conventional cavitating venturi. This parallel feeding lines system allowed to have a boost-sustain like thrust profile.

Hybrid rocket motors throttleability advantages are:

---

21 Hydrogen peroxide
22 Catalytic Fuel Grains
23 NAMMO stands for Norwegian ammunition and is a Norwegian industry specialized in defence systems and the European leading expert in hybrid propulsive technology.
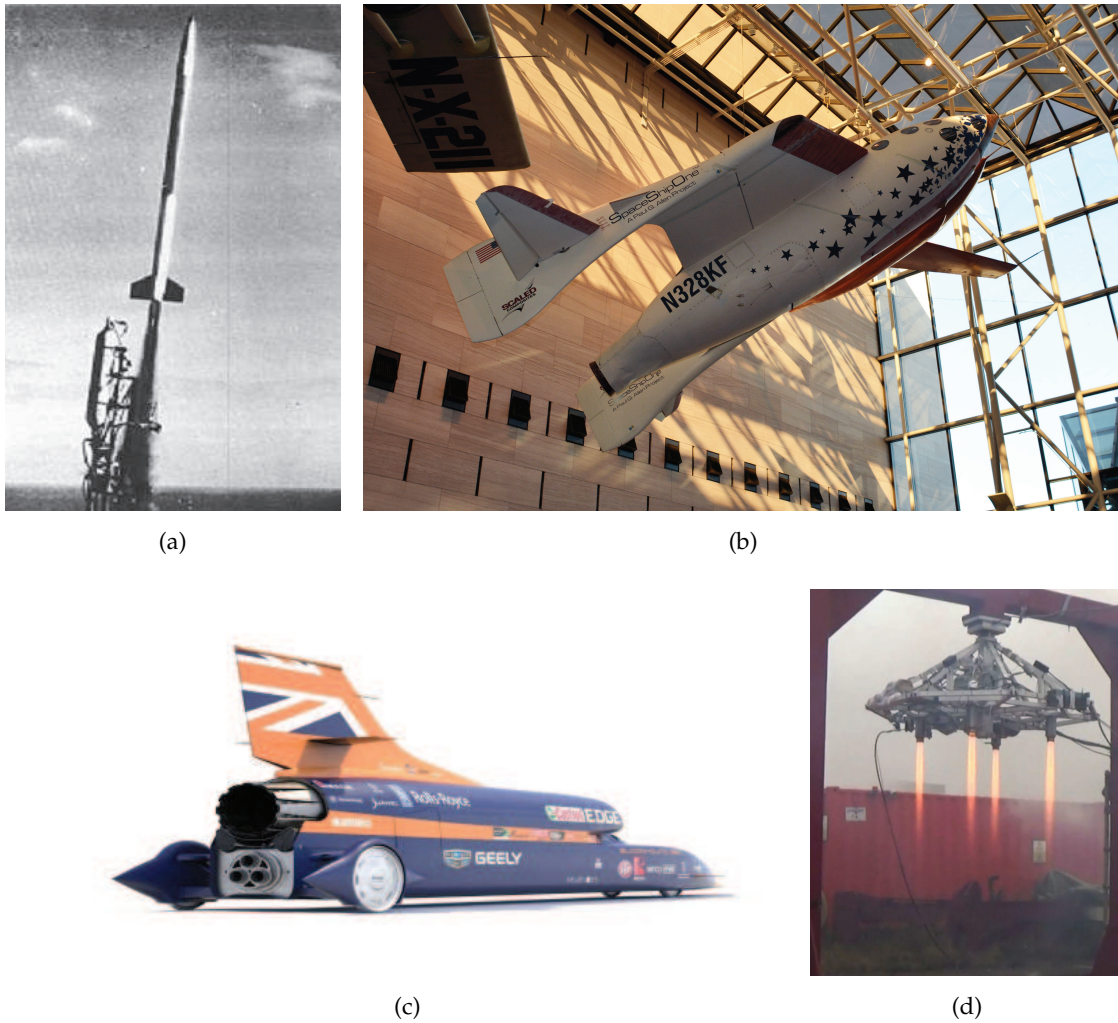
Figure 1.7: Some hybrid rocket motor applications: (a) ONERA's LEX hybrid sounding rocket, (b) Virgin Galactic's Space Ship One, (c) Bloodhound SSC and (d) Thales Alenia Space's SPARTAN Project during testing at NAMMO's.

INCREASE TRAJECTORY EFFICIENCY During ascending trajectories it is possible to use throttling to reduce the maximum dynamic pressure and also the maximum longitudinal acceleration. These requirement may be driven by the necessity to reduce the drag force and the mechanical stresses to the payload. Because the thrust can be modulated it is possible to perform a different trajectory with respect to the one that would be achieved for a fixed thrust system. This way it is possible also to reduce the drag forces hence reducing the ascending required Δv.

PECULIAR MISSION PROFILES Thanks to throttling it is possible to perform some very peculiar mission profiles. The first striking example is the Lunar Module soft landing. Then also an ascending and descending vehicle would require such capability. A flying test beds such as Mighty Eagle and Project Morpheus use throttling in order to test some experiment and innovative navigation systems. Another relevant example of throttling is the recent reusable launching strategy used by SpaceX.

It would not be possible to vertical land a launcher without on-demand thrust modulation. Implementing throttleability can increase consistently the range of applications for hybrid propulsive technology.

Unfortunately, because of hybrids peculiar diffusive flame mechanism, the throttleability dose not come without disadvantages:

o/f SHIFT Because the fuel mass flow in the combustion chamber is correlated with the oxidizer mass flow to it, the system is harder to control. In conventional hybrid rocket motors the o/f is affected by a change of the oxidizer mass flow, the oxidizer to fuel ratio shifts. This shift brings some loss of performances. This aspect will be discussed in detail in the next chapter.

INCREASE IN SYSTEM COMPLEXITY Hybrid rocket motors are simple and as long as they are kept simple it is possible to maintain their characteristics of reliability, safety and low cost, which are much appreciated by many people. By adding the flow control valve required to perform throttling, the system increases in complexity. It is a possible part of the motor that can fail. This is not seen with good eyes from some hybrid rocket motor designers according to whom the hybrid rocket design must be kept as simple as possible, without intricacies.

Beside the advantages and disadvantages related to the implementation of throttling, some considerations related to the possible applications of hybrid technology must be taken into account. The argued applications of hybrids are many: launchers, apogee kick motor, sounding rockets, VTVL[24] ADV[25], flying test beds and many others. But at today the real "flight" application of the hybrid rocket technology are very limited. Figure 1.7 shows some of the actual applications of HRM, among them there are: ONERA's LEX hybrid sounding rocket (Figure 1.7(a)), Virgin Galactic's Space Ship One (Figure 1.7(b)), Bloodhound SSC (Figure 1.7(c)) and Thales Alenia Space's SPARTAN Project (Figure 1.7(d)). These are peculiar applications: space tourism launchers, flying test beds and, unexpectedly, world record speed cars. Some of these applications require throttling. As already mentioned sounding rockets often used throttling to increase the trajectory efficiency, for ascending and descending vehicles throttling is a must. The only application of the four exposed that do not use throttling is Space Ship One, but it is not such a remote hypothesis that future versions of tourism space ships could be implement with throttling feature. Among the other potential space applications, launchers and in orbit transfer engine throttling could be a required feature as well, but because of the c^* penalties involved there must be a case to case analysis for this implementation. Bellomo discussed the importance of throttleability and the application

---

24 Vertical take-off vertical landing
25 Ascending and descending vehicle

of hybrid technology for formation flight in his PhD thesis [52]. Schmierer studied a hybrid rocket motor demonstrator concept for moon sample return mission requiring throttling for soft landing purposes[35].

As it should be clear from this short HRM applications overview, throttleability is an important and required feature for current and future hybrid rocket engine applications. A consistent part of the work we carry out at the University of Padova Hybrid Propulsion Group is end-of-application research and because throttling is quite a requested feature our group must increase his knowledge and capability in designing and testing throttleable hybrid systems.

Up to now our group was able to test hybrid rocket motors with parallel feeding lines finalized in achieving a boost-sustain like thrust profile, in a fashion similar to the first hybrid sounding rockets. The group also participated actively to the SPARTAN project in the testing phase of the throttleable motor, but previously to this PhD research project it was not possible to independently test a HRM with a continuous and not discrete thrust profile.

1.2 PROJECT OBJECTIVES AND THESIS OUTLINE

The current research project is focused on the investigation of throttleability on hybrid rocket motors. The hybrid rocket motor configuration was not determined at the beginning of the project, two options were possible:

- axial gaseous oxidizer injection, paraffin fuel grain and a mixer in the post combustion chamber.

- gaseous swirled injection, HDPE[26] fuel grain, conventional post combustion chamber design.

These two configuration were proved to be high performance and high regression rate within the research group at a oxidizer thrust class of 300 and 7 kN. The test motor will have the following characteristics:

- 1 kN maximum thrust (vacuum equivalent thrust);

- HTP as an oxidizer which is injected in the combustion chamber in the decomposed gaseous form;

- a catalyst pack will be used to decompose the HTP flow;

- the engine will be self ignited by means of the decomposed hot gasses from the catalyst pack;

---

26 High density polyethylene

- continuous throttling capability with a throttling ratio of 10:1;

- pressure fed system.

The throttleability will be implemented by means of a flow control valve. The FCV will be developed in house and will have the following characteristics:

- it will be safe to operate in an experimental environment;

- its design will be solid and robust, i.e. not flight-weight;

- the rise and fall time over the range of throttleability will be 1.2 seconds.

The developed flow control valve will be statically and dynamically characterized and its suitability for throttling purposes will be investigated. This characterization will be aimed to:

- determine the valve characteristic curve;

- determine the valve dynamic behaviour;

- determine the valve application limits;

- evaluate possible valve insertion effects on the combustion chamber.

The investigation methods used during this research are mainly experimental although the experimental results are compared with the ones coming from simplified analytical models.

The experimental test setup used to evaluate the motor performances, throttling capabilities and characterize the flow control valve will have to:

- be safe to operate;

- provide accurate measurements of the appropriate physical quantities;

- allow to perform several tests per day;

The work performed during the last three years is reported in this thesis which follows this outline:

- Chapter 2 describes a simplified combustion model that is used intensively to interpolate experimental data and evaluate the penalties due to throttleability. A thorough description of the c^* related penalties is made, and the possible alternative are taken into account.

- Chapter 3 describes the flow control valve design and characterization phase. Both valve body and actuation are described. The valve is is based on the variable area cavitating venturi principle the control loop is open on the thrust but closed on the pintle position.

- Chapter 4 describes the test motor, experimental setup and the performed fire test campaigns. Two preliminary fire test campaign with two different motor configurations are described, only one is used to perform the presented dynamic throttling fire tests. The obtained results are compared with the command reference and the expected from a theoretical model.

THROTTLING OF HRMS

In this chapter the implications of hybrid rocket throttleability are discussed. An analytical model that describes the hybrid combustion is presented in order to draw some conclusions about the penalties that are due to throttling. These penalties are mainly due to a combustion chamber characteristic velocity reduction caused by an oxidizer to fuel ratio shifting that in turn is generated by the diffusive flame mechanism.

2.1 HYBRID ROCKET STEADY STATE COMBUSTION

In order to understand the implications of hybrid rocket throttleability it is necessary to introduce the physics of steady hybrid combustion. The fundamental theory of hybrid combustion and fuel regression has been proposed by Marxman and co-workers; it will be described briefly in this section. In a typical hybrid rocket the oxidizer enters the combustion chamber from the fore end and flows over the solid surface of the fuel grain. After motor ignition a macroscopic diffusion flame develops above the grain. This same heats up the grain surface until the solid fuel decomposes. The vaporized fuel mixes with the incoming oxidizer sustaining the combustion.
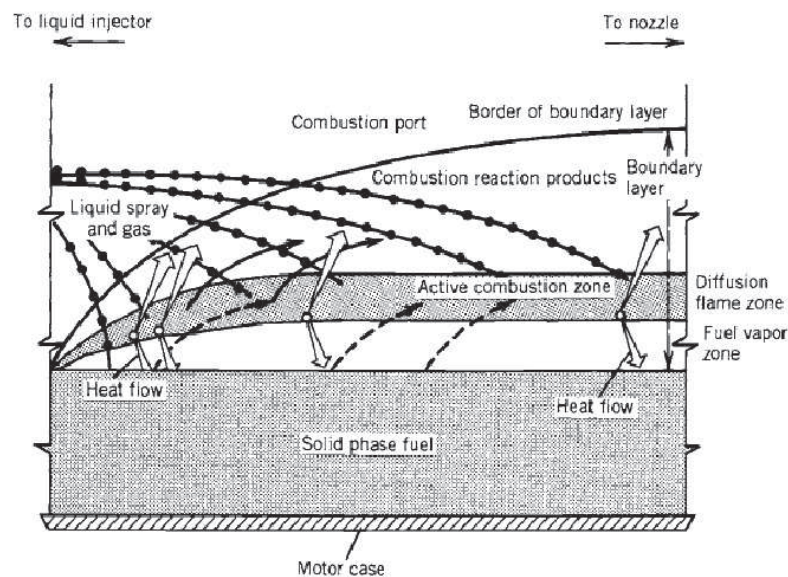

Figure 2.1: Diffusion limited flame mechanism

These phenomena take place inside the boundary layer. The boundary layer is the region that is affected by the presence of the wall. It is possible to define multiple boundary layers, each one related to a specific variable. The thermal boundary layer

is defined as the zone where the temperature changes from the value of the incoming flow to the wall temperature. The species boundary layer is the zone where the chemical concentration changes from the value of the incoming flow to the value at the wall. The momentum boundary layer is defined as the region where the velocity is affected by friction and the fluid has to slow down in order to meet the no slip boundary condition at the wall. In the boundary layer large gradients of the fluid variables occur. Let's consider the general conservation equation for a fluid quantity in the Eulerian form (with respect to a fixed reference frame):

$$\frac{\delta \Phi}{\delta t} + \vec{v} \cdot \nabla \Phi = D_\Phi \, \nabla^2 \Phi + S_\Phi \tag{2.1}$$

The first term on the left hand size is the time variation of the generic property Φ the second one is the convective transport of Φ. On the right hand side we have the diffusion of Φ (D_Φ is the diffusion coefficient) and the source or sink term for Φ. Outside the boundary layer the fluid flow can be assumed as inviscid. Temperature, momentum and chemical concentration follow equation 2.1 suggesting a similar behaviour. This is the basis for the Reynolds analogy. The Reynolds analogy states that under specific conditions the solutions of equations 2.1 should be similar, hence the different properties Φ follow the same profile. These profiles can be related each other by adimensional parameters defined as the ratio between the diffusive transport of Φ_1 and the diffusive transport of Φ_2. Some parameters of interest for next discussions are the following:

$$\text{Prandtl number} \quad Pr = \frac{v}{k} = \frac{\mu \, c_p}{\lambda} \tag{2.2}$$

$$\text{Lewis number} \quad Le = \frac{k}{D} = \frac{\lambda}{\rho \, c_p \, D} \tag{2.3}$$

$$\text{Schmidt number} \quad Sc = \frac{v}{D} = \frac{\mu}{\rho \, D} = Le \cdot Pr \tag{2.4}$$

In the Reynolds analogy these numbers represent the ratio between the thickness of several boundary layers. The most important consequence of Reynolds analogy is that only one profile need to be known, the others can be scaled from the latter by knowing the relative adimensional number. Similar profiles imply similar derivatives of those profiles. This similitude is particular relevant, the convective heat flux proportional to the temperature gradient and is equal to $\dot{q} = -\lambda \frac{\delta T}{\delta y}$. This heat can be determined from the shear stress that is proportional to the velocity gradient and equal to $\tau = \mu \frac{\delta v}{\delta y}$. This analogy is widely used to solve heat transfer problems by knowing the solution of the momentum equation. Marxman used this analogy to determine a regression rate correlation in hybrid rocket motors.

Inside the boundary layer the oxidizer diffuses from the external flow toward the solid surface, while the fuel diffuses from the fuel grain surface outward. Oxidizer and fuel mix to generate the flame region. The concentration profile that forms is the result

of the balance between diffusion and convection. The flame is established inside the boundary layer at a position where the concentration between the reactants is favourable. On normal hybrid the rate at which the flame reaction occurs is much higher than the rate at which the reactants reach the flame region. The Damkohler number (Da) is defined as the ratio between the fluid dynamic time scale and the chemical reaction time scale. For conventional hybrid combustion $Da >> 1$, the combustion is then defined diffusion controlled or diffusion limited. Under these circumstances it is possible to neglect the combustion rate. It is possible to divide the boundary layer in two regions separated by the flame. In the upper part the oxidizer diffuses through the combustion products that generates in the flame toward the flame position. The remaining part which ranges from the flame to the fuel surface is composed by decomposed fuel vapours that migrate from the surface to the flame. Marxman considered the steady state heat balance at the wall: the heat at the wall is the one required to vaporize the fuel plus the heat conducted inside the fuel grain:

$$\dot{q}_{wall} = \dot{r}\,\rho_{fuel}\,L_v + \dot{q}_{cond} \tag{2.5}$$

It can be easily demonstrated that for a quasi steady state regression rate of the fuel surface, in which there are no in depth heat absorbing mechanism, the heat loss for conduction is equal to the heat required to warm up the eroded amount of base material from the initial temperature to the wall temperature. The surface heat balance becomes then:

$$\dot{q}_{wall} = \dot{r}\,\rho_{fuel}\,L_v + \dot{r}\,\rho_{fuel}\,c\left(T_{wall} - T_{in}\right) \tag{2.6}$$

$$= \dot{r}\,\rho_{fuel}\left(L_v + c\left(T_{wall} - T_{in}\right)\right) = \dot{r}\,\rho_{fuel}\,h_v. \tag{2.7}$$

The wall heat flux q_w is composed by two terms: convective and radiative heat flux. The radiative heat is not taken into account in the classic hybrid theory also if a correction was subsequently introduced. The reason for this is that in normal operative regimes the convective heat flux is several times greater than the radiative one. The key element in Marxman theory is the correlation of the convective wall heat flux with wall shear stress. The first assumption is to consider the Prandtl and Lewis numbers equal to one. This is a frequently made hypothesis for a turbulent boundary layer of a gaseous mixture, the implication for this is that all the boundary layers have the same height. Another hypothesis made by Marxman is that the fluid is incompressible. This is an incorrect hypothesis that is necessary in order to come to understand hybrid combustion behaviour.

$$\dot{q}_{wall} = -\frac{\lambda}{c_p}\frac{\delta h}{\delta y} \overset{Pr \approx 1}{=} -\mu\frac{\delta h}{\delta y} \tag{2.8}$$

By applying the Reynolds analogy between the fuel surface and the flame it is possible to linearly correlate the enthalpy gradient to the velocity gradient:

$$\frac{\dot{q}_{wall}}{h_{flame} - h_{wall}} = \frac{\tau_{wall}}{v_{flame} - v_{wall}} \tag{2.9}$$

because the speed at the wall is zero ($v_{wall} = 0$) the wall flux is equal to:

$$\dot{q}_{wall} = \tau_{wall} \frac{h_{flame} - h_{wall}}{v_{flame}} \tag{2.10}$$

In this equation the wall friction can be determined using the friction coefficient definition $\tau_{wall} = \frac{1}{2}\rho_e\, v_e^2 C_f$:

$$\dot{q}_{wall} = \frac{1}{2}\rho_e\, v_e C_f \frac{v_e}{v_{flame}} \left(h_{flame} - h_{wall} \right) \tag{2.11}$$

By using equation 2.7 we have:

$$\dot{r}\, \rho_{fuel}\, h_v = \frac{1}{2}\rho_e\, v_e C_f \frac{v_e}{v_{flame}} \left(h_{flame} - h_{wall} \right) \tag{2.12}$$

In this equation the unknown variables are the friction coefficient (C_f) and the ratio between the speed at the edge of the boundary layer and the speed at the flame (v_e/v_{flame}). It must be noted now that there is a presence of blowing due to fuel gaseous decomposition and reaction. The blowing is that phenomena in which the boundary layer is inflated by the presence of a vertical speed component at the wall. This inflation of the boundary layer reduces the wall gradients reducing in turn the shear stress and heat flux. The blowing parameter describes the flow over a blowing surface and is defined as:

$$B = \frac{\dot{m}_{fuel}}{\frac{1}{2}\rho_e\, v_e\, C_f} \tag{2.13}$$

This parameter represents the adimensional form of the vertical mass flow. In an hybrid motor the vertical mass flow is determined by the amount of decomposed fuel that enters the boundary layer. In hybrid physics B it is not a free parameter. Using the definition of blowing parameter in equation 2.12 we have:

$$B = \frac{v_e}{v_{flame}} \frac{h_{flame} - h_{wall}}{h_v} \tag{2.14}$$

Hence substituting the latter equation in equation 2.12 we have:

$$\dot{r}\, \rho_{fuel} = \frac{1}{2}\rho_e\, v_e\, C_f\, B \tag{2.15}$$

Marxman was also able to determine the ratio between flame and boundary layer edge velocities based on the position of the flame:

$$\frac{v_{flame}}{v_e} = \frac{O/F_{flame} \frac{h_{flame} - h_{wall}}{h_v}}{K_{oxe} + (O/F + K_{oxe}) \frac{h_{flame} - h_{wall}}{h_v}} \tag{2.16}$$

The velocity ratio v_{flame}/v_e is dependent only on the enthalpy ratio $(h_{flame} - h_{wall})/h_v$ and the oxidizer to fuel ratio O/F at the location of the flame. Now that the blowing parameter B, and the ratio v_e/v_{flame} have been determined the only quantity left to determine of equation 2.12 is the friction coefficient C_f. The value friction coefficient under blowing conditions (C_f) is not the same one for the friction coefficient in absence of blowing (C_{f0}), but the two can be related:

$$\frac{C_f}{C_{f0}} = \left[\frac{ln\,(1+B)}{B}\right]^{0.8} \left[\frac{1 + 13\,B/10 + 4\,B^2/11}{(1+B)\,(1+B/2)}\right]^{0.2} \tag{2.17}$$

Note that this equation meet the following conditions: $C_f/C_{f0} = 1$ for $B = 0$ and $C_f/C_{f0} \rightarrow 0$ for $B \rightarrow$ inf. A good interpolation for equation 2.17 for a wide range of blowing parameters is the following:

$$C_f/C_{f0} = 1.2\,B^{-0.77} \quad \text{for}\,(5 \leq B \leq 100) \tag{2.18}$$

Later Altman in [14] proposed a new interpolation model that is more accurate in the typical hybrid rocket motor range:

$$C_f/C_{f0} = B^{-0.68} \quad \text{for}\,(5 \leq B \leq 20) \tag{2.19}$$

It must be kept well in mind that the later equations are interpolation fit and hence their application is limited to their range.

In the classic hybrid combustion theory the friction coefficient in absence of blowing is determined from the one of the flat plate:

$$\frac{C_{f0}}{2} = 0.03\,Re_x^{-0.2} \tag{2.20}$$

Where Re_x is equal to:

$$Re_x = \frac{\rho_e\,v_e\,x}{\mu_e} \tag{2.21}$$

The use of the flat plate theory is, of course, a simplification and a strong hypothesis in the classic theory, however this equation leads to draw some important conclusions on hybrid rocket steady state combustion. Substituting equations 2.19, 2.20 in equation 4.1 we get:

$$\dot{r}\,\rho_{fuel} = 0.03\,\left(\frac{\mu_e}{x}\right)^{0.2} (\rho_e\,v_e)^{0.8}\,B^{0.32} \tag{2.22}$$

The product between density and velocity at the edge of the boundary layer $(\rho_e\,v_e)$ is approximated to the local mass flux (G).

$$\dot{r}\,\rho_{fuel} = 0.03\,\left(\frac{\mu_e}{x}\right)^{0.2} G^{0.8} B^{0.32} \tag{2.23}$$

Rearranging the latter and combining the nearly constant terms we get:

$$\dot{r} = a^I\,G^{0.8} x^{-0.2} \tag{2.24}$$

This is the important result of Marxman theory, an analytical equations that correlates the fuel grain regression rate with the local mass flux. It must be noted that even if this equation was derived by imposing some strong hypothesis (incompressible flow, flat plate friction, flux approximation, etcetera...) it is a good mean to understand which are the parameters involved. Some alternate forms of equation 2.24 are used to fit experimental data. Normally the experimental results are spatially and temporally averaged. Following the procedure in [30] it is possible to obtain the following averaged forms of equation 2.24:

$$\dot{r} = a^{II} \left(O/F\right) G_{tot}^{0.8} L^{-0.2} \quad \text{or} \quad \dot{r} = a^{III} \left(O/F\right) G_{ox}^{0.8} L^{-0.2} \tag{2.25}$$

The second one leads the famous general expression that is used to interpolate experimental results:

$$\dot{r} = a^{IV} \left(O/F\right) G_{ox}^{n} L^{m} \tag{2.26}$$

Normally the values for a, n and m obtained from experimental tests are different from the ones predicted by Marxman theory. This is expected given the amount of approximations and hypothesis done during the Marxman theory demonstration. Many times from an experimental point of view, the effect of the fuel grain length (L^m) is included in the a coefficient and also the dependence of a from the o/f is forgotten, leading to the following expression:

$$\dot{r} = a \, G_{ox}^{n} \tag{2.27}$$

Since the contribution to the regression rate of L is included in a the reported Marxman law coefficients are dependent on the fuel grain length. In order to have a complete understanding of the involved phenomena the length of the fuel grain should be declared. However the scale of the motors used in hybrid propellant characterization are similar (even from different research groups) leading to comparable results. The term L^m represents the scale effect, for an increase of the fuel grain length, if m is negative, the regression rate is reduced. Normally the length averaged form of the regression rate equation is more accurate than the punctual one. In fact the regression rate law along the fuel grain does not follow the power law in equation 2.24 for the initial values because the regression rate in the fore-end of the grain depends on the type of injection, the pre combustion chamber design and the flame holding mechanism [38],[11],[12]. This effects are particularly relevant for low aspect ratio fuel grains.

Marxman power laws are valid only for a determinate range of oxidizer fluxes G_{ox}. For low fluxes the radiative heat flux overcomes the convective one, hence it is no more negligible. Marxman introduced a radiative heat correction to his theory that is not here reported. The factors that influence the effect of radiation are: flame emission coefficient (metal particles[1]) and fuel grain absorption (fuel grain soot and dye). For high oxidizer

---

1 Metallized fuel grains and flames highly increase the emissivity ϵ
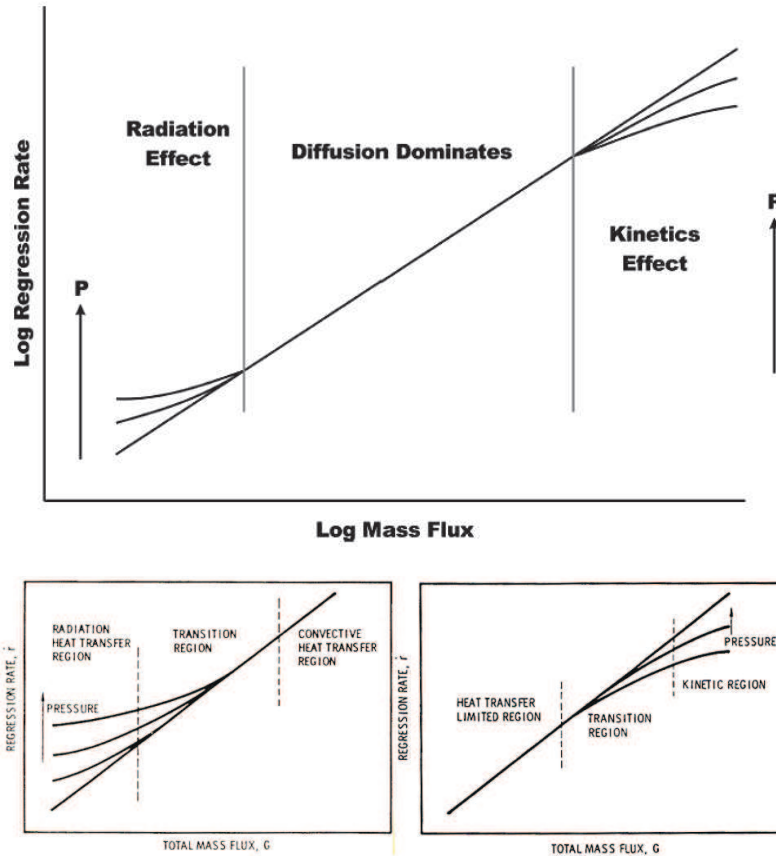
Figure 2.2: Example of a logarithmic trend of the fuel regression rate with the mass flux and effects for very high and low fluxes.

fluxes, the Marxman power law is not valid for a different reason: the reactants residence time through the boundary layer and flame is so small that $Da >> 1$ hypothesis fades. The chemical kinetic effect can not be neglected, and it will play an important part in limiting the reaction. Analogously to what happens in solid rocket motors, the regression rate is dependent on the local pressure, this is because pressure plays an important part on chemical kinetic. Figure 2.2 summarizes the last considerations about hybrid combustion regression rate on a logarithmic plot of the regression rate $\dot{r}$ versus the mass flux G. In a logarithmic plot the Marxman power law appears as a straight line with a slope equal to the power law exponent n. For high mass fluxes the slope decreases because of the chemical kinetic limitation. On the other end, for low fluxes the slope decreases as well because of the increasing effects of the radiative heat. Moreover, outside of the diffusion dominated "linear" region a family of curves appears on both ends, these represents the effect of pressure on the regression rate outside the diffusion dominated region. For conventional fuels like paraffin, HDPE, HTPB the diffusion limited region is quite wide. This region tends to shrink, on the left hand size when temperature enhancing metal particles are added to the propellant formulation or the fuel grain is dyed. The reduction of the diffusion dominated region is reduced on the right hand side as well when a low combustion chamber pressure is employed. It is evident that the complex

correlation between fuel regression rate and fluxes becomes even more complicated when operating outside the diffusion controlled region. Normally, for sake of simplicity and control, a hybrid rocket motor operates within a predetermined oxidizer mass flux range.

The theory presented until now describes only the steady state combustion modeling for a hybrid rocket motor. The motor respond differently in a dynamic situation. Stanford University[6][31], Arif Karabeyoglu[46] and Francesco Barato[25] studied in detail the dynamic behavior of an hybrid rocket motor. The combustion chamber is characterized by a characteristic filling and emptying time τ_{fill} which is dependent on the combustion chamber volume, throat area and chemical composition of the gas. In a simplified 0-D model, this characteristic time governs how the combustion chamber pressure respond with a variation of the incoming propellant flux. The fuel production depends on the thermal lag in the solid fuel grain and the relation between incoming heat flux and oxidizer mass flow[46][24]. Because of thermal lag there can be also an overshoot on the fuel production. The oxidizer flow to the combustion chamber depends on the feeding line and flow control mechanism. In many instances the transient period of the feeding system is higher than the fuel grain one. In this work only the macroscopic effects that throttling have on the combustion are considered.

2.2   HRMS THROTTLING BEHAVIOUR AND c^* PENALTIES

The experimental results reported in this work are often compared with the form of Marxman power law in equation 2.27, the same law is used as a regression rate model. The implications of the dependency between fuel regression rate and oxidizer mass flux have already been qualitatively discussed in the introduction; these being a major disadvantage of the hybrid propulsive technology. Because of the potential implication that throttling can have on the motor performances, in this section the impact of throttling is quantitatively presented with a simplified model.

2.2.1   o/f shift

If we consider a single circular port fuel grain, with a port diameter D_p and a port length L_p, in which only the fuel in the port take part to the combustion, i.e. the only regressing surface of the fuel grain is the port (no face effect), we have that the fuel mass flow coming from the fuel grain is equal to:

$$\dot{m}_f = \dot{r} \, A_{fuel} = \dot{r} \, \pi \, D_p \, L_p \tag{2.28}$$

Now let's suppose that the fuel in the port burns following the Marxman power law:

$$\dot{m}_f = a\ G_{ox}^n\ L_p^m\ \pi\ D_p\ L_p = a\ G_{ox}^n\ \pi\ D_p\ L_p^{1+m} \tag{2.29}$$

$$= a\ \left(\frac{\dot{m}_{ox}}{\pi\ D_p^2/4}\right)^n\ \pi\ D_p\ L_p^{1+m} \tag{2.30}$$

The instantaneous oxidizer to fuel ratio is defined as the ratio between injected oxidizer and injected fuel. It follows that the oxidizer to fuel ratio is:

$$o/f = \frac{\dot{m}_{ox}}{\dot{m}_f} = \frac{\dot{m}_{ox}}{a\ \left(\frac{\dot{m}_{ox}}{\pi\ D_p^2/4}\right)^n\ \pi\ D_p\ L_p^{1+m}} = \frac{\dot{m}_{ox}^{1-n}\ D_p^{2n-1}}{a\ \pi^{1-n}\ 4^n\ \rho_f\ L_p^{1+m}} \tag{2.31}$$

We must remember that the latter equation has been determined introducing the following hypothesis:

- circular port fuel grain

- no fuel grain faces contribute to the combustion (only the fuel grain port burns)

- the fuel port burns uniformly following the length averaged Marxman power law $\dot{r} = a\ G_{ox}^n\ L_p^m$

Nevertheless, from equation 2.31 it is possible to draw some important conclusions about the parameters that influence the o/f and lead to the o/f shift. Three are the variables involved in the combustion that influence the oxidizer to fuel ratio: port diameter D_p, oxidizer mass flow $\dot{m}_{ox}$ and fuel port length L_p. The latter doesn't varies much in normal hybrid rocket motor conditions, and its effect could be however negligible because of HRMs high aspect ratio. Therefore the two major players in o/f shifting are oxidizer mass flow and port diameter. It is possible to note from equation 2.31 that the Marxman power law exponent n plays a important part on the effect of the above mentioned variables. The effects of the port diameter is null for an exponent n equal to 0.5. This is a condition that is very looked after in conventional hybrid rocket designs. Because some applications of hybrid rocket motors require a constant thrust and hence constant oxidizer mass flow, there would be no o/f shift if a particular propellant formulation with n as close as possible to 0.5 could be employed. Such power law exponents were reported for paraffin based fuels and N_2O or HTP. Another example of near 0.5 power law exponent, but for low regression rates, is the recent use at the JPL[2] of SP-7/MON[3]. They look to use this performing propellant formulation in their Mars ascending vehicle project [37],[8]. With respect to equation 2.31, the oxidizer mass flow effect is null if the power law exponent is equal to 1. Unfortunately Marxman theory does not take into account for such high exponents, and among all the experimental results available in literature there are hardly

---

2 Jet Propulsion Laboratory
3 Mixed oxides of nitrogen

values higher than 0.85 reported. It is not possible to void the effects of both port diameter and oxidizer mass flow at the same time. For a throttleable hybrid rocket, which requires oxidizer flow control in order to modulate the thrust, it is not possible to avoid o/f shift. Figure 2.3(a) shows the effects of a variation of the port diameter adimensionalized with
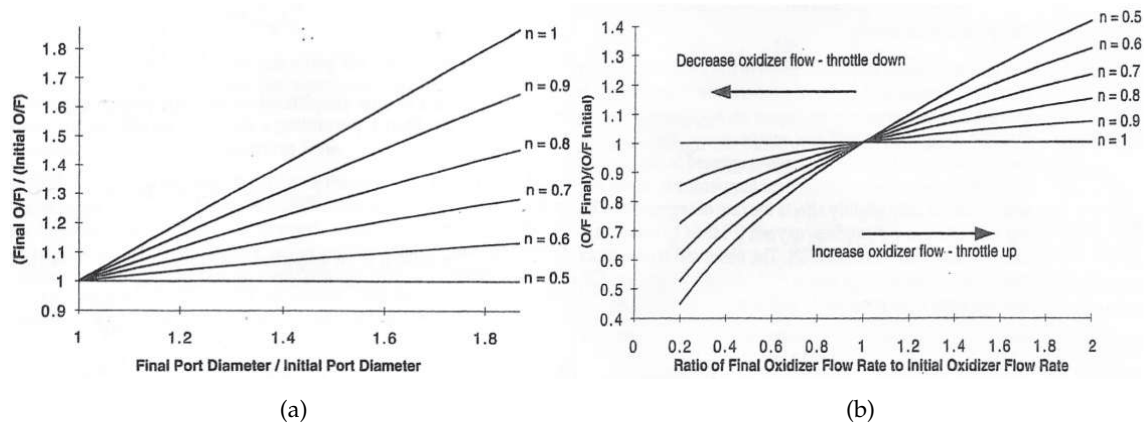

Figure 2.3: Examples of adimensional o/f shif for hybrid rocket motors. On the left the effect of port diameter. On the right the effet of a variation of oxidizer mass flow.

the initial one on the oxidizer to fuel ratio, for various power low exponents. Figure 2.3(b) shows the effect of a variation of the oxidizer mass flow with respect to the nominal one. Selecting the most suitable power law exponent for a throttleable hybrid rocket motor is a case dependant choice. It must be weighted over the different conditions. For example given a final to initial port diameter and a required throttling ratio a suitable n value could be the one which gives an evenly distributed o/f shift over the two effects. Another aspect that can be kept into account is the expected thrust profile. If most part of the time is spent at a fixed thrust and the throttling capability is exploited only occasionally, the weight of the throttling losses could be negligible with respect to the losses induced with the variation of the port diameter. Another thing to take into account about near 0.5 power law exponents (and direct consequence of o/f shift absence with the port diameter) is this: after a temporary variation of the oxidizer mass flow the return to the previous combustion chamber pressure and thrust is granted. Because the performances are not affected by a variation of the port diameter. For sake of clarity let's consider the following example:

Figure 2.4 shows the results of a simplified quasi-stationary numerical simulation using a lumped parameter zero-order model. In figure 2.4a the three different normalized oxidizer mass flow profiles are presented, these curves are input for the simulations. The results reported in figure 2.4b and figure 2.4c show the difference in the output normalized pressure profiles. In particular after a variation from the nominal oxidizer mass flow and the consequent restore of the nominal conditions there is a difference in the restored pressure, which is also dependent on duration and intensity of the throttle

(a)

(b)   (c)
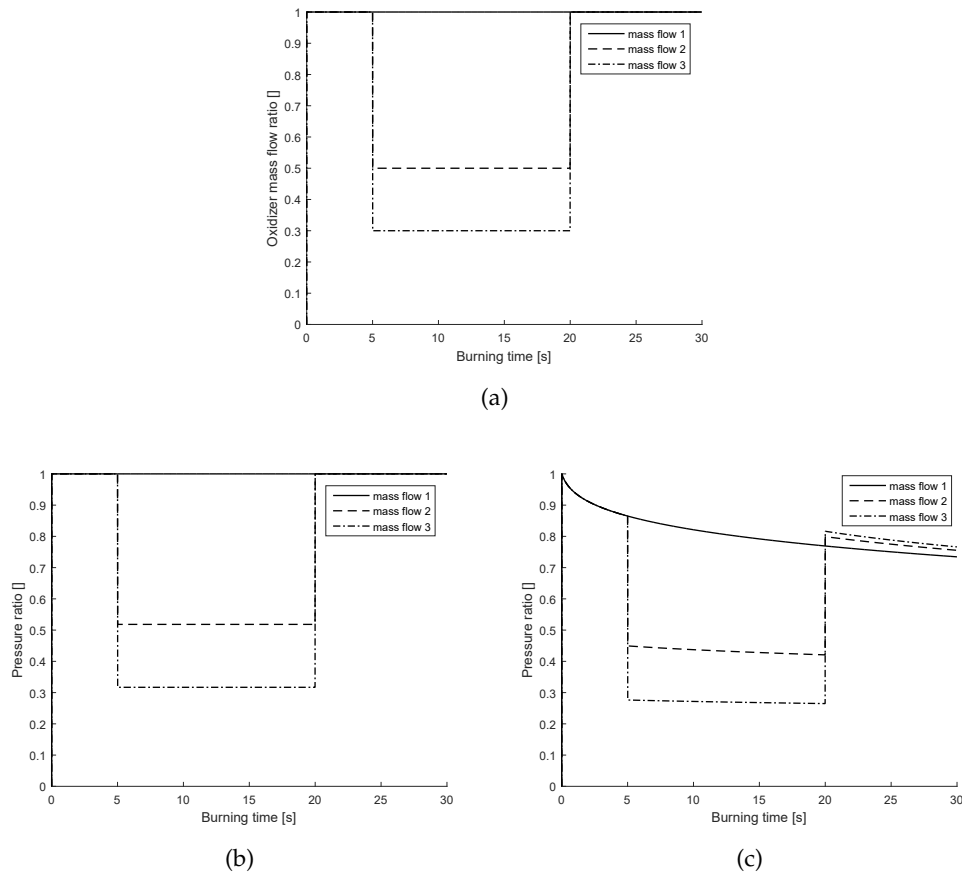
Figure 2.4: Difference between pressure profiles after an arbitrary variation of the oxidizer mass flow for $n = 0.5$ and $n = 0.8$

down. Figure 2.4b shows how this is not the case with an n exponent equal to 0.5. Of course this simplifies a lot the thrust control, because it guarantees a one-to-one relation between oxidizer mass flow and pressure. Therefore the 0.5 exponent provides the best accuracy for a throttleable hybrid in open loop, accepting, anyway, a slightly higher c^* penalty compared to a higher n. If the propellant formulation and motor design power law exponent differs significantly from 0.5 the thrust control algorithm must take into account for the port diameter variation in order to precisely know the performed thrust.

2.2.2 c^* penalties

Until now we discussed the effects of throttling and port diameter variation on the o/f. These are worth of note for mainly one reason: the motor performances are dependent on the oxidizer to fuel ratio. The combustion chamber characteristic velocity strongly depends on the oxidizer to fuel ratio. The optimal c^* can be achieved only for a limited o/f range span. There are two important thing to during c^* penalties evaluation: the first is how a variation of oxidizer mass flow affects the o/f the other is how the characteristic velocity is affected by a o/f variation. Figure 2.5 shows three trends of the characteristic

Figure 2.5: Characteristic velocity trends with the oxidizer to fuel ratio for paraffin and LOX, nitrous oxide and 90% high test peroxide.

velocity with the oxidizer mass flow for three different propellant formulations, paraffin as a fuel and various oxidizers: LOX, N_2O and 90% HTP. This trends were 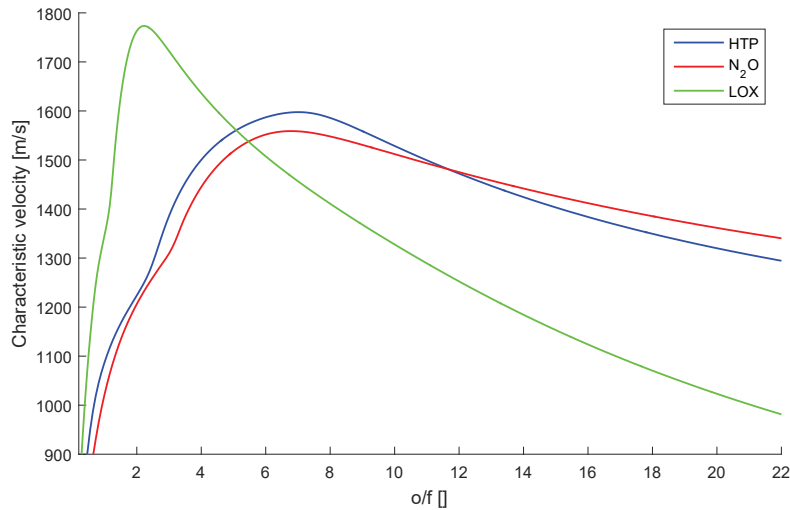obtained using NASA's CEA[4] computer program[26]. It is possible to note that the c^* peak for N_2O and HTP is quite flatter than the one for LOX. Also the characteristic velocity for N_2O and HTP on the oxidizer rich side (high o/f) tends to an asymptotic value, this is because hydrogen peroxide and nitrous oxide are both oxidizers and monopropellants, they exothermically decompose into a stable gas mixture. These aspects must be taken into account when evaluating throttling performances. Once again the expected thrust profile plays an important role, this time in the choice of which part of the presented diagram use to operate the engine. If the thrust profile is not known and there is equal probability to perform the maximum and minimum thrust, then the the operative region should be the one that allow equal characteristic velocity losses for both thrusts, i.e. a balanced region around the maximum c^*. But if we consider a thrust profile coherent with the one that was predicted for the LMDE, visible in figure 2.6, it is evident that the average thrust is shifted toward the higher values. In this case it is convenient for the motor to operate in a fuel rich region in order to have the average thrust o/f close to the optimal one.

Table 2.1 reports the maximum values of c^* and c^* sensitivity [5] as well as two information about the c^* penalty which incur with a throttling ratio of 5 and 10. In the first case (balanced), the throttling takes place around the o/f at which the maximum c^* is achieved and ranges in both the oxidizer rich and fuel rich regions. In the second case the motor operates only in the fuel rich region, starting from the optimal mixture ratio.

---

4 Chemical Equilibrium and Applications

5 Where c^* sensitivity means the second derivative of the trends in figure 2.5 around the c^* maximum point.
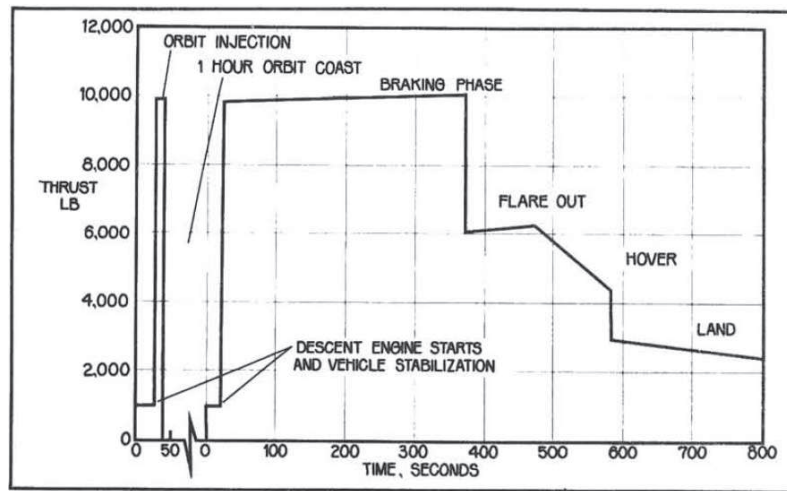
Figure 2.6: The thrust profile that was expected for the lunar module descent engine during the design phase.

There are two main reasons why the second c^* penalty is reported, first the quantity of total impulse associated with the low thrust could be smaller if compared with the high thrust, and considering LMDE duty cycle (applicable for a soft landing ADV in general) the motor spend less time at the lower thrust. Secondly, in the fuel rich region the drop in c^* is partially compensated by the relative increase of consumed fuel mass and so the motor behaviour results more linear than the one achieved in the oxidizer rich region. A linear motor behaviour would facilitate the throttling control loop, especially if open.

	HTP	N_2O	LOX
Maximum c^* [m/s]	1598	1559	1773
c^* Sensitivity [m/s]	−22.4	−16.3	−369.9
c^* Penalty TR=5 (balanced)	95.3%	95.9%	96.2%
c^* Penalty TR=5 (fuel rich)	88.0%	84.5%	82.7%
c^* Penalty TR=10 (balanced)	91.6%	92.8%	93.2%
c^* Penalty TR=10 (fuel rich)	78.3%	78.5%	75.4%

Table 2.1: Characteristic velocity maximum, sensitivity and losses

The $c^\star$ sensitivity has been computed as a discrete numerical second derivative using three equally spaced o/f points. The mid point is the point of maximum characteristic velocity. The interval that defined the second derivative varied with the propellant formulation, it was set to 0.2 for HTP, and it was reduced for N_2O and LOX taking into account that the point of maximum characteristic velocity is actually at a lower oxidizer to fuel ratio. The thermochemical data used for these considerations were obtained using CEA computer program. For the balanced case the reported penalties were computed

using an iterative procedure in which at the beginning a throttling ratio is set, from this an initial ratio between maximum and minimum oxidizer mass flow is determined. With a variation of the oxidizer mass flow comes and alteration of the oxidizer to fuel ratio as expected by equation 2.31. With this data an initial characteristic velocity penalty is computed using the $c^\star (o/f)$ function from CEA. But since the thermochemical properties affects the value of the force coefficient, another couple of value for the minimum and maximum oxidizer mass flow are determined, and hence the iterative procedure is repeated until convergence of the obtained $c^\star$ penalties. The procedure for the balanced case penalties is very similar, with the difference that the operative o/f for the maximum thrust is known. The power law exponents n used to obtain the data presented in table 2.1 are 0.5, 0.5 and 0.65 for HTP, N_2O and LOX respectively. As we can see the advantage of having an higher exponent for the *paraffin-LOX* formulation and hence a lower o/f shift associated with throttling is compensated by the high sensitivity of the propellant, for the maximum achievable characteristic velocity efficiency is comparable with the one for HTP and N_2O.

It is important to remember that all this considerations were made under the assumption of cylindrical fuel grain which is consumed exclusively in the port following the simplified Marxman power law. This model does not take into account for the face consumption and the contribution of thermal protection which could also represent an effective manner to reduce or mitigate the negative effects of throttling on the characteristic velocity.

3

FLOW CONTROL VALVE DESIGN

The flow control valve development process started during the first Ph.D. year and ended at the beginning of the third year. The aim was to design, develop and realize an prototype flow control valve to be used on the hybrid rocket motors under development at the hybrid propulsion group. The design procedure for the development of the FCV was subject to changes during these three years to what was expected at the beginning of the first year.

A flow control valve is a device that is used to control the oxidizer mass flow to the hybrid combustion chamber, in order to achieve a variable rocket thrust. A flow control valve is not the only way to throttle a motor but we find it a suitable solution for our particular motor configuration.

3.1 THROTTLING METHODS

There are many methods to achieve throttling. Casiano, Hulka and Yang presented a comprehensive review on LRM throttling[54]. Because of the peculiar nature of liquid rockets many of the throttling methods presented are coupled with injector design. Figure 3.1 represents a chart of the possible throttling methods for a LRM investigated by NASA during project MX-794.

The final throttling method used in this PhD work differs from the ones exposed in this chart. However a general introduction of the most used throttling method is here presented:

- The first method consist in using a flow control valve, but because of injection atomization requirements the pressure drop in the injection plate can be excessive for high mass flows limiting the effective throttling ratio.

- The second method uses a variation of the injection area to control the mass flow through it and reduce the pressure losses due to atomization. Examples for this method are the pintle injector and the dual manifold injection plate.

- The third method uses both a variable injection and a flow control valve. This method was used for the LMDE where a variable area cavitating venturi based flow control valve was used with a pintle injector. The cavitating venturi had a beneficial effect on controlling the system over the wide range of operative thrust.

- The fourth method consisted in on parallel feeding, a pilot one and one actuated with an on-off valve. With this method it is possible to realize a boost-sustain like

No.	Method of Throttling	Primary Variables	Supply Pressure P_s	Chamber Pressure		Pressure Drops				Area Ratio		Throttling Range	Comments
				$*P_{c_1}$	$*P_{c_2}$	ΔP_{i_1}	ΔP_{i_2}	ΔP_{g_1}	ΔP_{g_2}	A_{i_1}/A_{i_2}	A_{g_1}/A_{g_2}		
1	ΔP_i, ΔP_g, A_g	A_g	2235	60	600	15	1500	2160	135	1	1/40	1/10	Excessive supply pressure. For throttling range greater than 1/2.3.
			1000	260	600	65	350	675	50	1	1/8.5	1/2.3	
2	ΔP_i, A_i	A_i	780	60	600	720	180	—	—	1/20	1	1/10	Single proportional control function and satisfactory supply pressure.
			1000	46	600	954	400	—	—	1/20	1	1/13.0	
3	ΔP_i, ΔP_g, A_g, A_i	A_g, A_i	797	60	600	15	150	722	47	1/3.16	1/40	1/10	Two control functions. Satisfactory supply pressure. Large throttling range possible.
			1000	30	600	7.5	150	962.5	250	1/4.57	1/40	1/20	
4	On-off Valve, P_c, Pilot Burner	On-off Valve	750	60	—	690	—	—	—	1/21.4	1	1/10	Satisfactory for step throttling only.
				—	600	—	150	—	—		1		
5	A_i, A_n, ΔP_i	A_i, A_n	750	600	600	150	150	—	—	1/10	1	1/10	Two control functions. 1/10 throttling possible with chamber pressure less than 600 PSIA.
			375	300	300	75	75	—	—	1/20	1	1/20	
			1000	600	600	400	400	—	—	1/20	1	1/20	
6	A_g, A_n, A_3, ΔP_g	A_g, A_n	15,610	600	600	150	15,000	14,860	10	1	1/385	1/10	Two control functions. Excessive supply pressure and governor valve area ratio for 1/10 throttling range.
			1000	600	600	150	350	250	50	1	1/3.42	1/1.53	
7	ΔP_i, A_n, P_c	A_n	750	600	30	150	720	—	—	1	1	1/2.19	Throttling range insensitive to supply pressure. Not recommended as throttling method.
			750	600	60	150	690	—	—	1	1	1/2.14	
			1000	800	30	200	970	—	—	1	1	1/2.19	
			∞	∞	60	∞	∞	—	—	1	1	1/2.24	
			603	600	303	3	300	—	—	1	1	1/10	

ASSUMPTIONS MADE FOR CALCULATIONS:
1. Injector pressure drop (ΔP_i) must be at least 25% of chamber pressure (P_c).
2. Maximum practical governor valve area ratio $\frac{A_{g_1}}{A_{g_2}}$ is 1:40.
3. Maximum injector valve area ratio $\frac{A_{i_1}}{A_{i_2}}$ is 1:20.
4. Characteristic velocity and thrust coefficients are constant over throttling range.
5. Maximum practical chamber pressure is 600 PSIA

* SUBSCRIPTS: 1 — Low thrust operation. 2 — High thrust operation.

PRESSURES: Pounds per Square Inch Absolute — PSIA.

Figure 3.1: Chart of throttling techniques investigated by NASA during project MX-794. [54]

thrust profile or obtain an intermediate thrust level by operating the secondary valve in PWM[1] mode. Usually a dual manifold injection plate is employed.

- The fifth and sixth presented methods are analogous to the second and first one respectively, beside the fact that this time also the nozzle throat area is controlled. This allows to effectively use a single set of injector when a single FCV is employed. The ability to control the nozzle throat area also influence the thrust coefficient efficiency. Of course this technique is quite complicated because of the high temperature nozzle environment. Presently variable area nozzles applications are very limited.

- In the last presented method, the thrust is controlled by varying the nozzle throat area, here the flow to the combustion chamber is reduced because of an increase of injection Δp.

The method presented in this thesis is similar to the first one with two exceptions: the flow control valve used is based on a variable area cavitating venturi and the injection is gaseous. The injection pressure drop is comprehensive of the catalyst pack pressure drop which is the main contributor to these losses. The motor configuration currently

---

1 Pulse width modulation

under study at the hybrid propulsion group is particularly suitable to be implemented with such a method. Firstly by using hydrogen peroxide, which is a storable oxidizer, a cavitating venturi can be employed. This is hardly possible with nitrous oxide and liquid oxygen since a cavitating venturi would be an excessively limiting element for a saturated fluid. [2]. Secondly the use of a catalyst pack to decompose the HTP flowing to the combustion chambers enables to achieve many features:

- With a gaseous injection it is possible to introduce a swirled injector and so achieve a vortex motor which is one of the peculiar high efficiency high regression rate configurations presented in the introduction;

- A gaseous injection in general tends to have a very stable behaviour, there are no droplet evaporation lag instabilities. This is true as long as the catalytic bed performs correctly;

- HTP decomposition temperature reaches temperatures around 1000 *K*, this temperature is high enough to thermally decompose and ignite the commonly used fuels. This make the motor self ignitable and restartable: no pyrogenerators are required and the system can be stopped and started several times.

The coupling between a FCV based on a cavitating venturi with a gaseous injection of a decomposed monopropellant is a favourable configuration to realize a throttleable and restartable HRM.

In this chapter the design of the developed FCV is presented.

3.2   CAVITATING VENTURI CHARACTERISTIC

A cavitating venturi is a venturi tube in which the throat pressure corresponds to the vapour pressure of the fluid transiting through the venturi. This device has been long credited for being a simple and accurate means for controlling the flow of an incompressible fluid. The phenomena happens as the pressure drop through a conventional venturi increases the upstream pressure head is converted into velocity, at some point the residual pressure head is equal to the vapour pressure of the liquid.

The cavitating venturi characteristic equation can be derived from the Bernoulli's equation considering the head balance between an upstream point and the throat:

$$p_{0,up} = p_{th} + \rho \frac{v_{th}^2}{2} + \Delta p_{loss}$$

---

2 Since nitrous oxide, liquid oxygen and hydrogen peroxide are the most commonly used oxidizers when talking about hybrids this makes the use of a CV[3] peculiar to the hydrogen peroxide application

For cavitating venturi the throat pressure is equal to vapour pressure of the operating fluid. By neglecting the losses on the convergent section of the venturi the throat speed can be rewritten as follow:

$$v_{th} = \sqrt{2\frac{p_{0,up} - p_{sat}}{\rho}}$$

The media mass flow through the cavitating venturi can be determined using continuity at the throat:

$$\dot{m} = \rho \, A_{th} \, v_{th}$$

$$= A_{th}\rho\sqrt{2\frac{p_{0,up} - p_{sat}}{\rho}}$$

$$= A_{th}\sqrt{2\,\rho\,\left(p_{0,up} - p_{sat}\right)}$$

Experimentally the measured mass flow through the cavitating venturi is lower than the one computed using the previous equation. To take into account of this difference a coefficient (C_D) is introduced on the mass flow equation resulting in the well known cavitating venturi characteristic equation:

$$\dot{m} = C_D \, A_{th}\sqrt{2\,\rho\,\left(p_{0,up} - p_{sat}\right)} \tag{3.1}$$

In this work C_D is referred to as discharge coefficient, in literature C_D can be called orifice coefficient or flow coefficient. Beside being a variable introduced to take into account of the difference between theory and reality, the discharge coefficient considers many flow effects:

- Because of the vapour formation at the venturi throat, the liquid passage area is often reduce, resulting in a smaller equivalent throat area. This effect is commonly referred to as vena contracta.

- The neglected losses on the Bernoulli's equation can have a relevant effect on the mass flow. Experimentally these are taken into account in the discharge coefficient.

There are instances in which these two effects are related. One example are the drilled injection holes of a cavitating injection plate, where the convergent is normally absent and it is replaced by a sharp edge entrance: the convergent efficiency is very poor and the sharp entrance affects the vena contracta, reducing consistently the throat area. In this case the discharge coefficient can have values as low as 0.6.

Equation 3.1 describes the mass flow through the cavitating venturi when the liquid at the throat cavitates. In this instance the flow through the cavitating venturi does not depend on the downstream pressure. Because of the analogy with the sonic flow through a rocket nozzle, the flow is said choked. When this condition no longer occurs the flow is said unchoked. The main reason why the cavitating venturi is a simple and accurate

method to control the flow is that when the venturi is choked there is no dependence between mass flow and downstream pressure. Of course a determinate pressure drop must be accepted in order to choke the flow. This aspect is particularly important in hybrid rocket motor testing. Normally, when testing a HRM the oxidizer tank and pressurization system are not the same of the flight model, as a consequence any possible coupled instabilities that can rise are not of interest for the test and could be potentially dangerous. Another aspect highlighted by equation 3.1 is that the cavitating venturi can be hardly used when the operating fluid is saturated or near saturation. Because the driving potential of 3.1 is the difference between the total upstream pressure $p_{0,up}$ and the saturated fluid or vapour pressure p_{sat} the required throat area would be excessive, resulting in a device that is heavy and cumbersome.

Normally the limit to which the characteristic equation is applicable is defined using the ratio between the maximum downstream pressure at which the flow is still choked and upstream pressure. This ratio is here defined as maximum allowed back pressure (MABP[4]) ratio, and it is a characteristic of the cavitating venturi. The MABP ratio depends on many aspects, the most important one is the divergent efficiency. On VACV[5]s an important part is played by the method used to alter the venturi throat.

Determining the discharge coefficient C_D and the MABP ratio can be performed experimentally or numerically. Numerical simulations supported by CFD[6] methods can aid the design of the flow control valve itself. Such a method has been attempted in this work, but because of the lack of time necessary to carry out all the required numerical simulations this approach was later abandoned. The obtained partial results are presented in the next session.

3.3 FIXED THROAT CAVITATING VENTURI

Many reasons led to the design and testing of a fixed area cavitating venturi before the realization of a variable area cavitating venturi to be used as a flow control valve:

- It served as a benchmark for the design of the variable area cavitating venturi. The initial idea was to perform a series of experimental tests to characterize the fixed throat cavitating venturi discharge coefficient and maximum allowed back pressure ratio. Then carry out a numerical simulation campaign to obtain a suitable CFD model able to predict correctly the desired characteristics and in the end use the CFD model to carry out a series numerical simulations to support the VACV design.

---

4 Maximum allowed back pressure
5 Variable area cavitating venturi
6 Computational fluid dynamic

- At the time a new, large scale, hybrid rocket motor was being designed at the hybrid propulsion group. The experimental set up needed a cavitating venturi to perform constant thrust fire tests. This created a good opportunity to validate the foreseen numerical model.

3.3.1 *Design*

The designed fixed throat cavitating venturi consisted in a four pieces assembly: two inserts that fixed the venturi internal geometry and a two piece shell to act as an insert holder. This configuration that is shown in figure 3.2, is a flexible configuration that allowed to test many different internal geometries, and in particular allow to use various throat diameter venturi inserts.
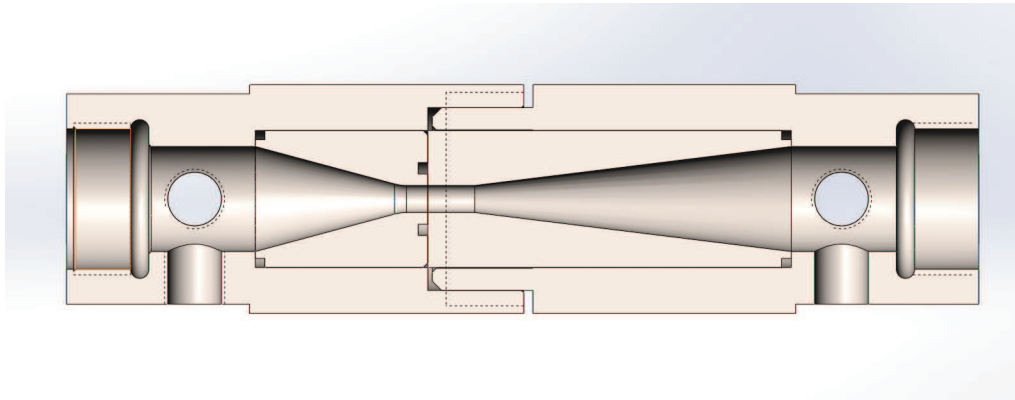

Figure 3.2: CAD model crossection of the fixed throat, four piece, cavitating venturi.

Moreover the venturi was realized in two inserts in order to enable the precise measurement of the throat diameter. Of course a frontal cut at the throat required some precise manufacturing, with reduced clearance between insert and holder. A conventional frontal O-ring sealing was placed between the two inserts while two reduced room frontal O-ring sealing avoided leakage between inserts and holder. The divergent insert was realized with a divergence angle of $14°$, the convergent one with a convergence angle of $30°$. These geometrical parameters were set following the good practise design for cavitating venturi presented by Randall in [48]. Because the required oxidizer mass flow was 2.2 kg/s and a maximum operative combustion chamber pressure equal to 25 bar a venturi throat diameter of 6 mm was selected. The discharge coeffcient using in the determination of the throat diameter is 0.9. The upstream operative pressure was selected starting from the downstream operative pressure and taking into account for a ratio between downstream

and upstream pressure of 0.85.[7] The venturi was manufactured and integrated with the fluidic line for the large scale test motor.

3.3.2 *Steady state experimental characterization*

A set of cold tests were carried out, these were aimed to characterize the cavitating venturi. Because the time for this characterization was limited, in the results that follows are reported also mass flow data from fire tests.
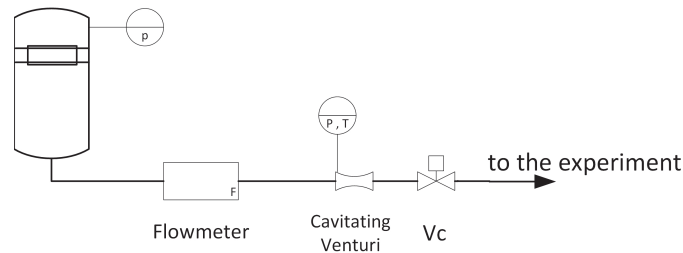

Figure 3.3: The scheme of the experimental set up used during the fixed throat cavtating venturi characterization.

Figure 3.3 represents the experimental setup used to characterize the fixed throat cavitating venturi. It consists of a pressurized oxidizer tank, which pressurization take into account for the pressure losses in the fluidic line, a ultrasound flowmeter which outcome is used to verify the oxidizer mass flow through the venturi, the cavitating venturi to be characterized and then a pneumatically actuated ball valve used to start and stop the test. During this experimental characterization a set of 8 useful test were performed, the results obtained and the relative uncertainty due to measurement errors are reported in table 3.1. The maximum allowed back pressure ratio for the cavitating venturi was determined and equal to 0.82. This characteristic was possible to obtain thanks to a set of experimental fire test. The amount of back pressure was controlled by setting the combustion chamber pressure. This was achieved by setting the appropriate nozzle throat diameter.

3.3.3 *Numerical simulations*

A series of numerical simulations was performed on the fixed throat cavitating venturi. A commercial solver ANSYS fluent was used to perform the CFD simulations. The mesh for the fluid domain was realized using ICEM, this was a structured mesh with quadrangular elements. The analysed domain contained was bidimensional axialsymmetric

---

7 This ratio will be explained later in this work, but it is known as back pressure ratio and it is an important operative parameter for the cavitating venturi.

and representative of the the region upstream and downstream of the throat with an area ratio of 9 with respect to the throat. The mesh used normally have a number of nodes around 400k. The model used to simulate the cavitation and biphase flow was a 2 parameters Schnerr-Sauer model[27]. The parameters that fluent allows to modify are the fluid vapour pressure and the bubble density number. The vapour pressure for an hydrogen peroxide acqueous solution was determined in literature, the value used during the numerical simulations is 305 Pa, which is the vapour pressure of 90% HTP at $20°C$. For what concern the bubble density number, at the beginning the default value preset in fluent was used, afterwards the number was increased in order to have a good correlation for the discharge coefficient with the experimental one. The results presented are relative to simulations with a ratio between downstream and upstream pressure of 0.7. A 2 equations $k - \epsilon$, non equilibrium wall function model was used to simulate the internal fluid dynamic. A mass flow boundary condition was imposed to the inlet and a pressure boundary condition to the outlet.
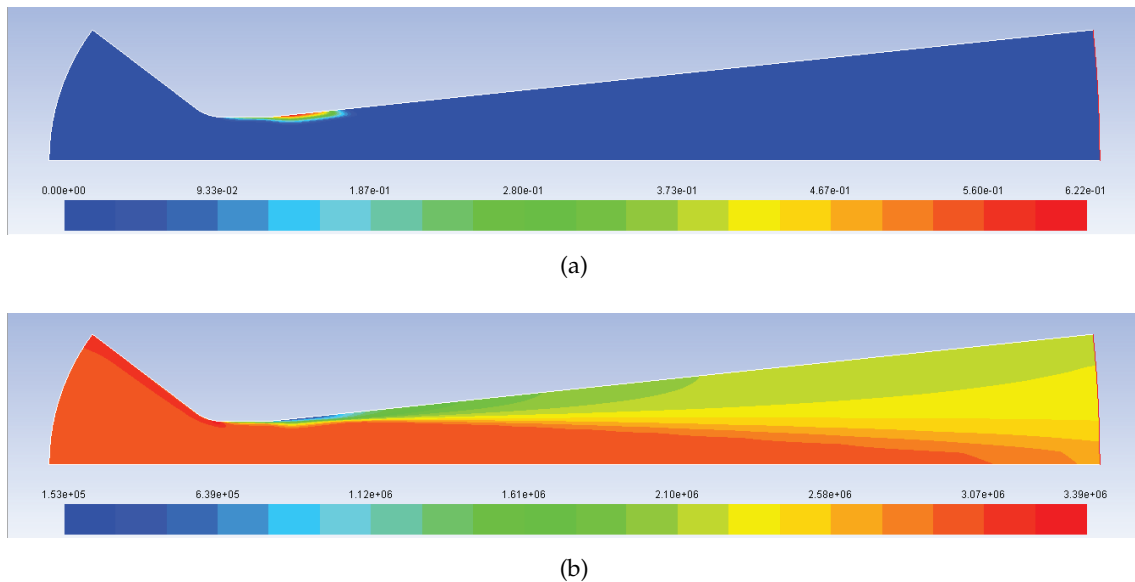
(a)

(b)

Figure 3.4: Results of a CFD numerical simulation of the cavitating venturi: on top vapour title contour and on bottom total pressure distribution.

Figure 3.4 shows the results of one of the performed CFD simulations with the afore described numerical model. The first one represents the vapour title in the fluid domain. It is possible to see the cavitation region inside at the throat and the relative vena contracta. Cavitation starts at the throat but then it continues further in the downstream region where it reaches a maximum. The second figure is the total pressure contour. Beside the cavitation region being characterized by a very low total pressure it is possible to see that the core region conserves a higher amount of total pressure, this is compatible with the high speed jet type of cavitation presented in [48].

test n°	1	2	3	4	5	6	7	8
$\dot{m}_{ox}$ [kg/s]	2.347	2.182	2.288	2.319	2.053	1.978	2.068	1.968
p_{up}° [bar]	29.15	26.76	28.64	28.87	23.17	21.89	23.37	22.30
exp. C_D []	0.9185	0.8912	0.9046	0.9132	0.9026	0.8933	0.9038	0.8850
unc. C_D []	0.0266	0.0257	0.0271	0.0283	0.0275	0.0307	0.0269	0.0273
num1 C_D []	0.9544	0.9491	0.9398	0.9473	0.9588	0.9456	0.9544	0.9360
num2 C_D []	0.9125	0.9088	0.9138	0.8953	0.9047	0.9047	0.9082	0.8968

Table 3.1: Experimantal and numerical results of the preliminary cavitating venturi characterization.

Table 3.1 shows the experimental and numerical results obtained during this cavitating venturi characterization. The first and second lines represent the measured oxidizer mass flow and upstream total pressure. The experimental computed discharge coefficient and respective uncertainty follows on the third and fourth rows. The fifth row (num1 C_D) is the obtained numerical discharge coefficient when the default fluent bubble number density was employed. It is possible to note that the numerical C_D is quite higher than the experimental one. In order to have a good correlation between the experimental and numerical results, the bubble density number was raised. The bubble density number affects the numerical value for the discharge coeffient. For the geometry is always the same this implies a change of the size of the vena contracta. Once a good correlation was found the numerical simulations were repeated to see if the trend was still respected. The CFD results for the second series of numerical simulations are reported in the last row of table 3.1.

It is important to note now that the initial strategy to aid the design of the VACV by employing numerical simulations was not pursued for the following reasons:

- As a part of PhD Students formation plan, we must follow some interdisciplinary seminars. In one of these I had the pleasure to discuss about the application of RANS models on CFD numerical simulations with Professor Francesco Picano, one of the major experts in biphasic numerical simulations in Europe. During this seminar Professor Picano pointed out how the solution obtained with RANS models are extremely limited, it is true that their accuracy can be improved by handling the model parameters, but it is equally true that the obtained parameters could not possibly be used in a numerical simulation with a different fluid domain. Hence neglecting the effectiveness of the desired initial strategy.

- At this point the end of the first year was approaching. Numerical simulations would have drained essential time to be dedicated to other activities involved in the project.

The design of the flow control valve based on the variable area cavitating venturi followed, but instead of being supported by numerical simulations a flexible design was adopted, in order to enable the system to be modified if needed.

3.4   VARIABLE AREA CAVITATING VENTURI

As previously declared, the flow control valve developed during this thesis work is based on the variable area cavitating venturi (VACV). With a VACV it is possible to control precisely the choked flow through the venturi. This is achieved by varying the venturi throat area. There is an almost linear dependence between throat area and oxidizer mass flow as it can be seen from the cavitating venturi characteristic equation (Eq. 3.1). This dependence is almost linear because the discharge coefficient C_D slightly varies for a variation of the venturi throat area. It is worth to note that among the involved variables in equation 3.1 two can be used to control the oxidizer mass flow through the cavitating venturi: throat area and upstream total pressure. Because of the linear dependence the throat area is a good candidate to be used as control variable: it simplifies the control algorithm. But it is equally possible to use a fixed throat cavitating venturi with a variable upstream pressure. Other than being non linear, using the upstream total pressure as control variable presents some technical difficulties. In most HRM applications the feeding system is pressure fed. With this configuration it is difficult to vary the tank pressure on demand, and the involved volume is quite consistent which suggests a poor reaction time. Varying the upstream pressure would possible if a pump fed feeding system is employed. Coupling a CV with a pump would bring some advantages in terms of feeding stability, but however we must remember of the non-linear dependency between flow and upstream pressure and how the the venturi characteristic curve will couple with the feeding pump one. Since at University of Padova we use mostly pressure fed system, the use of throat are as control variable is the best choice, hence the development of a variable area cavitating venturi. The most commonly used method to realize a VACV consists in a pointed shaped spike, or pintle, that enters the throat of a traditional venturi. When the pintle advances toward the venturi, the portion of throat area occupied by the pintle increases, which means that the effective throat area is reduced. It is common to identify a linear coordinate defined as pintle stroke to evaluate the position of the pintle with respect of the venturi. The pintle stroke is defined as the distance between the pintle actual position and the closed position in which the pintle touches the venturi throat wall. This distance must be projected on the

pintle actuation axis which is commonly aligned with the venturi bore axis. It is assumed that the pintle stroke increases when the spike moves outward and it has zero value when pintle and throat are in contact. The pintle can have many shapes. Generally it is axialsymmetric and with a conical point. As it will be shown soon, a conical pointed pintle implies a quadratic trend of the throat area with pintle stroke. However this kind of point is the most used because it is easy to manufacture and verify. For a conical
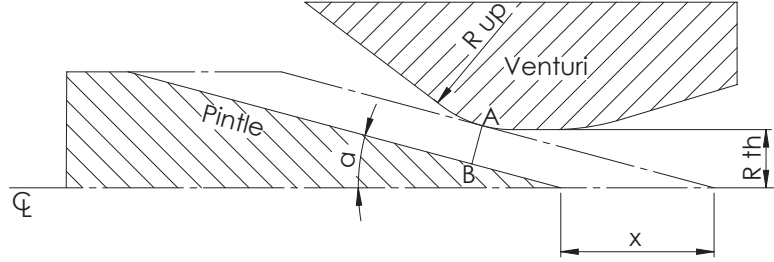

Figure 3.5: Crossection schematic of the throat area for a conical shaped pintle.

shaped pintle the throat area can be assumed as the lateral area of the truncated cone which generatrix is perpendicular to the pintle surface at the frustum. This definition is here explained with reference to figure 3.5.

The throat area is assumed to be the minimum passage area. In the conical spike configuration this is equal to the lateral area of the truncated cone that is generated by the rotation of segment AB around the axis (centerline). In this case the passage area cone has an apex angle equal to $(\pi - 2\,\alpha)$.

The lateral area of a cone is equal to

$$A_{lateral} = \pi\,r\,a$$

And since the relation between frustum (a) and base radius (r) is known ($a = r/\cos\alpha$) the lateral area can be rewrote as:

$$A_{lateral} = \pi\,r^2/\cos\alpha$$

The throat area is the difference of the lateral area of two cones which share vertex and apex angle $(\pi - 2\,\alpha)$. With reference to figure 3.5 the larger cone has a base radius equal to r_A and the smaller one r_B. Where:

r_X is the radial coordinate of a given point X with respect to centerline axis;

A is the venturi wall reference point upstream of the throat where the sloop of the rounded edge is equal to α (pintle half apex angle);

B is the pintle wall reference point which is defined as the point of minimum distance from A on the actual pintle frustum.

Hence the throat area as difference of the defined cones lateral area is:

$$A_{th} = \frac{\pi}{\cos \alpha} \left(r_A^2 - r_B^2 \right)$$

The radial coordinate of point A is computed from the throat radius incremented by a portion of the throat sagittal radius:

$$r_A = R_{th} + R_{up} \left(1 - \cos \alpha \right)$$

The radial coordinate of point B is computed from r_A decreased by radial component of segment AB:

$$r_B = r_A - AB \cos \alpha = r_A - x \ \sin \alpha \cos \alpha$$

Introducing the derivation of r_B in the definition of A_{th} we have

$$
\begin{aligned}
A_{th} &= \frac{\pi}{\cos \alpha} \left(r_A^2 - (r_A - x \ \sin \alpha \cos \alpha)^2 \right) \\
&= \frac{\pi}{\cos \alpha} \left(r_A^2 - r_A^2 + 2 \ r_A \ x \ \sin \alpha \cos \alpha - x^2 \ \sin^2 \alpha \cos^2 \alpha \right) \\
&= \frac{\pi}{\cos \alpha} \left(2 \ r_A^2 \ \sin \alpha \ x - \sin^2 \alpha \cos \alpha \ x^2 \right)
\end{aligned}
$$

So to conclude the venturi throat area for a conical pintle is described by the following equation:

$$A_{th}(x) = \pi \left(2 \left(R_{th} + R_{up} \left(1 - \cos \alpha \right) \right) \sin \alpha \ x - \sin^2 \alpha \ \cos \alpha \ x^2 \right) \tag{3.2}$$

where α is the apex half angle, R_{th} is the throat radius, R_{up} is the upstream throat radius (in the sagittal plane) and x is the pintle stroke, from the position in which the pintle touches the venturi.

Equation 3.2 shows how for a conical shaped pintle the throat area function is non linear with the stroke, in particular it is quadratic. The non-linearity term can be reduced, two methods are here analysed:

REDUCE THE PINTLE APEX ANGLE since $\sin^2 \alpha \cos \alpha \ \cos \alpha$ tends toward 0 faster than $\sin \alpha$ for $\alpha \to 0$, by decreasing the apex angle (2α) it is possible to increase the linearity of equation 3.2 over the same range of pintle stroke. This strategy has a major drawback. There are mechanical/structural limits to how far the apex angle can be reduced. Furthermore these limits are met not only during the operational life of the VACV but also during manufacturing. For the most common method to manufacture a pintle is turning, the structural abovementioned mechanical limits are often met during the manufacturing phase.

OVERSIZE THE VACV An increase of the term $\left(R_{th} + R_{up} \left(1 - \cos \alpha \right) \right)$ of equation 3.2 implies a higher weight of the linear term. This from the practical point of view means to realize a oversized VACV and reduce the operative pintle stroke.

During the design phase of the VACV both the presented methods were used. The pintle cone apex angle was reduced to the minimum guaranteed by the manufacturer, and the venturi throat area was slightly oversized in order to reduce the effects of non linearity over the operative mass flow range. Hence reducing the operative pintle stroke.
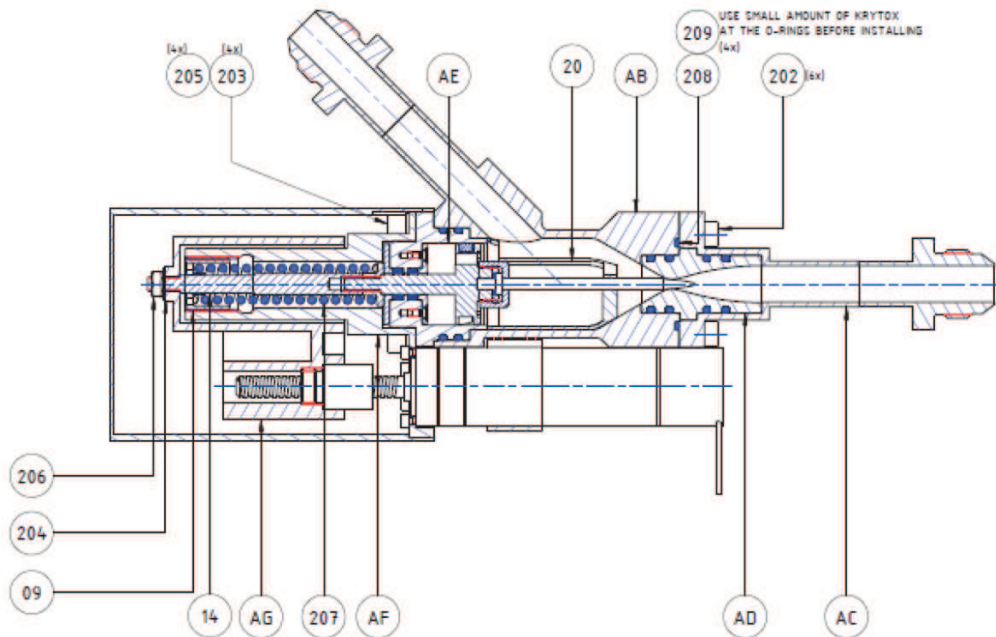

Figure 3.6: MOOG-Bradford FCV developed during FP7 SPARTAN project. To mitigate non linearity effect between oxidizer mass flow and pintle stroke this VACV employ a paraboloid pointed pintle.

If the non linearity implied by the use of a conical pointed pintle is unbearable and oversizing the system is not an option, it is possible to use a differently shaped pintle. In particular a paraboloid shape will increase the linearity of the throat area with the pintle stroke. MOOG-Bradford developed a FCV based on a variable area cavitating venturi [15] on the frame of EU FP7 SPARTAN Project (a project funded by the European Union)[57]. In their device they characterized both a conical and paraboloid pointed pintle. With the paraboloid pintle they found a linear relationship between oxidizer mass flow and pintle position when the flow is chocked. Another advantage of the paraboloid pointed spike is that it is more robust that a conical one. On the other hand it requires a higher manufacturing level and it is very difficult to verify the manufacturing accuracy.

3.4.1 *Design*

The design phase of the VACV started with the definition of the operative requirements defined on table 3.2.

Minimum oxidizer mass flow	30 $[g/s]$
Maximum oxidizer mass flow	300 $[g/s]$
Nominal operative pressure range	50 ÷ 80 $[bar]$
Maximum operating pressure	90 $[bar]$

Table 3.2: Table of requirements for the variable area cavitating venturi design

The maximum operative oxidizer mass flow is set to 300 g/s for two reasons: firstly this mass flow corresponds to a thrust of nearly 1 kN in vacuum at the optimal o/f, this thrust level is reasonable for a lab-scale test motor; secondly it is a reasonable HTP mass flow that can be processed by the catalytic bed that is currently used for the test of small (up to 1kN) hybrid rocket motors at the University of Padova Hybrid Propulsion Group. The minimum oxidizer mass flow was derived from the maximum one knowing that the desired throttling ratio was about 10:1. For what concern the operative pressure, this requirement was set starting from the required maximum combustion chamber pressure between 35 and 40 bar. Now if we analyse the fluidic line pressure drop upstream of the combustion chamber we have the following contributes:

- Injection plate pressure drop (gasseous injection). This term is particularly relevant if a swirled injector is employed;

- Catalyst pack pressure drop. This fundamental component that is employed to decompose the incoming peroxide implies a pressure drop.

- Downstream to upstream pressure ratio. Normally VACV can operate with a maximum value of such a ratio after which the flow is unchocked.

So starting from the combustion chamber pressure the injection plate and catalyst pack pressure drops are added and the achieved pressure is divided by the maximum allowed back pressure.

$$p_{0,up,nom} = \left(p_{cc} + \Delta p_{inj} + \Delta p_{cat} \right) / MABP$$

It must be noted that, at this point of the flow control valve development, not all the terms required to fully evaluate the nominal venturi upstream pressure were known. In particular the catalytic pressure drop (Δp_{cat}), which is strongly dependent from the oxidizer mass flow through it, was determined only for an oxidizer mass flow range from 40 to 110 g/s. A semi-empirical model has been developed within our research group to determine some operative parameters of the catalyst pack employed, among them the catalyst pressure drop. Unfortunately this model was not available when the requirements for the VACV were defined, hence the required maximum pressure drop was determined with a linear extrapolation of the available experimental data. The injector pressure drop

has been determined using gas dynamic equations and considering that the acquired kinetic energy is dissipated. Experimental data on swirled injectors show a very good correlation with theoretical model. The maximum allowed back pressure ratio used during the requirement definition is 0.8 which was a conservative value generated from an analysis of the values reported in literature and the experimental ones that were determined for the fixed area cavitating venturi previously described.

As many other components that build up the fluidic line, the maximum operating pressure (last requirement for the VACV) was set to 90 *bar*. This is normal for all the components that are designed in-house and integrated to the oxidizer line. It is also a pressure level that we can easily reach with our experimental pressurization system in order to qualify the components. The oxidizer tank integrated in the experimental set up is equipped with a 100 *bar* bursting disk. The VACV configuration adopted for the
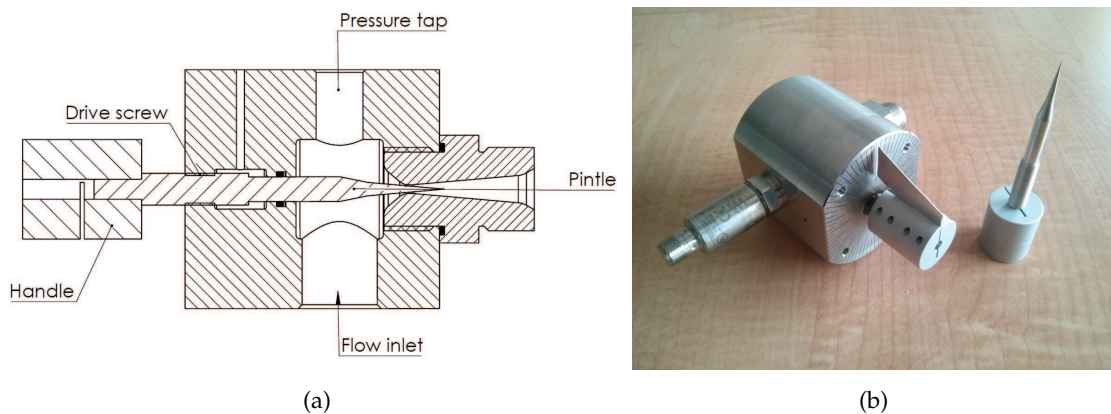

(a)   (b)

Figure 3.7: Variable area cavitating venturi scheme on the left and photo of the VACV and the spare conical pionted pintle on the right. This figures are the first version of the VACV. Some improvements were apported to the final design particularly for what concern the venturi.

realization of the flow control valve is experimental, i.e. heavy, not structurally optimized, flexible in order to allow some design change. Figure 3.7 shows the first version VACV configuration and assembly. It consists of three parts: pintle, main body and venturi.

MAIN BODY The main body consists in most part of the valve. Its goals are to connect the pintle with the venturi, allow the pintle actuation with specific assembly tolerances, host flow inlet and venturi. On the fore face of the main body is also present the interface for the actuation, which consist of four threaded holes.

PINTLE The pintle is the body that enters the venturi throat in order to reduce or vary the throat area and allow the flow to be controlled. For sake of simplicity in manufacturing and quality control the pintle was designed to have a conical shaped point. The pintle is helically moved toward the venturi throat by mean of a drivescrew machined in the main body. An O-ring sealing is used to separate

the wet region of the flow control valve from the drivescrew, and in order to relief the pressure caused by a movement of the pintle a venting hole is machined in the main body.

VENTURI The venturi is a venturi shaped channel carved inside an appropriate fitting and connected to the main body via a screw connection, the sealing is granted by an O-ring placed in a groove at the end of the thread. This type of connection aside from providing an effective sealing also grants the precise and reproducible positioning of the venturi in the main body, which is necessary in order to reduce position uncertainties. The venturi first version resembled a nipple like fitting with BSPP screw connections on both ends. The second version have a smaller venturi divergence angle and allowed it to be connected to the fluidic line with a Let-Lok fitting.

The oxidizer flow enters with an angle of $90°$ with respect to the pintle axis and venturi port. On the opposite side of the entering bore there is a pressure tap to be used with a pressure transducer. This structurally robust and configuration flexible design allows, if necessary, to test many different pintle and venturi configurations. During the development phase of the venturi a second venturi configuration was realized.

Figure 3.7 shows also a rigid coupling that is connected to the pintle. This part served as a handle/knob during the FCV static characterization. An indicator was added to the handle and a goniometer was attached to the fore face of the main body in order to know pintle stroke. This was the VACV situation at the end of the PhD course second year[44]. The venturi throat diameter was computed from equations 3.1 and (3.2). It was assumed for the maximum throat area to be 3/2 of the throat area at which the maximum oxidizer mass flow is achieved. This oversizing was introduced to limit the nonlinearity of the oxidizer mass flow with the pintle stroke. The computed venturi throat diameter is equal to 2.2 *mm*. The pintle apex angle was set to $10°$, this was the minimum angle the manufactured guaranteed. With such geometry definitions the maximum oxidizer mass flow pintle stroke is reached at about 5 *mm* over a 11 *mm* maximum pintle stroke. The maximum pintle stroke was computed as the stroke at which the above-defined truncated cone area is equal to the venturi throat area. Of course the upstream pressure plays an important part in determining the intensity of oxidizer mass flow through the VACV. The throat upstream sagittal radius was set equal to three times the throat radius.

Table 3.3 reports the geometrical parameters for the variable area cavitating venturi. These are outputs of the geometrical design that allow to compute the throat area function with the pintle stroke. Figure 3.8 shows the throat area function with the pintle stroke.

Another aspect that influences the design is the maximum operative pressure. Fortunately this basic structural design is quite robust. Because of the dimensions required to host the fittings and because the geometry was not structurally optimized, the maxi-

Venturi throat diameter	2.2 [*mm*]
Venturi upstream radius	3.3 [*mm*]
Venturi divergence angle	10 [*deg*]
Pintle apex angle	10 [*deg*]
Maximum pintle stroke	11 [*mm*]
Useful pintle stroke	7 [*mm*]

Table 3.3: Output design parameters for the VACV

mum pressure does not represent a problem for the structure itself. The major design limitation to the maximum operative pressure is the clearance between pintle and main body. In fact the sealing between these two components is realized with an O-ring. An excessive combination of clearance, pressure and relative movement between the two components leads to the extrusion of the O-ring sealing from its grove and consequently to a boundless leakage of oxidizer from the FCV. Parker O-ring sealing handbook is a useful tool to design O-ring sealing. For a maximum operating pressure of 90 *bar* and a polymer hardness of 75 § (shore hardness) the handbook defines the clearance extrusion limit to 0.24 *mm*. As a consequence to this limit the manufacturing clearance must lay between 0.11 and 0.13 *mm*.
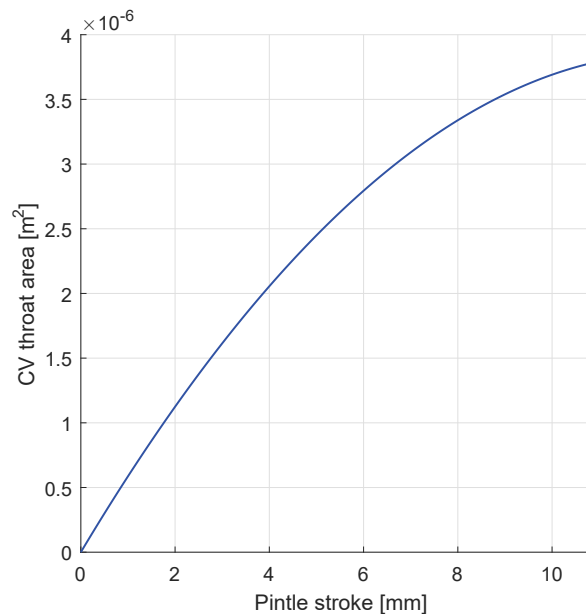

Figure 3.8: VACV throat area with the pintle stroke.

Other aspects relative to the design are the used materials. Hydrogen peroxide is safe to use as long as it is in contact with compatible materials. The manufactured

components are made of AISI 316 L stainless steel, while the O-ring sealing are made of fluoroelastomer (FKM[8]) also known with registered name of Viton. Both this two material are long term compatible if properly cleaned and passivated.

3.4.2   *Pintle positioning errors and manufacturing tolerances*

Figure 3.8 represent the theoretical throat area function, but there are some aspects that must be taken into account: manufacturing tolerances and relative uncertainty of pintle positioning. Because of these two conditions it is possible to know the actual throat area with a relative confidence margin.

Let us analyse the design presented in figure 3.7, we can see that there is a relative positioning between pintle and main body, and there is a connection between venturi and main body as well. This two relative positions build up to create relative positioning error between pintle tip and venturi throat. On the venturi side, the position uncertainty is defined by the thread tolerance and relative position in the main body of the VACV. The thread is a 1/2" BSPP with a manufacturing class A, which implies an axial uncertainty of $22\mu m$ But because the venturi is tightened to the main body as long as the bolting preload occur this axial position uncertainty can be neglected. On the pintle side of the main body the drivescrew is realized with a M8x1 metric thread connection with a class g6 for the pintle H6 for the main body. Because the pintle-main body coupling is liable, the overall connection axial clearance must be taken into account when considering the pintle axial position uncertainty. With these two thread classes the overall pintle axial uncertainty is equal to $34\mu m$. This is an effect that must be considered when analysing the VACV throat area uncertainty. Another source of uncertainty on the pintle axial position is the accuracy to which the pintle rotation angle is known and this is directly correlated with the feedback sensor accuracy.

Other aspects that influence the accuracy of the throat area function are the manufacturing tolerances, in particular the one related to the driving geometrical parameters: pintle apex angle, venturi throat diameter and throat upstream sagittal radius. All these sources have their way to influence the combined throat area uncertainty.

Figure 3.9a shows the contribution of every source to the combined throat area uncertainty with the pintle stroke. It is worth noting that the contribution on the pintle position (x) is dominant for low pintle strokes, while the most contributing source for high pintle strokes is the vernturi throat diameter uncertainty. The manufacturing tolerance on the pintle apex angle plays a moderate role reaching a 10% top influence for the intermediate strokes. The contribution of the throat upstream sagittal radius is almost negligible.
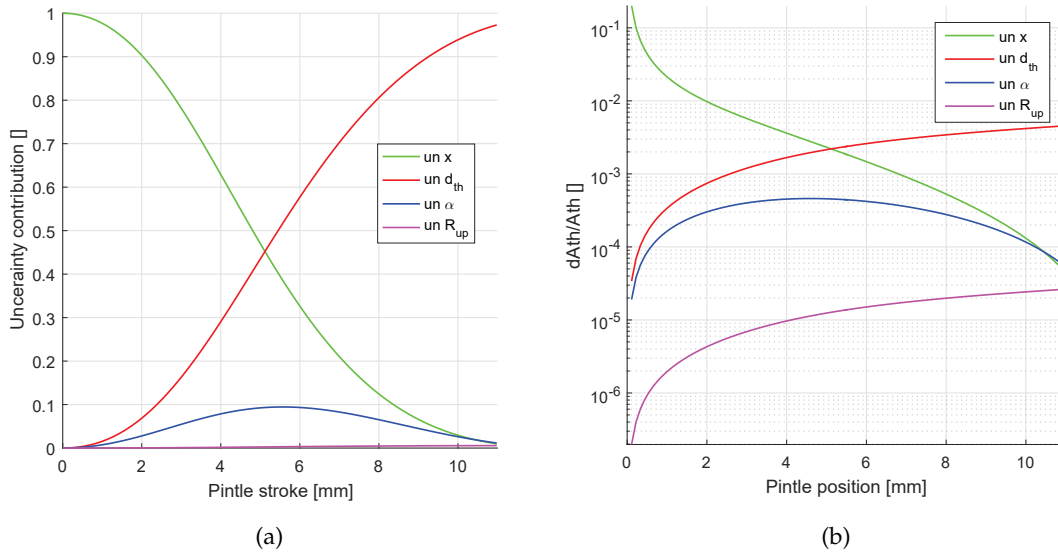
---

8 Fluorocarbon monomer

Figure 3.9: Throat area uncertainty due to pintle positioning errors and manufacturing tollerances. On the left the uncertainty contribution for every single source with the pintle stroke. On the right the influence of throat area uncertainty over the throat area with the pintle stroke.

Overal uncertainty and contributions have been computed with the error propagation or Kline-McClintock formula [33].

On figure 3.9b the throat uncertainty over the throat area is reported. The uncertainty explodes for pintle stroke tending toward zero and the major contributor is the pintle stroke uncertainty. This effect implies that the VACV or the flow control valve should be used for pintle strokes lower than 0.25 *mm*.

Figure 3.10 is an update of figure 3.8 with the added 3σ confidence uncertainty. It must be noted that the throat area uncertainty is higher when the pintle is at a greater distance from the closure position. Nevertheless, as it is above-mentioned the influence of this uncertainty is higher for pintle strokes tending toward zero.

3.5 ACTUATION & CONTROL

After the VACV was designed the design of the actuation followed. The actuation configuration is flexible as well, there is a simple interface betweenVACV (the valve body) and actuation[45]. The static part of the actuation can be linked to the four threaded holes interface on the VACV main body while the rotor can be connected directly, or indirectly, to the pintle.

Firstly let us consider the principle of pintle actuation: the drivescrew. This mechanism allows the pintle to move axially, along the venturi bore axis, via a relative rotation between pintle and VACV main body. As mentioned in the previous section the drive-
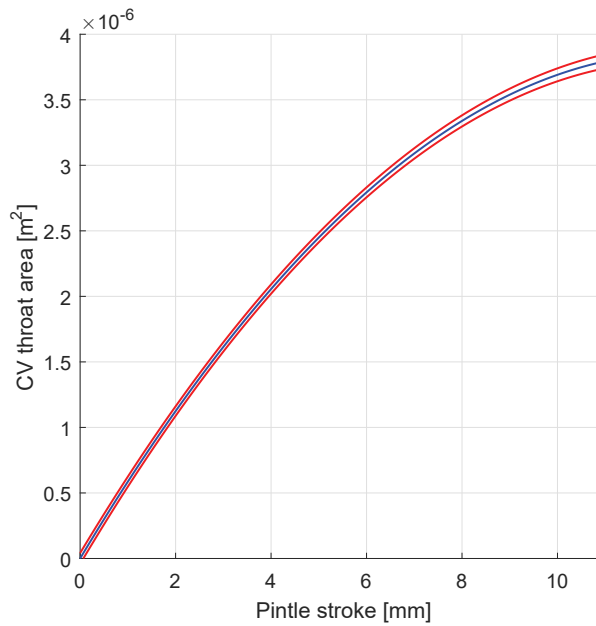
Figure 3.10: VACV throat area and added uncertainty with 3σ confidence with the pintle stroke.

screw is realized with a $M8 \times 1$ metric thread. This thread have a pitch of 1 *mm* which implies a transmission ratio (H)between pintle rotation and pintle advancement of $1.59E - 04$ *m/rad*.

$$H = \frac{pitch}{2\pi}$$

This ratio is very low, drivescrews are mechanism known for their irreversibility meaning that if a rotation implies a translation, the contrary in no longer true, because of the simple presence of friction in the threaded connection. This irreversibility is a main contributor to the safety of flow control valve in case of actuation fail, since, in such an event, the pintle stroke would remain constant. With other type of actuation the upstream pressure would cause the pintle stroke to increase, so that the oxidizer mass flow increases, leading to an involuntary flooding of the combustion chamber, with the consequences it may cause. Because this is the first time a FCV is being developed at UniPD Hybrid Propulsion Group, the choice of using a drivescrew was legitimate by safety requirements. Figure 3.11 shows the complete FCV schematic. On the left the last version and ultimate VACV to be used as flow control valve on the right the actuation. The adopted actuation configuration consists of a step motor connected with an absolute encoder. The step motor is dual shaft. The back shaft of the engine is used to connect the engine with the encoder via a flexible joint. The angular encoder is based on effect Hall and allows to measure the angle of the shaft with an absolute value for 31 turns and a precision of $2°26'$. Motor and encoder stators are connected with an aluminium flange. For what concern the connection between actuation and valve, the front shaft of the step motor is coupled with the pintle using a rigid joint. Step motor stator and valve main
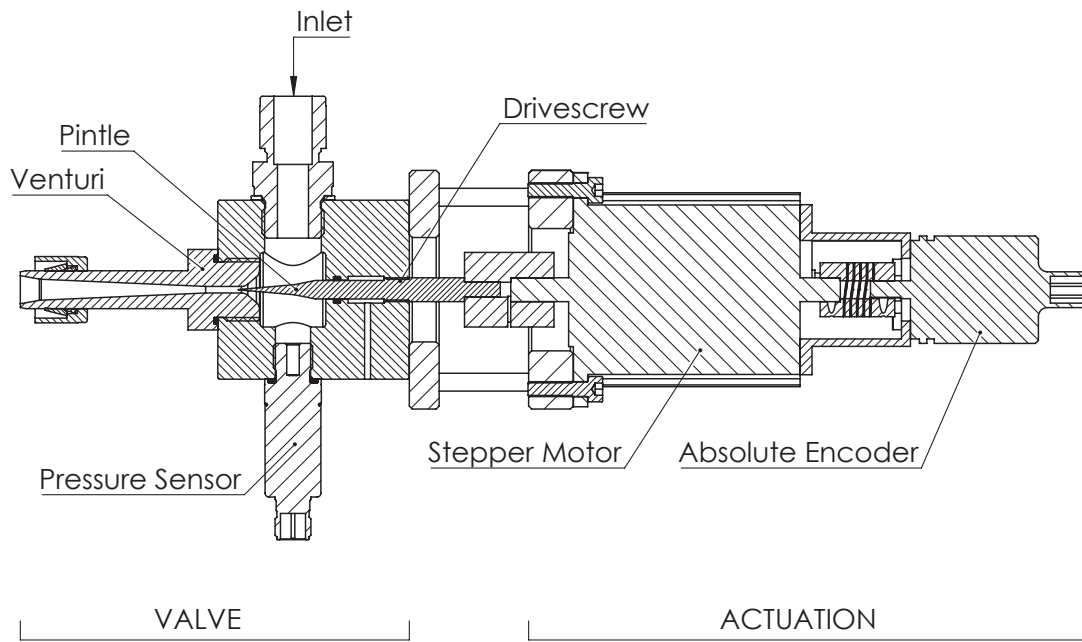
Figure 3.11: Crossection schematic of the complete flow control valve, VACV (valve) and actuation.

body are connected using four rectified bolts that allow the motion of the actuation along the pintle axis while blocking any kind of torque and bending of the actuation.

3.5.1 *Step motor*

A step motor have a very peculiar characteristic curve, it advances of the set step rate until the load torque reaches the pull-out torque. In this instance the motor starts to lose steps, it may advance in rotation as well but the rotational speed is consistently lower than the set one. The pull-out torque for the motor is a limiting parameter. The motor selection started with the definition of the motor requirement torque and speed, then the characteristic curves of the commercially available step motors are analysed and hence motor and power are selected. To evaluate the required torque two different effects must be taken into account: pressure and friction. The pressure force is generated by the resultant of the pressure integral on the pintle surface portion exposed to the fluid, this is equal to pressure times the area generated by the 6 *mm* bore. The work generated by this force is positive when the pintle stroke increases and negative for a decreasing pintle stroke. This force generates a torque on motor rotor proportional to the transmission ratio:

$$T_{press} = H\, F_{press} = H\, MEOP\, \frac{\pi\, d_{bore}^2}{4}$$

The pressure force is also the major contributor to the friction torque. This effect must be evaluated because it is dominant if compared to the sole pressure torque:

$$T_{fr} = F_{press} \frac{\mu_{tf,dry} \; d_{thread}}{2 \; \cos \alpha_{thread}}$$

where α_{thread} is the the thread angle, d_{thread} is the thread diameter and $\mu_{tf,dry}$ is the dry friction coefficient between pintle and VACV main body. The dry friction coefficient was taken into account in order to oversize the system.

With these considerations a total torque of 0.305 Nm is required for decreasing pintle strokes while 0.228 Nm are required for increasing pintle strokes.

Another requirement to take into account during motor selection is the maximum speed rate for the motor. This requirement was set from the objective of reaching a rise time for a step command of 1.25 s. This led to select a motor able to generate a 0.305 Nm torque at a 3.2 rps rotational speed.
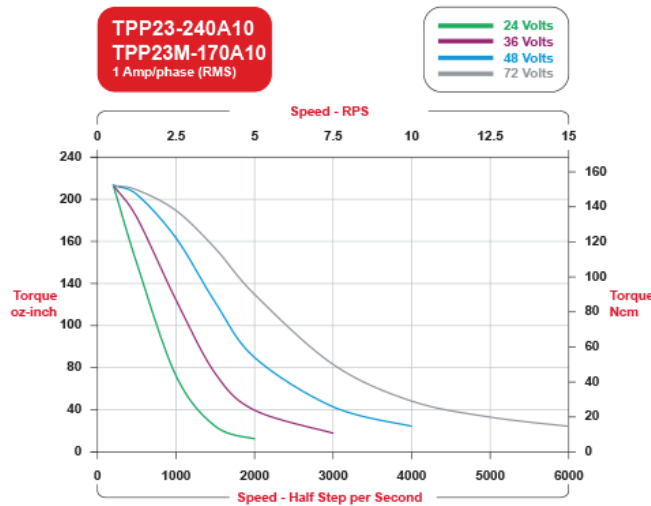

Figure 3.12: NEMA 23 Step motor pullout torque characteristic curve for the selected model

A NEMA 23 step motor was selected. The characteristic curve for the selected motor can be seen in figure 3.12. Among the available DC voltage supplies, 24 V was used. Even if higher voltage supplies lead to better performing characteristic curves with the same motor, 24 V is the limit, in our lab, to which it is possible to operate safely, on prototypes, without too strict safety requirements. The selected motor has a 1.8° step angle, which means 200 $\frac{steps}{turn}$. This is not a limitation in terms of angular resolution and hence pintle stroke because a control unit that allows multistepping is used.

As already mentioned the stem motor is dual shaft in order to have a direct connection between pintle, motor shaft and rotative encoder.

3.5.2 *Feedback sensor*

The pintle actual position is measured indirectly. It is derived from the knowledge of the pintle axis rotation angle with respect of a unambiguous reference position. Many rotation sensors are available, the most diffused ones being the relative encoders. The selection of the rotation sensor was driven by two conditions:

- An absolute encoder was preferred with respect to a relative one for two reasons: firstly in case of power supply interruption and system shut down the actual pintle position is known after system restart. It is possible that this event occurs during a fire test. Secondly we wanted to avoid to recalibrate and reset the system every time the system was "handled improperly". This being the pintle was rotated without power supply or the flow control valve was moved from the experimental set up to storage.

- Because the maximum pintle stroke is 11 *mm* the pintle rotation angle must be determined for 11 turns. This requirement restricted the gamma of choice consistently.
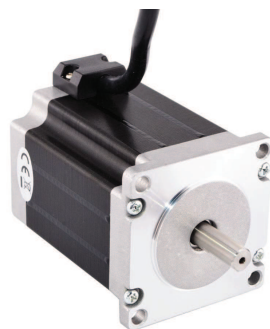
(a)   (b)

Figure 3.13: The selected step motor and absolute encoder for the actuation of the FCV.

The ASM PH36 absolute encoder based on effect hall was selected for the application. This sensor have a very good linearity over the whole operative range, a programmable output and the possibility to measure a rotation angle for up to 31 turns and a good resistance to a vibration intensive environment. Table 3.4 summarizes some of the technical data for the selected encoder.

The overall feedback uncertainty derived by the use of this absolute encoder is 2.43° . This amount was taken into account on the pintle positioning error analysis presented previously and on the data reported in figures 3.9 and 3.10.

Measure range	$31 \times 360°$
Output resolution	16 *Bit*
Repeatability	$0.1°$
Linearity	$\pm\,(2° + 0.015\%\,f.s.)$

Table 3.4: Specifications of the selected absolute encoder.

3.5.3   *Controller*

The flow control valve is controlled using a National Instrument myRIO 1900. This controller is a portable reconfigurable input output device, with 10 analog input channels, 4 analog output and 40 configurable digital input/output. The analog to digital converter resolution, for the analog channels, is 12 bit. This resolution suits the purpose the device is used for: controlling the flow control valve. Of course we do not need all the channels

Figure 3.14: The configurable input-output myRIO-1900 device used to perform the closed loop control of the flow control valve.

available in the device. We use a limited number of channels to acquire the involved sensors signal, control the step motor and interface with the HRM acquisition system:

ABSOLUTE ENCODER A 10 *V* analog input channel is used to acquire the signal from the absolute encoder;

PRESSURE SENSOR A 10 *V* analog input channel is used to acquire the signal from the upstream pressure sensor;

STEP MOTOR The step motor is controlled with a dedicated controller. This controller requires three digital input to: enable the system, control the turning direction and

control the step rate (clock). Three myRIO digital output channels are dedicated to this task.

SYSTEM INTERFACE OUTPUTS The FCV controller communicates some important parameters to the main acquisition system. This communication take place between analog channel. For example a myRIO analog output channel communicates a tension signal to an analog input of the main data logger proportional to the pintle stroke.

SYSTEM INTERFACE INPUTS Normally the pintle actuation is recorded in a program on myRIO. This predefined sequence of commands is started by the use of a trigger which uses a digital input channel.

The controller was programmed using LabVIEW, National Instrument native programming language. NI myRIO-1900 has a field programmable gate array (FPGA[9]) processor. With LabVIEW it is possible to directly program the FPGA. Normally only the task that require a fast processing speed or true parallelism are programmed in FPGA, the other tasks are performed with the real time processor. The communication between the two is performed with the so called scan engine. In this case the motor control is performed with the FPGA while the other tasks are performed with the real time.

3.6 EXPERIMENTAL CHARACTERIZATION

Four different types of characterization were performed on the valve: static, dynamic, maximum allowed back pressure (MABP) and cavitation dynamic instabilities. The experimental set-up used during these characterization is the same except for some minor changes.

3.6.1 *Experimental set-up*

Figure 3.15 shows the experimental setup used to characterize the flow control valve. From upstream to downstream the components are: a high pressure nitrogen tank, the pressure regulation block (consisting of two pressure regulators serially connected), the tank, a series of automated ball valves and, at the end, the variable area cavitating venturi. Downstream of the cavitating venturi there is a needle valve, used during the MABP characterization, and a pipe which connects the valve with a collector tank.

The oxidizer tank design is particular since it allows also to measure the mass flow. It consists of a precisely manufactured cylindrical barrel with two flat bulkhead at its ends. Inside the tank two rooms are separated by a piston the above volume host the
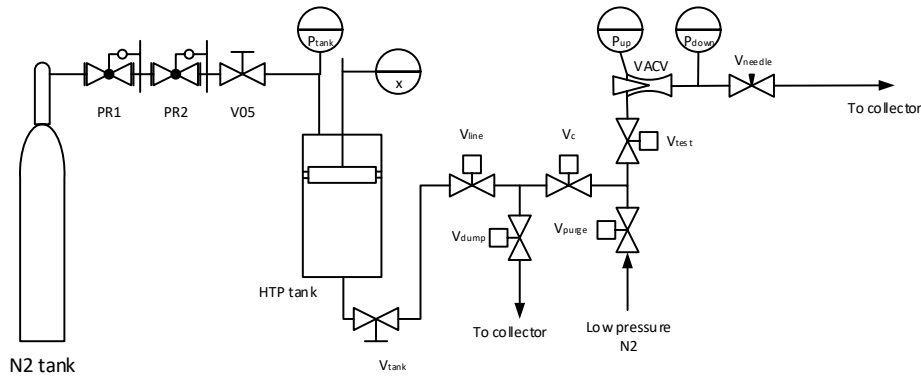
---

9 Field programmable gate array

Figure 3.15: The experimental set-up used during the FCV characterization.

pressurant while the lower volume holds the oxidizer, the impermeability of the piston is granted by specific sealing. Connected to the piston, directed upward, there is a stem which crosses the uppermost bulkhead, the stem is connected to a linear potentiometer. Thanks to the potentiometer output both the instantaneous mass flow and cumulative mass are determined. In order to grant the accuracy of the measure, before each test most of the gas and fluid in the lower volume is vacuum removed before filling up, so to reduce the ullage volume during the test. The tank capacity is four litres.

There are three pressure sensors in the setup: p_{tank} is screwed in the upper bulkhead of the tank, and hence measure the pressurant pressure, p_{up} and p_{down} are placed immediately upstream and downstream of the cavitating venturi. A thermocouple, placed at the tank outlet, measures the outflow temperature in order to compensate the density data and for safety reasons, in case of dissociation, inside the tank. Valves $V05$ and V_{tank} are manually actuated before loading the tank and pressurization. Valves V_C and V_{test} are pneumatically and automatically actuated in this order during the test. Valve V_{purge} is pneumatically and remotely actuated, it allows low pressure nitrogen to flow trough the last part of the line in order to purge this last volume from any residual HTP, during fire test this valve can be used to purge the combustion chamber. The downstream volume, between V_{test} and the engine injection is kept to a minimum. Valve V_{dump} is pneumatically and remotely actuated as well but its function is to empty and depressurize the line volume between V_C and V_{test}. V_{needle} is used to achieve a determinate amount of back pressure with the mass flow during the MABP characterization.

3.6.2 *Static characterization*

The static characterization consists in a series of tests to determine the mass flowing through the flow control valve for different values of pintle stroke and upstream pressure. Three different upstream pressures were analysed: 30, 45, and 60*bar*. The pintle stroke ranged from 0.5 to 10*mm* with a step of 0.25*mm*. The tests were performed using 91%*HTP*,

this happened during the second semester when the actuation was not integrated with the valve yet[44].
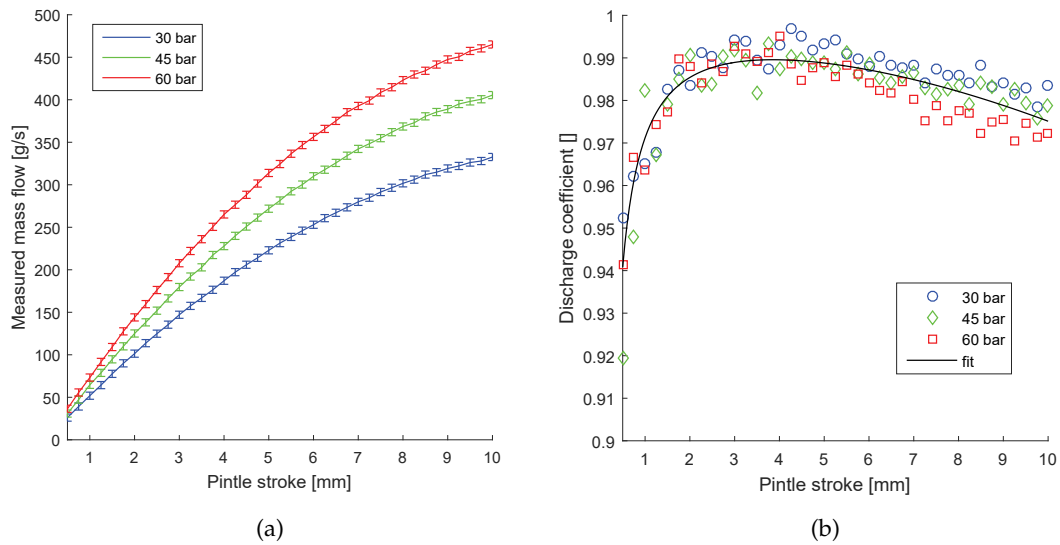

Figure 3.16: Results achieved during the static characterization, on the left the oxidizer mass flow for different valve apertures and operating pressures, on the right the relative discharge coefficient and the fit proposed in eq.3.3

The direct results achieved with the static characterization are reported in Figure 3.16, they are the trend of the oxidizer mass flow and discharge coefficient with the pintle stroke, for the three different upstream pressures. The oxidizer mass flow uncertainty is derived with the error propagation formula [33] from tank diameter, oxidizer density and the potentiometer uncertainty; in most cases it is lower than 4.2 g/s. The values for the discharge coefficient were obtained from the ones of the oxidizer mass flows assuming a venturi throat area that follows equation 3.2. The trends for the discharge coefficient displayed in figure 3.16b are similar for the three pressures even if they appear to be a bit scattered. A fitting function for the discharge coefficient was obtained using the least square method:

$$C_D = 1.003 - 0.7345\,x - 174.5\,x^2 - 3.086 \cdot 10^{-5}/x \tag{3.3}$$

Compared to the experimental data this function has a coefficient of determination R^2 equal to 0.84 indicating an appropriate goodness of fit.

3.6.3 *Maximum allowed back pressure characterization*

During the MABP characterization, the needle valve right downstream of the venturi (V_{needle} in Figure 3.15) was set to a determinate aperture. During the test the venturi started from a position of low mass flow to a higher position with a ramp command. In

this transition the mass flow reaches a level such that the pressure drop across the needle valve is higher than the maximum allowed back pressure, and so the flow through the venturi is no longer chocked, i.e. it doesn't follow Equation 3.1.
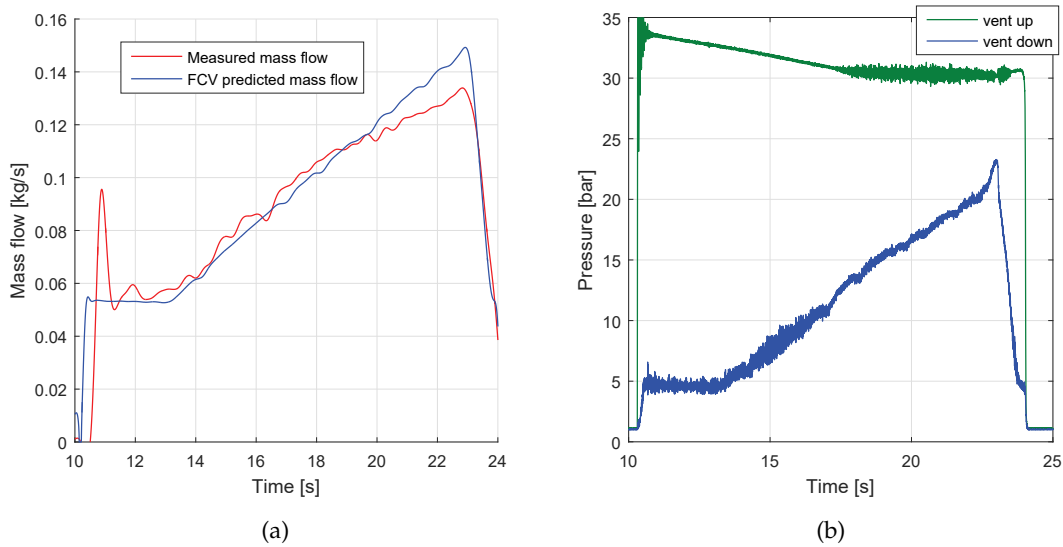

(a)   (b)

Figure 3.17: Oxidizer mass flow and pressure profiles during a typical maximum allowed back pressure test.

Figure 3.17 shows the effects of reaching the MABP on oxidizer mass flow and upstream and downstream pressures. Figure 3.17a shows, when MABP is reached, how the measured oxidizer mass flow (red line) start to differ from the one that is computed using Equations 3.1, 3.2, 3.3, the measured upstream pressure and the effective pintle stroke (blue line). Figure 3.17b reveal how the pressure oscillations propagates from downstream to upstream when MABP is reached and the flow through the venturi is no longer chocked.

A total of 13 tests where performed to determine what is the MABP, for a oxidizer mass flow ranging form 30 to $300g/s$. As for the static characterization, $91\%HTP$ was used. The MABP ratios[10] measured during the 13 tests are displayed in Figure 3.18. The points presented in Figure 3.18 where determined in a graphical way. With reference to Figure 3.17b, the point at which the cavitatng venturi is supposed to be unchocked correspond to the point at which the pressure oscillations intensity is nearly half the final one. No automatic procedure was used in determining the MABP points. Because of this an uncertainty analysis was not performed on these data. At the beginning we believed that the MABP ratio was correlated with oxidizer mass flow (Figure 3.18a), but at a closer analysis it looks closely related to the pintle stroke (Figure 3.18b). The ratio is similar to the $0.8 - 0.9$ value presented by other researchers [48],[50], [51] only for the

---

10 The maximum allowed back pressure ratio is the ratio between maximum allowed back pressure and upstream pressure.
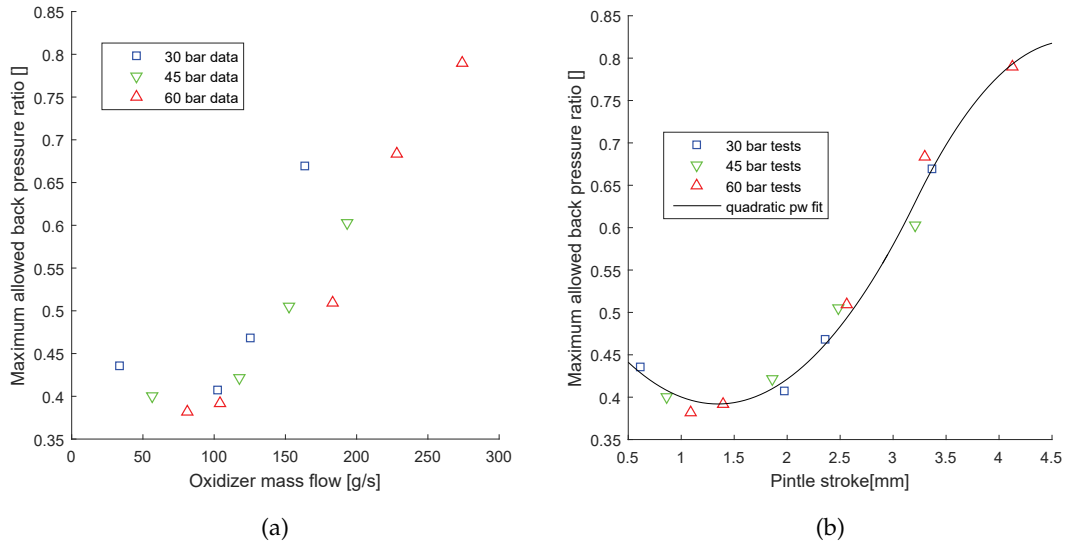
Figure 3.18: MABP ratios with the oxidizer mass flow and pintle stroke for three different up-
stream pressures.

higher analysed pintle strokes, while for the lower pintle positions the ratio tends to
fall, reaching a minimum of 0.4. The trend for the MABP ratio reported in Figure 3.18b
differs from the one presented by other researchers [50], however it must be noted that
also the method used for the determination of these experimental points is different. The
obtained excessively low MABP ratio values could be a problem when the FCV is used
to perform static tests with high combustion chamber pressures and low oxidizer mass
flow (pintle strokes) since an excessive upstream pressure would be required. However,
the presented FCV is suited for throttling where for the higher oxidizer flows we need
the highest MABP ratio. The effective operative ratio between downstream and upstream
pressure then falls linearly of an amount proportional to the throttling ratio.

A piecewise polynomial that fits the obtained data is here proposed:

$$\text{MABP ratio} = 0.51649 - 184.95\,x + 68677\,x^2 \quad \text{for } x \in \left[0.5 \cdot 10^{-3}, 3.2 \cdot 10^{-3}\right[\,m \quad (3.4)$$

$$\text{MABP ratio} = -1.0871 - 813.24\,x - 86658\,x^2 \quad \text{for } x \in \left[3.2 \cdot 10^{-3}, 4.5 \cdot 10^{-3}\right]\,m \quad (3.5)$$

It must be noted that this is a fit of experimental data and does not come from a
theoretical model as previous fit presented in this work.

3.6.4 Cavitation dynamic instabilities

Since cavitation produces severe pressure oscillations one may be concerned by the effects
that the instabilities produced by cavitation could have on the behaviour of the HRM. In
order to properly evaluate this effect the cavitation peak frequencies were determined
for different operating conditions. The experimental setup and experiments for this

characterization are analogous to the one performed during the MABP one. The needle
valve is set with a slightly bigger aperture in order to evaluate the pressure effect on the
bubble dynamic but not to reach the MABP ratio during the FCV ramp command. The
downstream pressure sensor used to analyse the effect of the cavitation was placed as
close as possible to the venturi exit to get the strongest signal.
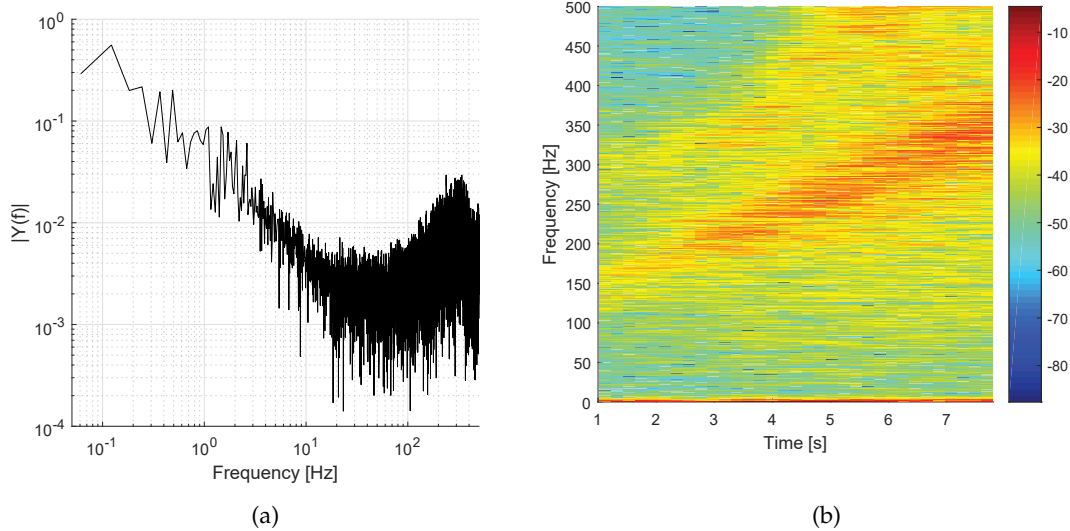

|(a)| |(b)|

Figure 3.19: Fast Fourier transformation of the downstream pressure sensor signal: spectrum and
spectrogram.

Figure 3.19a shows the spectrum obtained from the fast Fourier transformation of
the downstream pressure, over the duration of a whole test. In this case a resonance
peak can be observed at $300Hz$. Figure 3.19b display the spectrogram obtained during
the same test. There is a high spectral density for the lowest frequencies, this is due
mainly to actuation ramp command which varies the downstream pressure because of
the needle valve presence. But the important thing to note about the spectrogram is the
dense region that varies from 150 to $330Hz$ almost linearly with the time. This region is
the one associated with cavitation. We noticed during the MABP characterization that
this region fades away when the maximum allowed back pressure is reached. In both
figure the intensity is in *bar* for the input pressure signal was converted to *bar*.

The peak frequencies at which the cavitation is manifested are reported in Figure 3.20.
They are plotted with respect to the oxidizer mass flow in Figure 3.20a and with respect
to the downstream pressure in Figure 3.20b. As you can see there is a linear correlation
between the measured oscillation peak frequency and the downstream pressure.
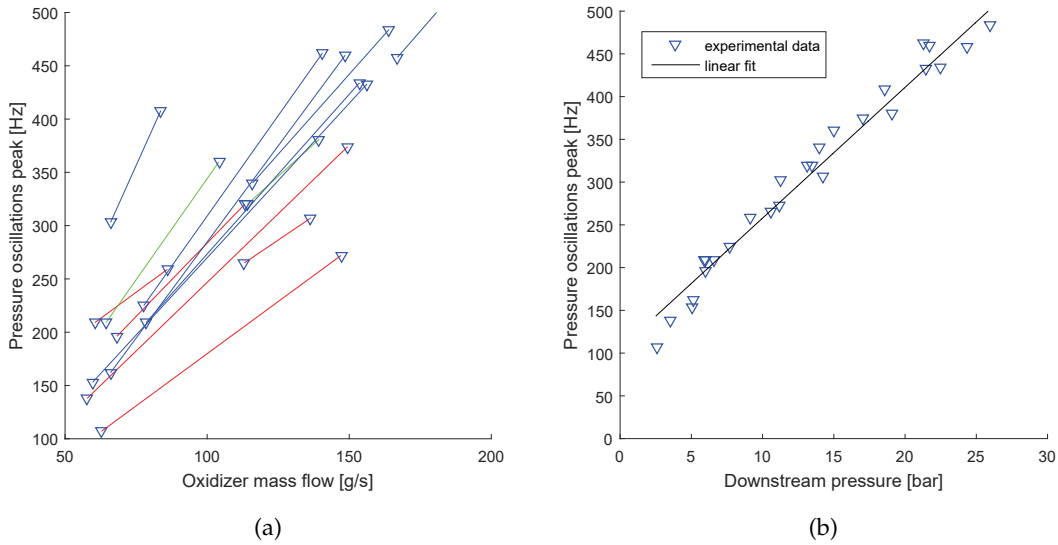
Figure 3.20: Cavitation peak frequencies plotted against oxidizer mass flow (left) and downstream pressure (right)

Using this data an analysis of the effect of cavitation on the whole system can be performed, based on the actual downstream pressure. A linear fit for the peak frequencies with the downstream pressure is proposed:

$$f_c = 105 + 1.529 \cdot 10^{-4} \, p_{0,down} \tag{3.6}$$

The obtained coefficient of determination R^2 is 0.96. It must be considered that for this limited range of downstream pressures the behavior appears to be linear, but this could be no longer true for lower or higher downstream pressures. Bubble natural frequency can be evaluated [9] but it is dependent not only to the local pressure but also to the bubble size at that pressure.

3.6.5 *Dynamic characterization*

The flow control valve is used to control the oxidizer flow to the combustion chamber. It must handle the dynamic oxidizer mass flow at command. The aim of the dynamic characterization is to determine the transfer function of the device. Here the output and input signals for the transfer function are the measured and command mass flows respectively.

In order to gather some information about the transfer function four tests were carried out. The first three consist in a sinusoidal command to the valve, with a frequency of 0.2, 0.3 and 0.4*Hz* respectively, they are aimed to determine the transfer function for these particular frequencies. During the fourth test the command mass flow was an impulse. This has the dual function to determine the rise and fall time of the answer and to get

some more information about the transfer function limitedly to the length of the impulse. The command mass flows where aimed to reach a throttling level of 5 both on sinusoidal and impulse tests.
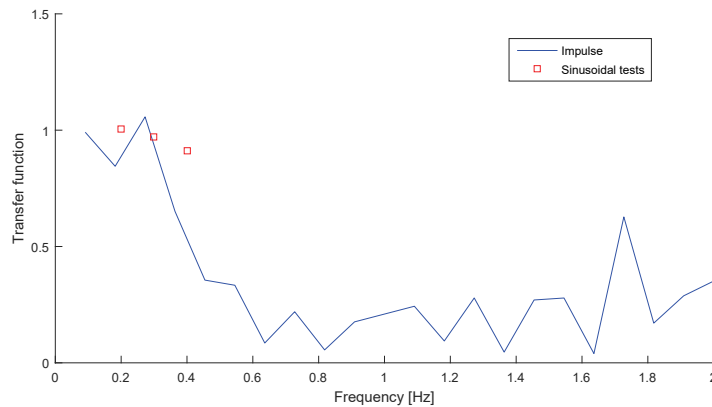

Figure 3.21: Transfer function obtained from the FFT of the impulse test.

Figure 3.22 shows the measured results from the four tests. It can be observed that there are some alterations of the response of the system (delay and magnitude of the oscillations). The fast Fourier transformation was computed for measured and command oxidizer mass flows and for all four tests. From the FFT[11] it was possible to obtain some values of the device transfer function, the results are presented in table 3.5 and figure 3.21.

Transfer function at 0.2Hz	1.00
Transfer function at 0.3Hz	0.97
Transfer function at 0.4Hz	0.91
Rise time from 72 to 288g/s	1.16
Fall time from 288 to 72g/s	1.29

Table 3.5: Results from the FCV dynamic characterization.

In table 3.5 are reported the values of the transfer function for the three sinusoidal tests, the one at 0.4Hz is quite lower if compared to the other two. Table 3.5 also report the values of rise and fall time during the impulse test.

Figure 3.21 shows the transfer function that was obtained from the data transformation of the impulse test. This transfer function has been determined by dividing the FFT of the measured oxidizer mass flow by the FFT of the commanded oxidizer mass flow. Unfortunately since the impulse is too wide[12], the transfer function is well represented

---

11 Fast Fourier Transformation
12 The bandwidth for a rectangular impulse of length $4s$ is $0.25Hz$.
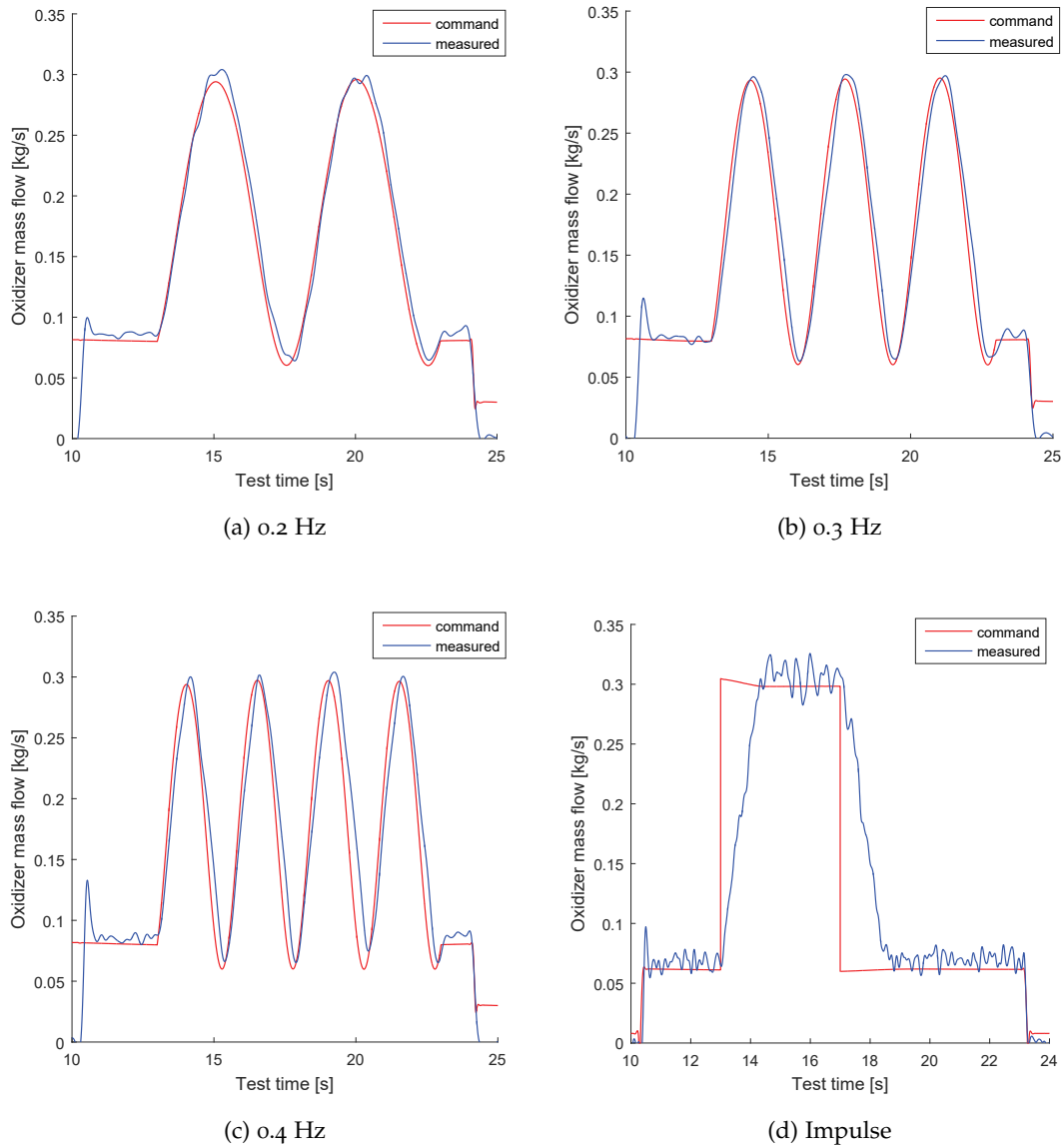
(a) 0.2 Hz

(b) 0.3 Hz

(c) 0.4 Hz

(d) Impulse

Figure 3.22: Oxidizer mass flows during four characterization tests.

only for the lower frequencies. You can see that the values starts to differ already at $0.4 Hz$.

3.7 CHAPTER CONCLUSION

A flow control valve has been designed, manufactured and characterized. The presented flow control valve is based on a variable area cavitating venturi and it is used to regulate the oxidizer flow to the combustion chamber in order to throttle the hybrid rocket engine. The presented design is robust and test-weight, however the performance of the device are representative of the behaviour of a flight-weight valve. A VACV was used as flow control principle because of the inherent advantages of the method: independence

between downstream pressure and oxidizer mass flow (within a determinate limit), linearity of the oxidizer mass flow with the throat area and protection of the system upstream of the venturi in case of an explosive event in the combustion chamber. The actuation of the pintle was achieved by using a drivescrew and a step motor. There is a feedback control loop on the position of the pintle, however the control loop on the thrust is open. Several type of characterization were performed on the flow control valve: static characterization, finalized to determine the characteristic curve and discharge coefficient of the VACV, MABP characterization, aimed to determine the maximum allowable back pressure for the system, cavitation instabilities, to determine which is the peak instabilities frequency due to cavitation and how it varied and, at last, dynamic characterization, finalized to determine some point of the transfer function and the rise and fall time of the system. The performed set of characterizations was aimed to determine how the flow control valve would behave in a static and dynamic condition, what are the limits of its application and what undesirable effects could it have on the rest of the system.

FIRE TESTING

In this chapter the throttling-related fire test campaigns carried out at the hybrid propulsion laboratory are described. Three fire test campaigns where performed: two of them were preliminary for the dynamic throttling fire test campaign. The first two consisted in series of four steady state fire tests, meaning that the engine was not throttled, but a nearly constant oxidizer mass flow was forced to the combustion chamber. The third fire test campaign consisted in the dynamic throttling testing of the motor. The reason why two preliminary fire test campaign occurred is that there was a shift of interest in the hybrid engine configuration. During the first campaign a HTP-paraffin axial injection motor was studied, while in the second campaign the configuration shifted toward a HTP-HDPE engine with a swirled injection. The reason that led to this shift of motor configuration are described in detain in this chapter.

4.1 FIRST PRELIMINARY MOTOR TEST CAMPAIGN

The first preliminary fire test campaign was carried out during the second semester of the second year. The motor configuration in this period is quite different from the final one used to perform the throttling fire tests, in terms of internal configuration and motor case design.

4.1.1 *Motor design & test setup*

Now, let us have a look at the hybrid motor design used in the tests. The combustion chamber case, visible in Figure 4.1, is made of carbon steel and is composed by a cylindrical section and two flanges, which are linked to the cylinder with two pairs of clamps. This type of connection permits a quick assembly/disassembly procedure, allowing an increase in the number of tests per day. A high temperature graphite packing is employed to ensure proper sealing between cylindrical case and flanges. The upstream or inlet flange is directly linked to the catalytic, while the downstream or outlet flange is designed to enclose a graphite nozzle which is hold in place by a steel cap. The nozzle employed in this preliminary fire test campaign is only convergent. At this time the fire test bed was not equipped with a load cell, every performance considerations were carried out by the analysis of the combustion chamber pressure signal. The combustion chamber elements are all designed to withstand a MEOP of 40 bars with a safety factor of 4. One exception to this are the nozzle cap bolts. This are basically burst or rupture bolts

designed to brake in case of a pressure higher than 60 bars. This choice has been made in order to avoid damage to the motor and the experimental setup in the occurrence of an unexpected overpressure event inside the combustion chamber.
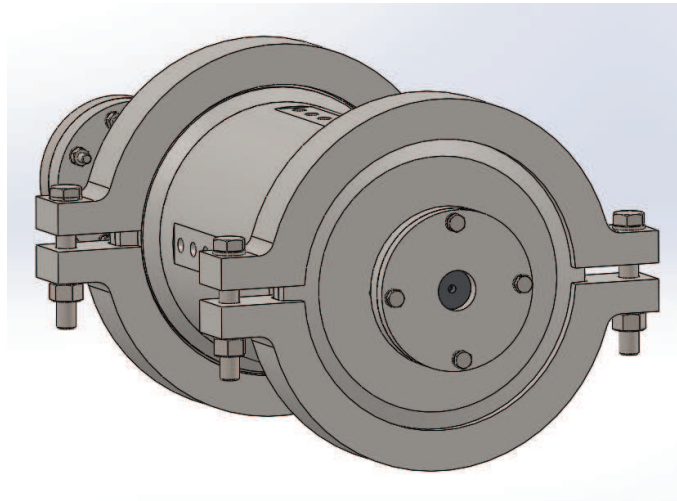

Figure 4.1: A CAD model of the motor case used during the first preliminary campaign.

The combustion chamber presents twenty-two sensor ports allowing to install thermocouples, pressure sensors or other instrumentation devices in order to take accurate measurements inside the chamber during the burn. In particular, the thermocouples cannot be used to monitor the chamber interior temperature because of the too high temperature of the burnt gases; however, if placed inside the paraffin grain at different radii, they can be used as a mean to measure the regression rate. This feature that is included in the motor design is not used for this purpose on this preliminary fire test campaign. Two of this sensor holes are used to determine the combustion chamber pressure downstream of the fuel grain. This motor case configuration allows to insert a cartridge like combustion chamber. It is not possible to present in this work the detailed internal configuration of the combustion chamber because some parts, with particular reference to the post combustion chamber, share some design elements with other motors that were under development at the hybrid propulsion group at the time. However a description is here provided. The cartridge is composed by a cylindrical backup shell that protects the motor case if the fuel grain is totally consumed or if the sealing between the internal components fail. This cylindrical backup shell is made of HDPE and is filled and sealed with the consumables[1]. Starting from upstream to downstream we have: inlet flange thermal protection, paraffin fuel grain, upstream mixer spacer, mixer, downstream mixer spacer, downstream flange protection and in the end the nozzle. All this components, with the exception of the paraffin fuel grain, are made of cotton reinforced phenolic resin commonly known as cotton-phenolic. The use of cotton-phenolic for the realization of the ablative thermal protection is a good compromise between performance and cost, in

---

1 The consumables consist of the ablative thermal protections and the fuel grain.

fact this material has a regression rate three times the one of carbon-phenolic but it costs a fourth. The fuel grain touches the inlet flange thermal protection meaning that during this motor configuration has no prechamber. This choice is a direct consequence of the post combustion chamber configuration. It is true that the mixing between oxidizer and fuel along the grain will be poorer because of the absence of the pre combustion chamber, but an efficient mixing is obtained by using the mixer on the post combustion chamber. On the other hand a post combustion chamber will imply a higher amount of thermal protections on the propellant with the negative effect that it could lead in terms of combustion efficiency and motor performances. Another think to take into account is that the presented design of the combustion chamber is not flexible in terms of combustion chamber length. As a consequence of this fact, because the fuel grain length was longer then the ones normally used with this motor case the post combustion chamber design had to be condensed in the aft end of the motor, this have some consequences that will be described on the testing section. The consumables composing the combustion chamber were joined together using RTV[2] silicones to prevent leakages between them.
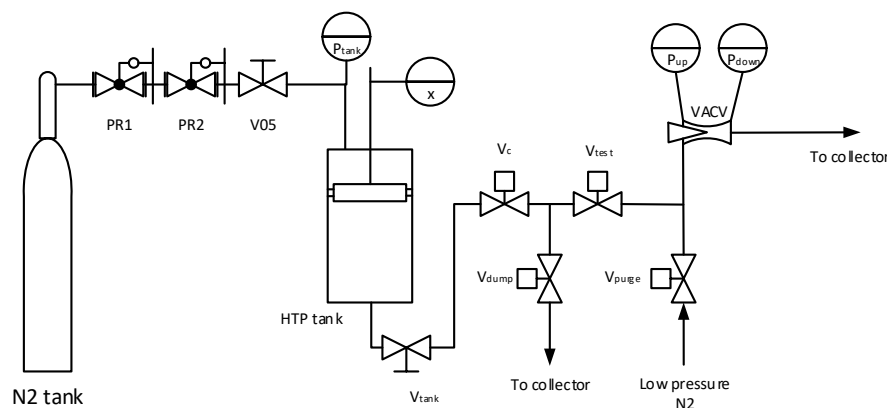

Figure 4.2: The fluidic line used during the three fire test campaigns.

The fluidic line experimental setup represented in figure 4.2 is similar to the one presented during the FCV characterization. From upstream to downstream the components are: a high pressure nitrogen tank, the pressure regulation block (consisting of two pressure regulators serially connected), the oxidizer tank, a series of automated ball valves and, at the end, the flow control valve. The needle valve downstream of the venturi is no longer present because adding a pressure drop is no longer needed, but a ball valve to start and stop the test has been integrated in the line instead.

The oxidizer tank is the same used during the cavitating venturi characterization, other than storing the oxidizer it allows also to measure the oxidizer mass flow thanks to the piston separator position.
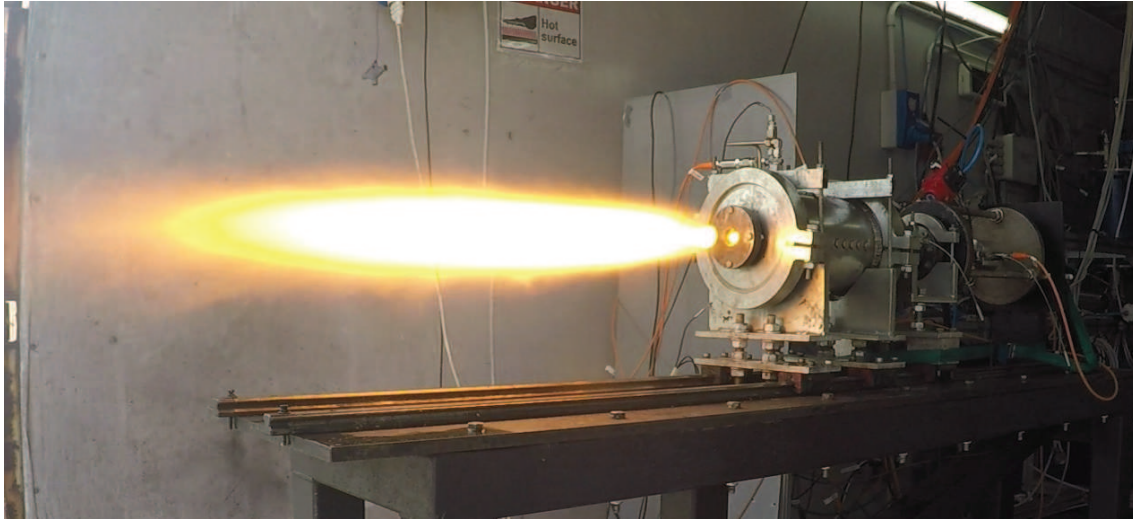
---

2 Room temperature vulcanizing

Figure 4.3: The rocket test bed during the first experimental campaign. The image was taken during the fourth test at a high oxidizer mass flow As it can be seen from the fuel rich flame part of the combustion take place outside of the combustion chamber. Plese note the railing system that allows to measure the in axis thrust.

The test bed were the motor lays has two linear guides so that the hybrid motor is mounted on slide units and is liable in the motor axial direction. With this test bed configuration the motor thrust can be transferred to a load cell installed on the main structure of the test bed enabling to measure the in-axis thrust. The complete experimental apparatus is visible during a fire test in figure 4.3. The motor, in front, is connected to the test bed by means of three sliding units, two for the combustion chamber one for the catalytic packing. Figure 4.3 shows the steady state flame of the 300 g/s

When the test start valve opens, the oxidizer pressurized in the tank flows through the fluidic line and the flow control valve, which is the major limiting element in the line, until it reaches the catalytic pack. Here the HTP mass flow is decomposed into gaseous O_2 and H_2O at about 1050 K. This hot and oxidizing gas mixture thermally decomposes and ignite the fuel grain. The catalytic pack is initially pre-heated in order to reduce the ignition time, particularly when the catalytic bed is near end of life. The ignition process normally takes around 1.2 s. Another possible way to ignite an HRM that employs hydrogen peroxide is the use of a catalytic hypergolic material or a catalytic fuel grain [43], [22].

During the whole duration of the test the VACV pintle stroke is constant and set in a predeterminate position.

There are several pressure sensors employed in the experimental setup. Both the pressurant and oxidizer side pressures of the tank are monitored, a pressure sensor, which is part of the FCV, is collocated upstream of the VACV. The pressure drop on the catalyst is monitored with a doublet of sensors one upstream and one downstream of the packing. The combustion chamber pressure is monitored in the post chamber,

downstream of the mixing plate. Some important locations of fluidic line and motor are temperature monitored as well using type J thermocouples. A thermocouple, placed at the tank outlet, measures the outflow temperature in order to compensate the density data and for safety reasons in case of dissociation inside the tank. Another thermocouple is placed upstream of the catalytic pack to monitor any variation of the temperature along the fluidic line. A thermocouple located directly downstream of the catalyst, monitors the decomposition efficiency. A set of two thermocouples is placed in the external part of the motor case to monitor if there is excessive heating of the motor case or flame break through. Valves $V05$ and V_{tank} are manually actuated before loading the tank and pressurization. Valves V_C and V_{test} are pneumatically and automatically actuated in this order during the test. Valve V_{purge} is pneumatically and remotely actuated, it allows low pressure nitrogen to flow through the last part of the line in order to purge this last volume of the line and the combustion chamber from any residual HTP. The downstream volume, between V_{test} and the engine injection is kept to a minimum. Valve V_{dump} is pneumatically and remotely actuated as well but its function is to empty and depressurize the line volume between V_C and V_{test}.

4.1.2 *Fire tests*

Before the static fire campaign started some preliminary test were performed on the catalyst bed. In fact it is possible to test the catalyst pack in a monopropellant configuration, in which a dedicated nozzle flange is applied directly downstream of the component, reducing the filling volume. This tests were aimed to evaluate the suitability and steady state performances of the catalyst pack currently employed for a wide range of operative oxidizer mass flows and chamber pressures. The nozzle applied to the monopropellant engine allowed to have nearly the same range of operative pressures with respect to the one predicted for the static fire tests at the same oxidizer mass flow. What was found from this tests is that for very low oxidizer mass flows, which unfortunately corresponds to low combustion chamber pressures, the catalyst pack had a very unstable behaviour. In particular, the pressure oscillations which intensity during a normal test is within the 14% of the nominal pressure, reached an intensity of 40% with a very low frequencies circa 7 Hz at 30 g/s. This was simply not acceptable for the purpose of throttling, which require thrust control and not the introduction of severe instabilities. At 60 g/s of oxidizer mass flow the catalytic pack had a radically different behaviour, stable with significantly reduced instabilities. This behaviour continued for the other oxidizer mass flows investigated up to 300 g/s. So the operative oxidizer mass flow range was set to 60 to 300 g/s with a reduction of the maximum achievable throttling ratio from 10:1 to 5:1. Now this limitation is attributed to the poor catalytic performance at very low pressures

(4 *bar*). There are several solutions to increase the range of throttleability of the motor configuration under analysis:

- Increase the pressure operative range in order to raise the minimum operative pressure is one possible solution. But this will imply also a raise in the maximum operative pressure, which will result in a heavier combustion chamber, and taking into account for the pressure drop chain of the feeding line and the MABP ratio this will result in a further massive system.

- The catalyst bed behaviour depends much on the reactivity and density of active sites. The low pressure stability would much benefit from a catalyst with a higher amount of active sites per volume. This solution could increase the throttling ratio maintaining the same low operative pressure range. In our group we have such catalyst bed, but unfortunately for the activities described in this work, it was available from the last semester of the third year.

- Another possible solution would be a variable throat nozzle. But few have investigated this technology which application is very limited.

After this monopropellant behaviour assessment campaign the preliminary fire test campaign started. A total of four static fire tests were carried out. This tests were aimed to evaluate the motor behaviour for a wide range of oxidizer mass flows in terms of regression rate and efficiency.
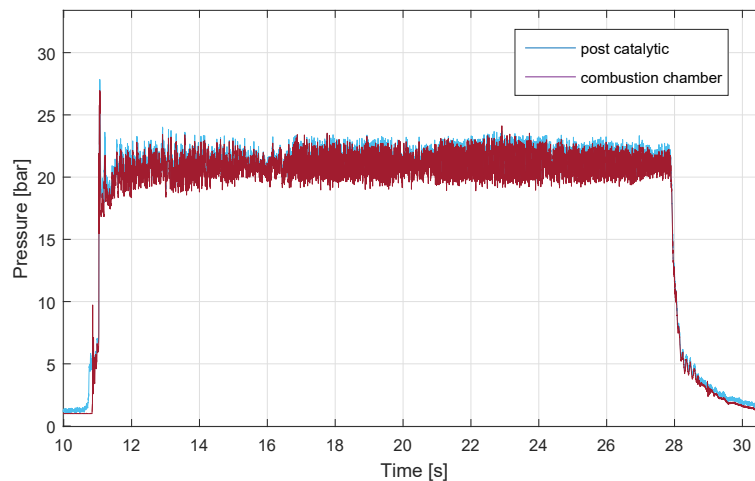

Figure 4.4: Pre and post combustion chamber pressure profiles during the second test at 138g/s.

In figure 4.4 are reported the pressure plot of post and pre combustion chamber during the second test. The flatness of the pressure profiles suggests that for paraffin-HTP propellant formulation the Marxman power law exponent is 0.5. The ratio between final and initial port diameter is nearly four.
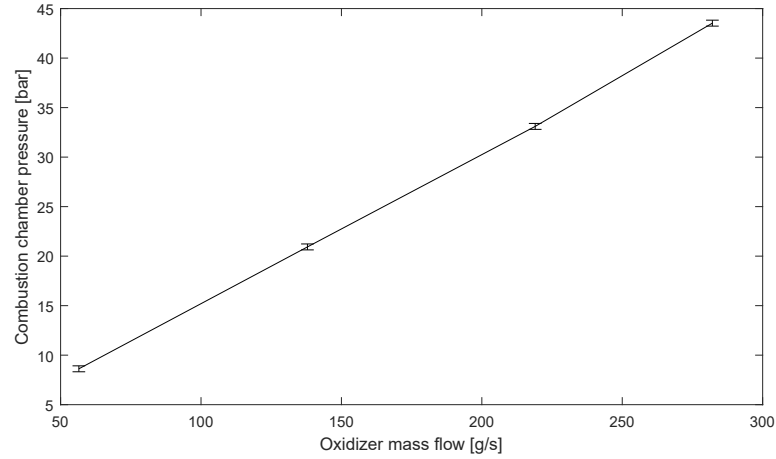
Figure 4.5: Average combustion chamber pressure versus oxidizer mass flow for the first preliminary fire test campaign.

Figure 4.5 represents the average motor combustion chamber pressure at different oxidizer mass flows. The trend is particularly linear, part of this linearity is due to the fact that by operating in the fuel rich region the increase of fuel mass flow compensate the decrease of characteristic velocity due to o/f shift. This is a very desirable characteristic in order to simplify the control algorithm and improve the predictability of the thrust at various levels. Here the combustion chamber pressure is assumed to be indicative of the achieved thrust, for one reason: during this test campaign little throat erosion was detected, mainly because of the extremely fuel rich environment. It is important to note that the obtained linearity far exceed the one that was expected.

Reference test	$\dot{m}_{ox}$ [g/s]	t_b [s]	$D_{p,fin}$ [mm]	p_{cc} [bar]	o/f
Test #1 | 60	57	25.0	80	8.62	2.9
Test #2 | 140	138	16.2	78.9	20.9	4.3
Test #3 | 220	219	7.6	68.3	33.1	4.2
Test #4 | 300	282	5.9	64	43.5	4.4

Table 4.1: Some results from the first preliminary fire test campaign.

Some relevant data from this preliminary fire test campaign are reported in table 4.1: oxidizer mass flow $\dot{m}_ox$, burning time t_b, final measured port diameter $D_{p_f in}$, mean combustion chamber pressure p_{cc} and and oxidizer to fuel ratio. This last is intended as the ratio between the used oxidizer mass flow and the fuel flow contributed exclusively by the fuel grain. The contribution of thermal insulation is not taken into account. Oxidizer mass flow and combustion chambers are variables that are acquired by our data logger, these are then averaged with the burning time. The final port diameter is measured directly on the fuel grain after the burn. The o/f is derived by dividing the oxidizer mass

consumed during the burning time (ignition excluded) by the burned fraction of the fuel grain. By looking at table 4.1 a curious thing can be noted: there is o/f shift between the first and second test with an oxidizer mass flow of 57 and 138 g/s respectively, but increasing the oxidizer mass flow to 219 and 282 g/s doesn't seem to affect the o/f with respect to the second test, or at least the o/f is not even close to the expected one by using a simple Marxman power law. An oxidizer to fuel ratio of 6.2 was wanted for a oxidizer mass flow of 300 g/s. This deviation from the attended behaviour was correlated to the consumption of the downstream face of the fuel grain. In fact in this motor design this face is not protected or inhibited by using a liner of thermal protection. During other fire test campaigns in which this fire test motor was involved, the oxidizer mass flow and fluxes involved were lower than the one during this test campaign (60 to 100 g/s), the relative downstream face regression rate was assumed as nearly constant. This is no longer the case for an engine in which the internal ballistic changes intensively. Furthermore we believe that the downstream exposed face regression was higher than usual because the mixing plate was closer to the fuel grain face. The reason for this lays on the fact that a longer fuel grain was employed and as a consequence the room for the post combustion chamber was reduced (since the combustion chamber available does not allow to vary the combustion chamber length). The proximity of the mixing plate also developed a flow recirculation between face and mixer, the higher the oxidizer mass flux the intenser is the recirculation. What was observed experimentally is that the downstream face was excessively consumed, for the high oxidizer mass flow tests.

Another think to note in table 4.1 are the test burning times. At the beginning these were set to achieve an equal final port diameter around 80 mm, but during the second test an excessive consumption of the mixing plate was observed. Because the failure of the mixing plate could have some catastrophic consequences, the burning time for the third and forth test were further reduced. This fact indicate that the fuel grain-mixer coupling affects both ends. However the mixer erosion rate can be reduced significantly with the appropriate mixing plate design.

During this fire test campaign the fuel grain-mixer correlation had some negative implications, the o/f was not the predicted one hence the performance were quite lower. But it must be kept in mind that, ironically, there was no o/f shift by doubling the thrust during the second, third and fourth tests. And the absence or reduction of oxidizer to fuel ratio shift for a throttleable hybrid rocket motor is a desireable characteristic. Furthermore a compact post combustion chamber design is paramount for a flight motor, and if a mixing plate is employed the downstream fuel grain face shall be protected in order to mitigate this effect. This strategy could be necessary for a constant thrust hybrid rocket were the face consumption could lead to undesired o/f shift.

Even if this motor configuration[3] presented the peculiar characteristic of reduced o/f shift because of the fuel grain-mixer interaction, it was not carried on for the dynamic throttling campaign for two reasons:

- It is true that the reduced o/f shift is desireable but it must be kept in mind that the achieved effect was unpredicted. In order to fully exploit this effect first it must be fully understood, and for this some proper CFD numerical simulation and experimental test campaigns must be performed. This task is demanding in terms of consumables required for the testing and man hours required both for testing and simulations.

- Because of the peculiar flow in the post combustion chamber an excessive amount of decomposed thermal protection was introduced in the flow, further reducing the maximum achievable characteristic velocity. In the worst case the paraffin fuel grain made up only the 70% of the total amount of consumed fuel (intended as the sum of the burned fuel grain and thermal protection).

4.2 SECOND PRELIMINARY MOTOR TEST CAMPAIGN

About the same time the first preliminary motor test campaign was carried out, this is the second semester of the second year of the Ph.D. course, some development test using a vortex engine were carried out at the Hybrid Propulsion Group of University of Padova. The so called vortex engine is distinguished by the fact that a vortex is established inside the hybrid combustion chamber. This motion is strongly rotational, and thanks to this there is a strong exchange of reactants and products between core and wall of the fuel grain port favouring the combustion chamber efficiency and increasing the fuel grain regression rate. Normally the vortex inside the combustion chamber is generated using a swirled gaseous injection. Our research group studied this configuration of hybrid combustion chambers for a long time [1],[2],[3], but recently it was reinvestigated to evaluate scaling effects. Another advantage of vortex motor is that since the mixing between reactants is favoured along the fuel grain, the size of the post combustion chamber can be very limited if compared to the one required for a mixing plate. This in turns results in a reduced amount of decomposed thermal protection that contribute to the combustion, hence higher combustion efficiency.

The preliminary fire test campaign objectives are:

- determine a zero order regression rate law to be used for the estimate of the fuel mass flow inside the combustion chamber during throttling fire tests;

---

3 The configuration under study during the first preliminary campaign had an axial gaseous injection, a paraffin fuel grain and a mixer in the post combustion chamber.

- measure the static thrust level and hence determine the achieved characteristic velocity and efficiency reached with the various oxidizer mass flows;

- verify the robustness of the whole system which had to perform for a wider range of oxidizer mass flow than the one normally used during previous characterizations.

Once again a series of four constant oxidizer mass flow tests was performed.

4.2.1   *Motor design & test setup*

The combustion chamber case is made of carbon steel and it is composed of a cylinder and two flanges (oxidizer inlet and exhaust outlet). With respect to the previous configuration represented in figure 4.1, this time the cylindrical section is not flanged, because clamps are no longer needed to connect the flanges with the case. The two flanges are connected by a set of eight rods, which also holds them in position against the cylinder. The sealing between flanges and cylinder is granted by a graphite packing. The case was designed to withstand a MEOP of $40bar$ with a safety factor of 4, the assembly was pressure tested using nitrogen at $80bar$ with success.
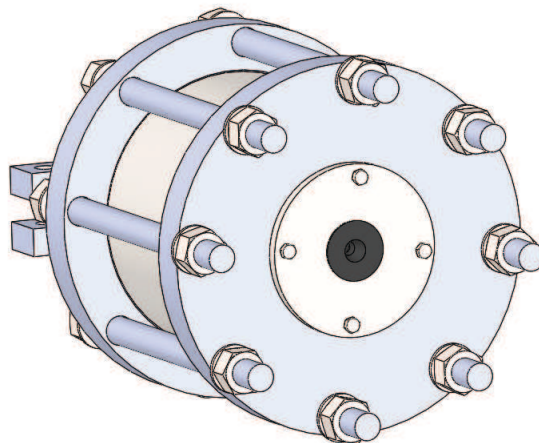

Figure 4.6: A CAD model of the motor case used during second preliminary and throttling fire test campaigns.

The cylinder is very simple if compared to the previous motor configuration. This imply that different cylinder of various lengths can be manufactured without resulting in a to excessive expense. This means that the combustion chamber length constrain of the previous configuration no longer applies.

The inlet flange is directly connected with the catalytic bed and hosts the swirled injector. The outlet flange accommodates the nozzle, which is hold in place by a smaller flange connected to the main one by a set of four bursting bolts. The bursting bolts are designed to crack at a combustion chamber pressure of $60bar$. The nozzle is machined

from a bulk graphite cylinder, it has a throat diameter of 13mm and an exit diameter of 23.5mm. This implies an expansion ratio of 3.26 which is close to the optimal value, considering that the engine operating pressure ranges from 8 to 37bar.

Inside the motor case a cartridge like combustion chamber is used analogously to what has been described in section 4.1. A fuel grain made of high density polyethylene (HDPE) with an initial port diameter of 20mm and length of 100mm is used. These consumable parts are assembled in a cartridge like fashion that can be easily inserted in and extracted from the motor case.

The cartridge is composed by a cylindrical backup shell that protects the motor case if the fuel grain is totally consumed or if the sealing between the internal components fail. This cylindrical backup shell is made of HDPE and is filled and sealed with the consumables. Starting from upstream to downstream we have: inlet flange thermal protection, HDPE fuel grain, downstream flange protection and in the end the nozzle. All the thermal protections are made of cotton-phenolic, which erosion rate is fairly low for this application[4]. The fuel grain touches the inlet flange thermal protection meaning that during this motor configuration has no prechamber. On the other side the fuel grain is directly connected with the downstream flange thermal protection. This component is thicker then the upstream one and constitutes also the post combustion chamber. The consumables composing the combustion chamber are joined together using RTV silicones to prevent leakages between them. Part of the internal ballistic for this engine has been developed by the Hybrid Rocket Group at University of Padova under commission from a external investor, to many details on the internal ballistic of the engine can not be disclosed.

One particular feature of this hybrid combustion chamber is the swirled injector. The one used during these experiments is an inward type manufactured by tangentially drilling a cup-like shell. Figure 4.7 shows the cad model and the 3D printed swirled injector. A common characteristic used to describe the type of injector is the geometrical swirl number, for this injector the geometrical swirl number (SN_g) is 3.3. This parameter was computed using the formula:

$$SN_g = (r_{int} - r_{holes}) \frac{r_{int}}{n_{holes}\ r_{holes}^2}$$

Where r_{int} is the internal radius of the cup-like injector, r_{holes} is the radius of the drilled holes and n_{holes} is the number of drilled holes. It must be kept well in mind that this value is not the effective swirl number inside the combustion chamber, nor the swirl number at the injection plate. Normally the internal swirl number is lower than the geometrical one and it also decay along the motor length because of dissipations and axial fuel injection. It is however true that a higher geometrical swirl number implies a higher initial swirl number and hence it can be used as an easy-to-measure reference parameter.

---

4 The thermal protections contribution to the overall fuel mass flow hardly exceed the 15%.

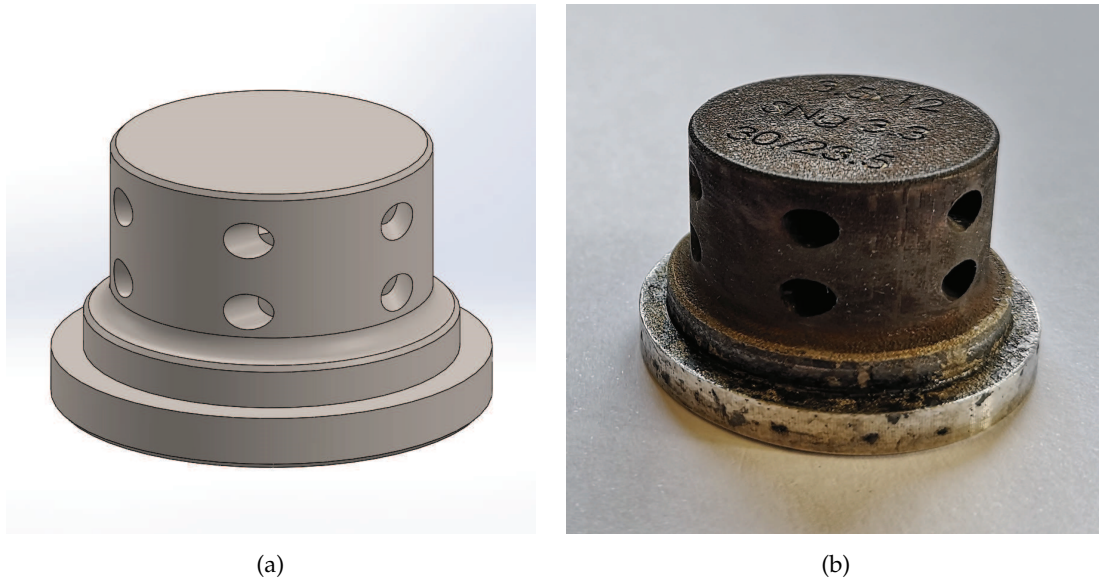(a)   (b)

Figure 4.7: The tangentially drilled cup-like design of the swirled injector. On the left the CAD[5] model, on the right the 3D printed manufactured component, after the test campaign.
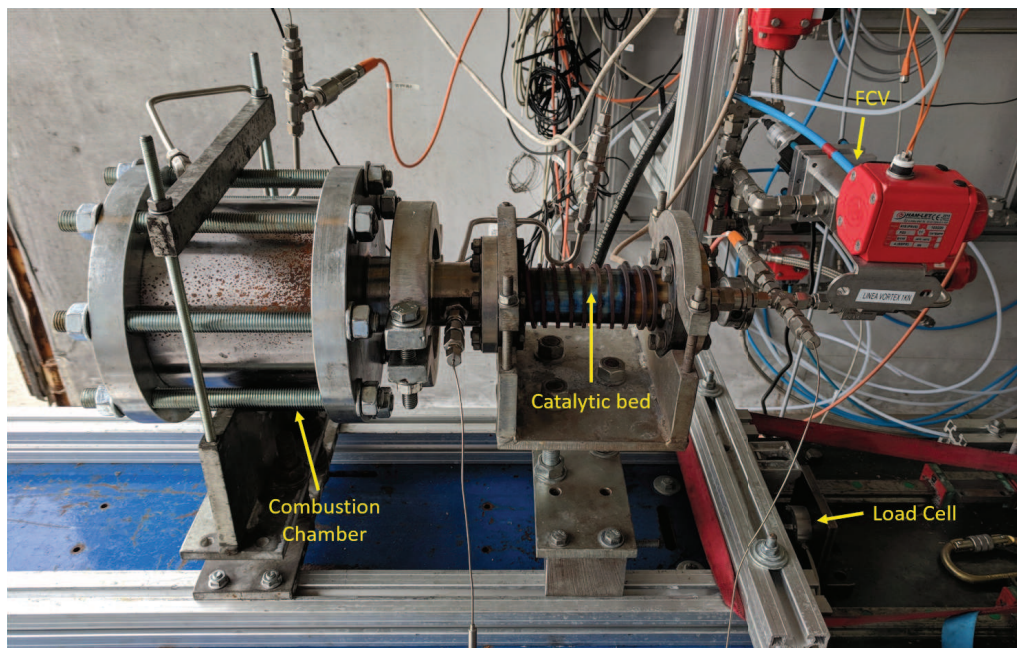

Figure 4.8: Small scale hybrid rocket motor under development at the University of Padova and the used eperimental test bed. Note that the motor is now connected to a carbon steel board (blue) that slides on the axial direction thanks to the railing system. Plese note also the other components that make the experimental test bed and rocket motor.

For what concern the experimental set up, the fluidic line remains unchanged from the one described in section 4.1. Also during this test campaign the catalytic pack was pre-heated. The pressure drop on the catalyst is monitored with a doublet of sensors one upstream and one downstream of the packing. The combustion chamber pressure is monitored in the post chamber. A thermocouple is placed upstream of the catalytic pack

to monitor any variation of the temperature along the fluidic line. Another thermocouple located directly downstream of the catalyst, monitors the decomposition efficiency. A set of two thermocouples is placed in the external part of the motor case to monitor if there is excessive heating of the motor case and flame break through. The hybrid motor is collocated on a thick board made of carbon steel that is allowed to move along the motor axis with respect of the test bed thanks to the same railing system used in the previous preliminary campaign. The board is connected to a load cell which is used to measure the in axis thrust of the rocket engine.

The valve opening procedure is the same described in the previous section.

4.2.2   *Fire tests*

In order to demonstrate the feasibility of throttleability in a HRM configuration such as the one described and to evaluate the motor performances, a series of four preliminary fire test were carried out. These tests had an increasing oxidizer mass flow: 71, 147, 218 and 296g/s. The length of each test was selected in order to obtain a similar final port diameter between tests, this was possible thanks to previous knowledge of the regression rate power law.

Reference test	$\dot{m}_{ox}$ [g/s]	t_b [s]	$D_{p,fin}$ [mm]	p_{cc} [bar]	T [N]	c^* [m/s]	η [%]*
Test #1 | 60	71	12.4	46	9.86	153.3	1509	95.2
Test #2 | 140	147	10.3	50	19.96	347.0	1507	95.5
Test #3 | 220	218	8.4	55	30.90	536.3	1510	95.4
Test #4 | 300	296	6.5	54	36.44	722.3	1493	94.8

* The efficiency here reported includes both the contributions of characteristic velocity and thrust coefficient efficiencies.

Table 4.2: Some results from the second preliminary fire test campaign.

Table 4.2 reports the results of the static fire campaign. During this tests an overall throttling ratio of 4.7 was reached with a thrust ranging from 153 to 722N. The overall efficiency value is steady over the range of flows analysed. The reduction of characteristic velocity with the flow is extremely low. This is due to the particular behaviour of the swirl injector coupled with the combustion chamber that allows us to get a high Marxman power law exponent. Thrust is directly measured with a load cell, the sensor acquisition uncertainty is 2.9 N. The load cell has been calibrated prior the test campaign. The characteristic velocity has been computed with the Kline-McClintock formula from the thrust and propellant flow: it ranges from 22 to 50 m/s depending on the test.
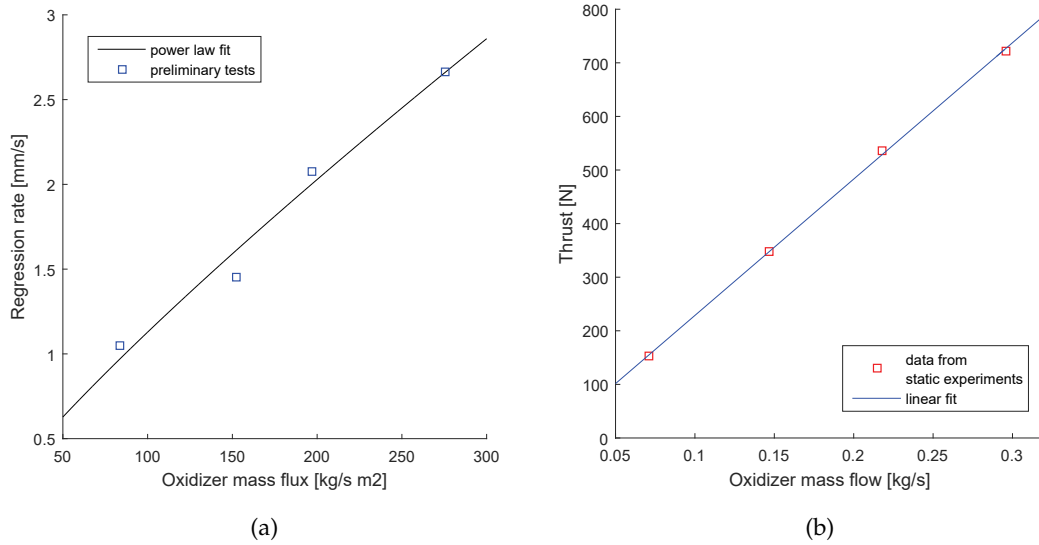
Figure 4.9: Results of the second preliminary test campaign. On the left, regression rates with the oxidizer mass fluxes. The data were fitted using a power law. On the right the thrust level versus the input oxidizer mass flow.

Figure 4.9a shows the regression rates obtained during the static fire test campaign as well as a power law fit which is represented by Equation 4.1. The coefficient of determination R^2 for this fitting function is equal to 0.97. The oxidizer flux has been computed using the average port diameter over the burn. This is the traditional method even if new methods were introduced to compute the experimental oxidizer flux, such the one presented in [7].

$$\dot{r} = 3.384 \cdot 10^{-2} \cdot G_{ox}^{0.78} \tag{4.1}$$

Figure 4.9b presents the thrust during the four tests, the trend is quite linear as can be seen from the fit. This is possible thanks to the low o/f shift due to the high power law exponent obtained with this configuration. As can be noted from Table 4.2 the behaviour of the combustion chamber pressure is not as linear as the thrust, this is mainly due to the effect of nozzle throat erosion. During the preliminary fire test campaign no system failures or thermal problems were detected. For each static test the spectrogram of the combustion chamber pressure was analyzed. No peak of intensity was detected from the signal in the frequency range determined during the cavitation instabilities characterization. This indicated that the cavitation in the venturi do not have a detectable effect on the combustion chamber instabilities.

4.3 DYNAMIC THROTTLING FIRE TESTS

With the throttling fire test campaign we want to demonstrate the throttling feasibility for our hybrid rocket motor configuration. This is an engine that uses hydrogen peroxide as an oxidizer, which is decomposed in a catalytic bed prior to the injection inside the combustion chamber. This configuration does not require a variable area injection to compensate the atomization defect with a non nominal oxidizer mass flow. A swirled injector has been adopted, which is possible because of the gaseous injection. Another objective of the throttling campaign is to understand the behaviour of the coupled FCV and HRM, and in order to do this, some points of the system transfer function were determined.

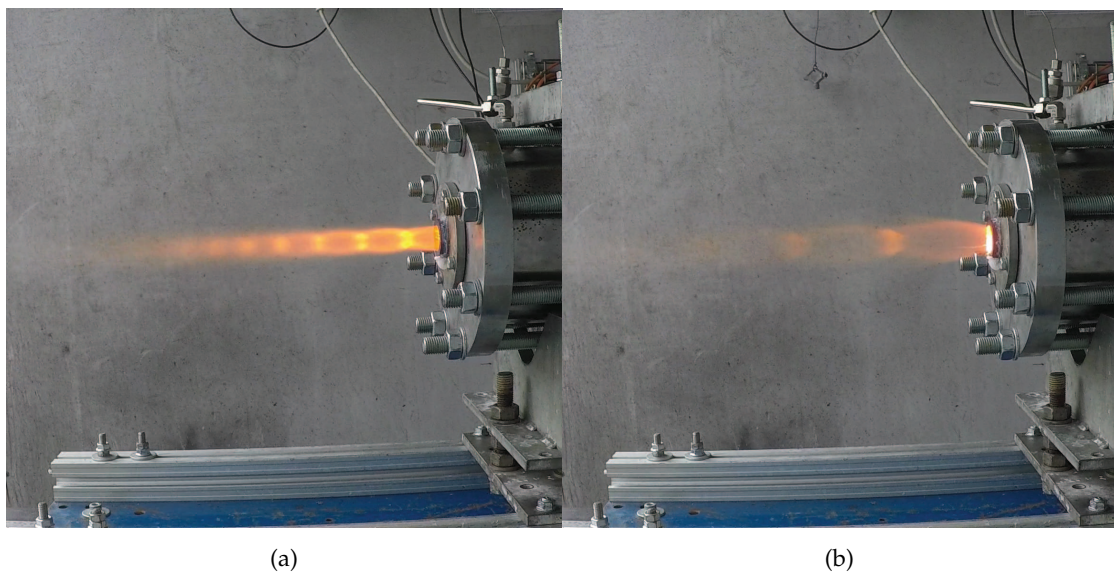(a)   (b)

Figure 4.10: Comparison between plumes from different operative regimes: On the left, the fuel rich overexpanded flame at low thrust. On the right, the oxidizer rich underexpanded flame at high thrust.

The campaign was carried out with four tests. Analogously to what happened during the dynamic FCV characterization, three fire tests had a sinusoidal thrust command, while the last one was commanded with an impulse. The overall burning time for each test is around thirteen seconds, the first three are needed for the system ignition, while the remaining ten are left for the throttling test. For all the tests the engine is ignited at $100 g/s$.

In figures 4.11, 4.12, 4.13 and 4.14 are reported the measured pressure and thrust plots for the four tests. The left hand side of each series represents the pressure profile during the tests, note that during the first test ($0.2 Hz$ figure 4.11a) are evident signs that indicate the MABP was reached for high combustion chamber pressures. Another interesting thing to note on the combustion chamber pressures is the effect of nozzle throat erosion:
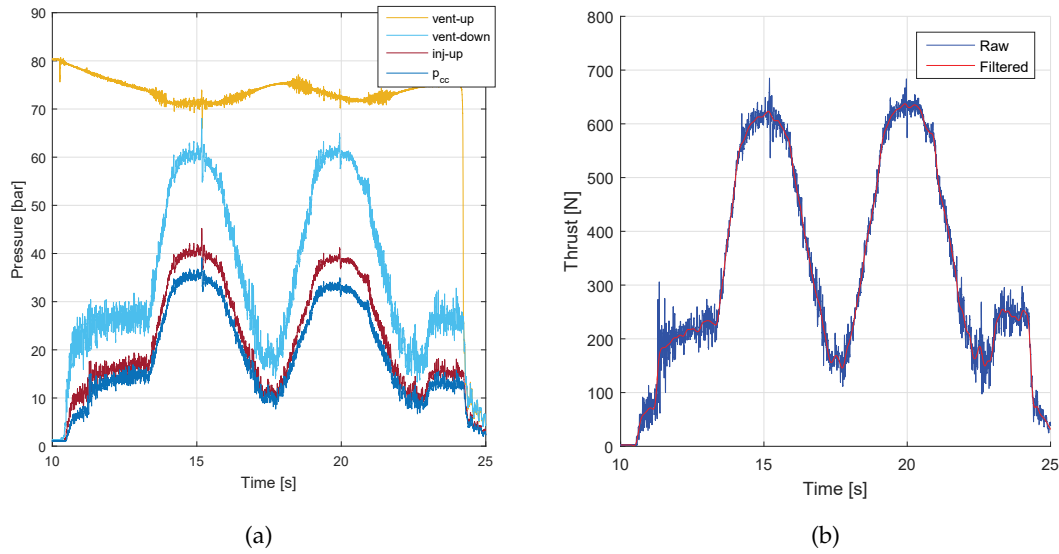
(a)

(b)

Figure 4.11: Pressure and thrust profiles for the first throttling test: two sine waves at 0.2 Hz.
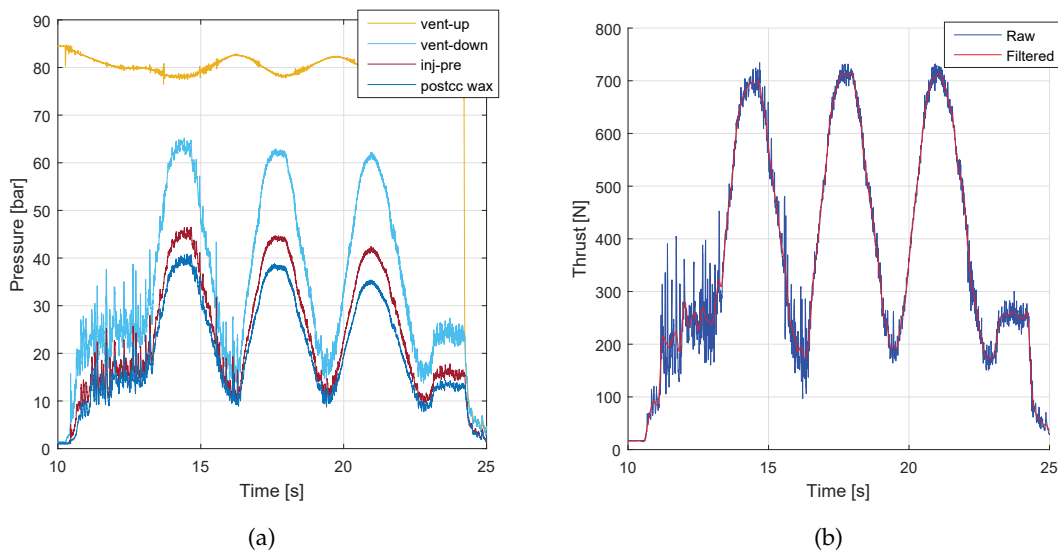

(a)

(b)

Figure 4.12: Pressure and thrust profiles for the second throttling test: three sine waves at 0.3 Hz.

the peak pressure tend to diminish with the burning time. This is particularly evident in figures 4.12a 4.13a. The right hand side of each series represents the measured thrust profiles for the tests. The blue line represents the unfiltered data, while the data associated with the red line are filtered using a Butterworth digital filter with a $5Hz$ cut frequency. You can notice that the thrust becomes noisier when it is lower. We believe that this is due to the fact that the catalytic bed performs poorly when the pressure is lower.

Figure4.14 shows the pressure and thrust profiles for the rectangular impulse test. Since to ignite the engine a $100g/s$ is required the rectangular impulse starts at a slightly higher level than the minimum, which is achieved at $70g/s$.
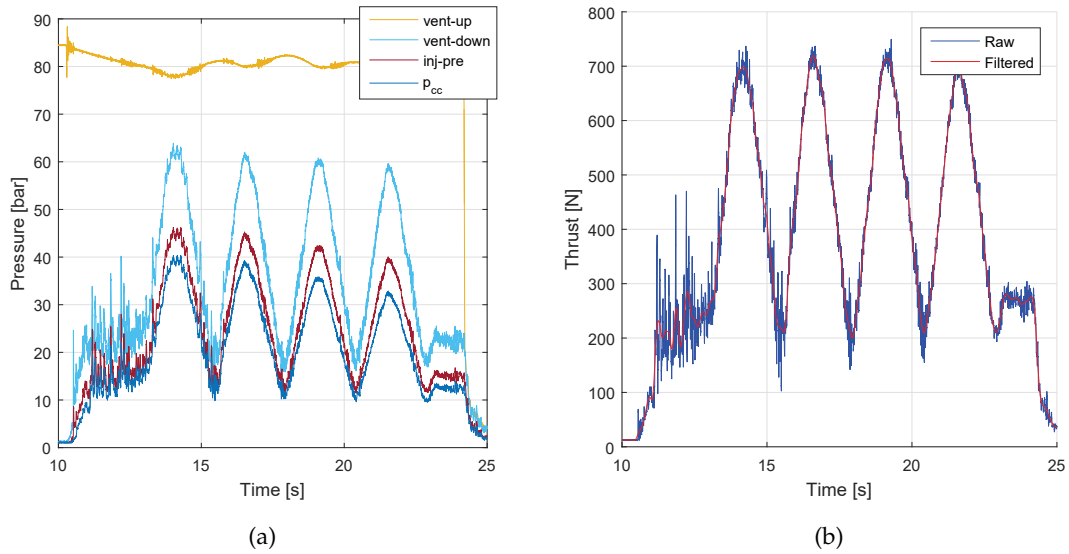
(a)

(b)

Figure 4.13: Pressure and thrust profiles for the third throttling test: four sine waves at 0.4 *Hz*.
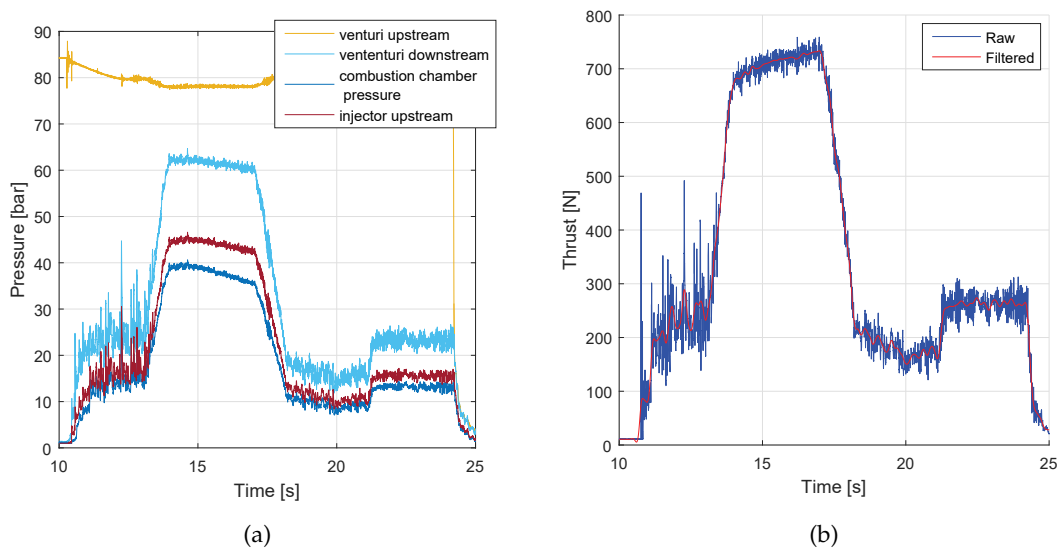

(a)

(b)

Figure 4.14: Pressure and thrust profiles for the fourth throttling test: rectangular impulse.

The measured thrust data were compared to the command thrust profile given to the FCV and the thrust profile that was expected from the measured oxidizer mass flow combined with the power law determined in the preliminary test (equation 4.1). This last profile was determined by considering that the oxidizer mass flow is instantaneously decomposed and the response of the fuel grain is immediate with the change of regime. This mean the system has an order zero with no delays. The comparison is presented in Figure 4.15.

It must be noted that during these tests there was not a feedback loop on the thrust, but only on the pintle stroke. The commanded thrust was actually converted in a preloaded

pintle stroke sequence to be performed during the fire test. Because the oxidizer mass flow is dependent on the upstream pressure and because the force coefficient depends on throat erosion there is a slight shift of the command thrust profile from the desired one.

At this point, the tested fuel grains were measured to validate the simplified regression rate model used. The measured final port diameter was compared with the one predicted with the zero order model. Table 4.3 reports the measured and computed final port diameter as well as the achieved thrust and throttling ratio for the throttling tests. The results of this comparison are reported in Table 4.3.

Reference test	$D_{p,in}$	$D_{p,fin,m}$ *	$D_{p,fin,c}$ †	T_{min}	T_{max}	TR ‡
Test 025, 0.2Hz	$20mm$	$55.6mm$	$57.9mm$	$149N$	$634N$	4.26
Test 033, 0.3Hz	$20mm$	$58.1mm$	$59.9mm$	$171N$	$712N$	4.16
Test 034, 0.4Hz	$20mm$	$57.7mm$	$59.8mm$	$202N$	$719N$	3.56

* Measured final port diameter.

† Final port diameter computed by integrating the zero order model.

‡ Throttling ratio as the ratio between the maximum and minimum achieved thrust.

Table 4.3: Results of the static fire test campaign

It should be noted that the diameter computed from the zero order model is bigger than the measured one. This could be due to an approximation of the computed regression rate power law during the static fire test campaign, but it is equally probable that the dynamic response of the engine plays an important part on the regression rate. In table 4.3 are reported also the minimum and maximum thrusts reached during the sinusoidal command fire tests as well as the throttling ratios. The throttling ratio for the 0.4 Hz test is quite lower than the others, as it will be shown soon this is due the incorrect response of the system to high frequency commands. A throttling ratio of 4.2 was reached during these tests.

The measured thrust profile as well as the oxidizer mass flows, used in the computation of the instantaneous system response, are filtered using a Butterworth digital filter with a cut frequency of 5Hz. Along with the command thrust profile they are presented in figure 4.15. As you can see from figure 4.15a the exceeding of the MABP is confirmed for the first test commanded with a sinewave of 0.2Hz frequency: the maximum thrust is not reached because of a lack of oxidizer mass flow to the combustion chamber[6]. For the remaining tests the upstream pressurization has been raised of 10bar and hence this problem was no longer encountered. Let us consider the thrust profiles of the other two sinusoidal

6 The green line represents the thrust that it is expected from the measured oxidizer mass flow and zero order response of the combustion chamber.
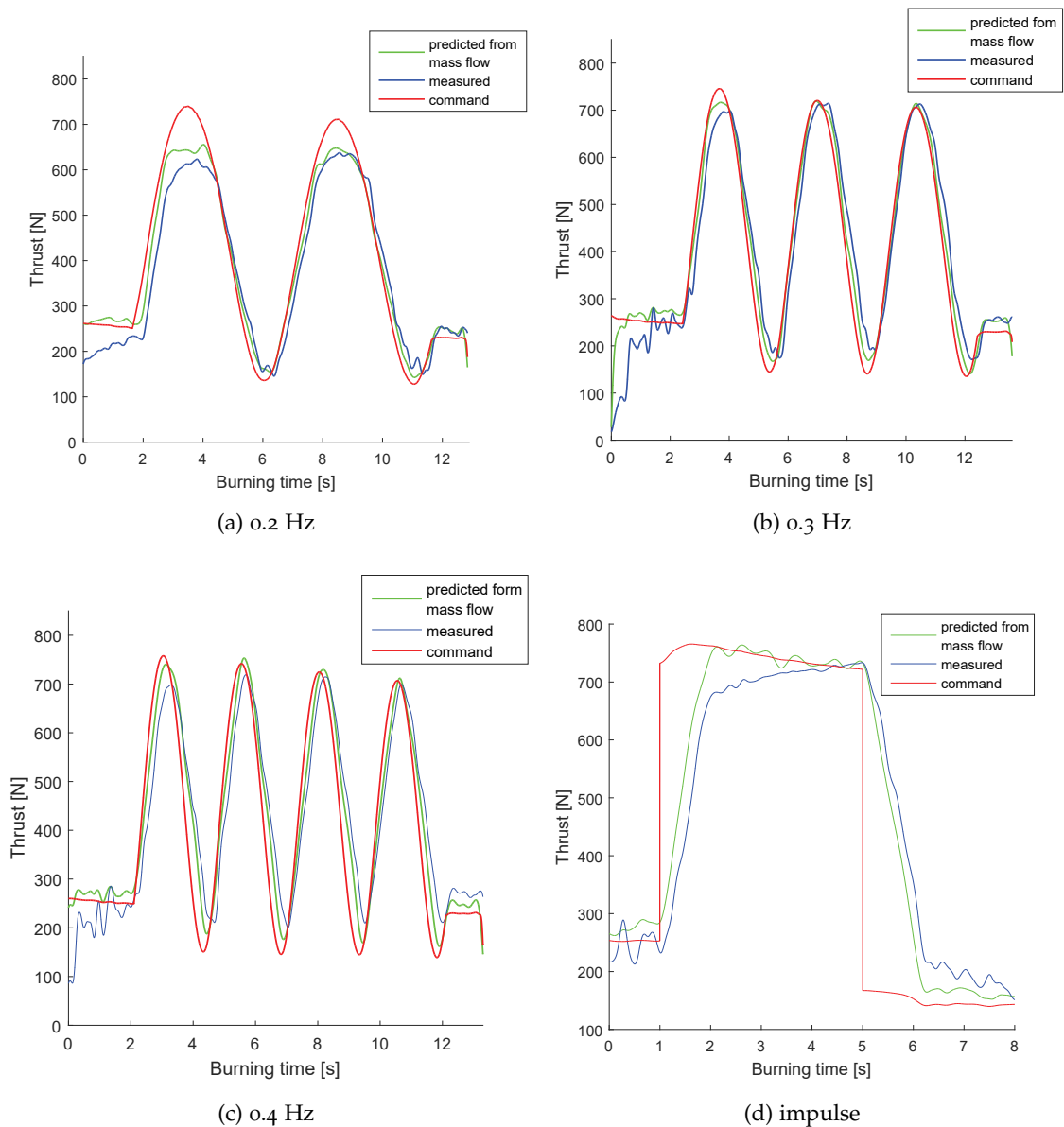
(a) 0.2 Hz

(b) 0.3 Hz

(c) 0.4 Hz

(d) impulse

Figure 4.15: Comparison between measured, command and predicted thrust profile for the four throttling tests. Data are filtered at 5 Hz

command tests. For the $0.3Hz$ test it is possible to note that the computed thrust profile follows the command one quite well. There is a little discrepancy between the measured and zero order model thrust profiles, which is particularly evident when throttling down. The thrust profiles for the $0.4Hz$ test present quite a peculiar behaviour, the zero order model profile is delayed from the command one and its amplitude is attenuated as well. The measured thrust profile follows an analogous trend with respect to the zero order one. In all cases the major discrepancies can be observed during throttling down.

The last comparison shows the response of the system to a rectangular impulse with a length of $4s$. As you can see the response of the zero order model to the command is analogous to the one presented during the FCV dynamic characterization, with similar

rise and fall times: 1.09 and 1.24s respectively. In this case the rise time is lower because of a lower initial oxidizer mass flow compared to the final one. But it is important to note that the combustion chamber takes some time to reach the command both during rise and fall. This is supposed to be caused by a non perfect catalytic bed response coupled with the presence of the swirl injector[7].
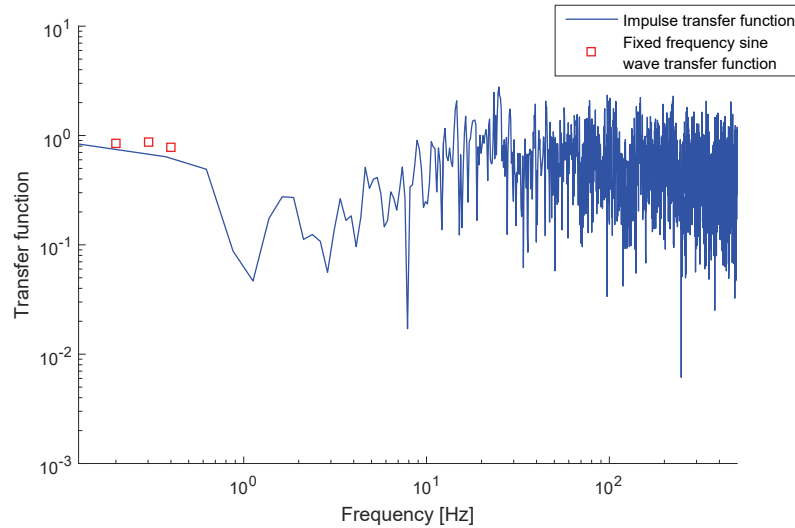

Figure 4.16: Transfer function for the performed throttling tests. In red the data obtained for the sinusoidal command tests.

Analogously to what happened during the FCV dynamic characterization, the transfer function between command and measured thrusts was determined. In this case the output for the transfer function is the measured thrust while the input is the command thrust which is actually computed from the imposed pintle stroke. As expected the transfer function for the higher frequency test (0.4Hz) is lower than the other two. In this case the transfer function computed for the 0.2Hz sinusoidal test is incorrect because the MABP was reached and hence the obtained thrust was considerably lower that the required one. The numerical values of the transfer function for the sinusoidal command tests are reported in Table 4.4.

Transfer function at 0.2Hz	0.849
Transfer function at 0.3Hz	0.876
Transfer function at 0.4Hz	0.779

Table 4.4: Coupled FCV-HRM transfer function data from the three sinewave command tests.

In Figure 4.16 is reported the transfer function obtained for the test with the impulse command. It must be noted that since the impulse has a finite length the transfer function

---

7 A partially decomposed HTP flow is not swirled efficiently by the swirled injector and as a consequence the whole system is affected by the catalytic response.

loses resolution for the higher frequencies. In the figure are presented also the results of the transfer function obtained with the sinusoidal tests. The value for the $0.2Hz$ test is incorrect because the MABP was passed, however it is included in the plot. It can be noted that the trend of the impulse transfer function follows the one obtained with the sinusoidal test. Over $1Hz$ the measured thrust noise overcome the impulse command.

Even if the data presented in Figure 4.16 are limited, the obtained transfer function can be used to understand the behaviour of the coupled FCV-HRM system, which starts to be attenuated at a frequency of $0.4Hz$. At this frequencies the response of the system is strongly limited by the FCV. However further attenuation and delay is observed for the hybrid rocket motor response.

4.4 CHAPTER CONCLUSIONS

After the FCV was implemented, dynamic throttling fire tests were carried out successfully. A maximum throttling ratio of 4.2 was achieved with thrusts up to $720N$. The motor used in this throttling tests was composed of a catalytic bed, for the hydrogen peroxide decomposition to high temperature gas, a swirled injector, that impose an in axis rotational motion to the oxidizer flow, and a combustion chamber, which embeds a high density polyethylene fuel grain. The combustion chamber design is very compact. We believe that this configuration is particularly suited for throttleability, because it does not require a variable area injector, which would be necessary with a liquid oxidizer injection. A transfer function of the FCV-HRM coupled system was determined and it appears that the response of the system starts to attenuate at $0.4Hz$. This limitation is due both to the motor reaction with a variable oxidizer mass flow and the FCV dynamic behaviour. The experimental results presented in this chapter proved the feasibility of throttling for hybrid rocket motors. Furthermore throttleability was implemented in a practical HRM configuration that uses flightworthy oxidizers and fuels, and with some small modifications could be transformed in a ready to flight configuration.

CONCLUSION

Throttleability is an important feature for present and future hybrid rocket motor applications. This thesis has been focused on the development of a 1 kN class throttleable hybrid rocket motor. This motor employed high test peroxide as oxidizer which is pressure fed to the combustion chamber and is decomposed by means of a catalyst pack. This configuration proved to be suitable for throttling purposes, since it does not require a variable area injector nor to have excessive injection pressure losses. Furthermore the propellant formulation used is among the green ones.

A steady state combustion model has been presented and the implication related to throttling were discussed. Because of the diffusion flame mechanism and the dependence between oxidizer and fuel mass flow an oxidizer to fuel ratio shift may occur. This in turns affects the combustion chamber characteristic velocity, because of a variation from the maximum one. This leads to some penalties in terms of performance that are not usually present for the other two chemical propulsive technologies. The entity of the losses in performance is dependent on throttling requirements, motor configuration, expected thrust profile and propellant formulation. Correctly evaluate the characteristic velocity penalties is case dependant, however some quantitative informations are presented in two particular cases with for two different throttling ratios 5:1 and 10:1 for three propellant formulations. In most cases, the losses determined during this analysis are lower than 9%. Variations of the motor configurations and phenomena strongly dependent on internal fluid dynamic were not taken into account.

Because part of this work consists in implementing throttleability in hybrid rocket motors and performing dynamic throttling fire tests, a flow control valve has been developed and characterized. The flow control valve design is based on the variable area cavitating venturi, in which the throat area of a conventional venturi tube is altered by means of a conical pintle. The conical shaped pintle has been chosen for sake of simplicity, manufacturing and control. On the other hand the use of a cavitating venturi implies that when the flow is choked there is independence between the oxidizer flow and downstream pressure; so that the tank and combustion chamber environments are uncoupled and the flow can be controlled in a reliable and precise way. In fact once the variable area cavitating venturi is characterized it can be used for flow measurements.

The pintle stroke has been controlled thanks to the actuation which is based on a drivescrew, a stepper motor and an absolute angular encoder for the feedback on the pintle position. The flow control valve control loop is closed on the pintle stroke but open on the thrust or on the oxidizer mass flow. It is possible to close the control loop on these

two variables and obtain the most precise control. However this would be easy to do in an already equipped set-up, but maybe could not be possible on the flight system, hence the most robust design solution has been used: open loop and precise flow control.

The characterization consisted in four different phases. During the first phase the characteristic curve has been obtained. This is the most important information about the flow control valve, it is not possible to perform a control loop which is open on the mass flow or thrust without precisely knowing the flow control valve characteristic. The characteristic curve is almost quadratic with the pintle stroke and the trend obtained for the discharge coefficient had values higher than 0.92. On the second phase the maximum back pressure that can be applied to the flow control valve without un-chocking the flow has been determined. The trend showed a good correlation with the pintle stroke. For high pintle strokes the obtained values are similar to the one reported by other researchers (0.85), but the maximum allowed back pressure ratio decreases strongly for lower pintle strokes reaching 0.42. This implies a higher required upstream operating pressure for lower pintle strokes, however this is not a problem for throttling purposes, because for lower oxidizer mass flows and hence pintle strokes, the combustion chamber pressures decreases as well. The effects that the cavitation could have on the engine behavior rouse some concerns among some of my colleagues as well as some engineers and researchers I met attending at conferences. This was an aspect worth investigating and it is the aim of the third phase of the flow control valve characterization, which outcome is a trend of the cavitation peak frequencies downstream of the venturi. The most important variable for the cavitation instability frequency is the local pressure. A trend between the two has been determined and evidence of instabilities in the combustion chamber pressure at the same frequency was investigated. No relevant instabilities at the cavitation frequency were found inside the combustion chamber. The last phase for the flow control valve characterization consisted in determining some dynamic characteristics: the mass flow transfer function at 0.2, 0.3 and 0.4 Hz as well as the rise and fall time for a throttling ratio of 1:5 have been determined. The answer of the flow control valve at frequencies higher of 0.5 Hz are limited because of the actuation system. The rise and fall time from an oxidizer mass flow of 60 g/s and 300 g/s are 1.2 and 1.3 second respectively.

Finally the flow control valve has been integrated with the engine and the fire test campaign could start. Before the dynamic throttling tests could be performed two preliminary fire test campaigns were carried out. For the first the combustion chamber configuration had an axial gaseous injection and a paraffin fuel grain (a configuration with a power law exponent near 0.5). A mixing plate was added in the post combustion chamber to enhance the combustion between reactants. The results of this preliminary campaign found a less severe o/f shift then expected and generally lower o/f. This effect has been attributed to a correlation between mixer and fuel grain downstream face at different oxidizer mass flow.

A vortex engine configuration was used during the second preliminary fire test campaign instead. This consisted in a swirled gaseous injection and a HDPE fuel grain. Because the vorticity inside the fuel port enhance the mixing of the reactants, the post combustion chamber design is more compact with respect of the previous configuration, resulting in a reduced amount of thermal protection pyrolysis gasses in the propellant. During this preliminary test campaign the vortex motor configuration proved efficient with an $I_s p$ efficiency around 95% for the wide range of oxidizer mass flows investigated. Also a good linearity of the thrust with the oxidizer flow has been observed and the o/f shift was as expected. For these reasons the vortex motor configuration has been used during the dynamic throttling campaign.

The dynamic throttling fire test campaign consisted in four fire tests: three with a sine-wave thrust command at 0.2, 0.3 and 0.4 Hz and the last one with a 4 s rectangular impulse. With the three sine-wave tests it was possible to determine the transfer function for the coupled FCV-HRM system. The three thrust trends were also compared with the expected system response from a zero-order model. The response to the impulse command was not as the expected one and it was not possible to obtain rise and fall time for the whole system. During this dynamic throttling tests a maximum thrust of 720 N and a throttling ratio of 4.2:1 has been achieved. The 720 N thrust is the equivalent of 1 kN in vacuum. The throttling ratio obtained was slightly lower than the 5:1 expected.

The throttling feature has been successfully integrated in a high efficiency hybrid rocket motor configuration, which used hydrogen peroxide as oxidizer and HDPE as fuel, the oxidizer is decomposed thanks to a catalyst pack. Other than being a green propellant formulation this configuration is particularly suited for throttling and reignition purposes. The developed flow control valve made this throttling implementation possible.

For the future it could be possible to reduce consistently the weight of the valve body, maybe by using additive manufacturing techniques, in order to make it flight-weight. Also the actuation could be rearranged, one particular promising solution could be the use of an hydraulic cylinder like actuation in which the operative fluid is the oxidizer itself. Now that a flow control valve has been developed for our 1 kN class motor the same could be done for the 7 kN class test motor to study also how scaling effects affect throttling.

[1]   Bellomo N., Barato F., Faenza M., Lazzarin M., Bettella A. and Pavarin D. "Numerical and Experimental Investigation of Unidirectional Vortex Injection in Hybrid Rocket Engines." In: *Journal of Propulsion and Power* 29.5 (2013), pp. 1097–1113.

[2]   Bellomo N., Barato F., Faenza M., Lazzarin M., Bettella A. and Pavarin D. "Numerical and Experimental Investigation on Vortex Injection in Hybrid Rocket Motors." In: *47th AIAA/ASME/SAE/ASEE Joint Propulsion Conference & Exhibit*. San Diego, CA, USA, July-August 2011.

[3]   Bellomo N., Faenza M., Barato F., Bettella A. and Pavarin D. "The "Vortex Reloaded" project: experimental investigation on fully tangential vortex injection in N2O – paraffin hybrid motors." In: *48th AIAA/ASME/SAE/ASEE Joint Propulsion Conference & Exhibit*. Atlanta, GA, USA, July-August 2012.

[4]   Boardman T. A. "Hybrid Propellant Rockets," in: *Rocket Propulsion Elements*. Ed. by Sutton G. P. and Biblarz O. Jhon Wiley & Sons Inc., 2001.

[5]   Jones R. A. *Hybrid Propulsion System for an Advanced Rocket-Powered Target Missile, Quarterly Technical Report*. Tech. rep. UTC 2220-QTR2, 1967.

[6]   Karabeyoglu M. A. and Altman D. "Dynamic Modeling of Hybrid Rocket Combustion." In: *Journal of Propulsion and Power* 15.4 (1999).

[7]   Rabinovitch J., T. Jens E., Karp A., Nakazono B., Conte A. and Vaughan D. A. "Characterization of PolyMethylMethAcrylate as a Fuel for Hybrid Rocket Motors." In: *2018 Joint Propulsion Conference*. Cincinnati, OH, USA, July 2018.

[8]   Karp A., Nakazono B. A., Vaughan D., Story G. T., Oglesby B. and Prince A. "Update on Technology Development Plan for a Low Temperature Hybrid Mars Ascent Vehicle Concept." In: *2018 Joint Propulsion Conference*. Cincinnati, OH, USA, July 2018.

[9]   Christopher E. Brennen. *Cavitation and Bubble Dynamics.* New York: Oxford University Press, 1995.

[10] Arves J., Gnau M.,Joiner K., Kearney D., McNeal C. and Murbach M. "Overview of The Hybrid Sounding Rocket (HYSR) Project." In: *39th AIAA/ASME/SAE/ASEE Joint Propulsion Conference and Exhibit*. Huntsville, AL, USA, 2003.

[11] Carmicino C. and Sorge A. R. "Role of Injection in Hybrid Rockets Regression Rate Behavior." In: *Journal of Propulsion and Power* 21.4 (2005).

[12]   Carmicino C. and Sorge A. R. "Influence of a Conical Axial Injector on Hybrid Rocket Performance." In: *Journal of Propulsion and Power* 22.5 (2006).

[13]   Hammock W. R. Jr., Currie E. C. and Fisher A. E. *APOLLO EXPERIENCE REPORT - DESCENT PROPULSION SYSTEMt*. Tech. rep. NASA, 1973.

[14]   Altman D. and Humble R. *Hybrid rocket Propulsion Systems in Space Propulsion Analysis and Design*. Space Technology Series. McGraw Hill, 1995.

[15]   Faenza M., Moretto F. , Tijsterman R., Popela R., Dvorak P., Petronio D. and Pavarin D. "Experimental Characterization of a Cavitating Pintle Valve with H2O2." In: *4th AAF/ESA/CNES Space Propulsion Conference*. Cologne, Germany, May 2014.

[16]   Jones C. C., Myre D. D. and Cowart J. S. "Performance and Analysis of Vortex Oxidizer Injection in a Hybrid Rocket Motor." In: *45th AIAA/ASME/SAE/ASEE Joint Propulsion Conference & Exhibit*. Denver, CO, USA, August 2009.

[17]   Paccagnella E., Barato F., Pavarin D. and Karabeyoglu A. M. "Scaling Parameters of Swirling Oxidizer Injection in Hybrid Rocket Motors." In: *Journal of Propulsion and Power* 33.6 (2017), pp. 1378–1394.

[18]   Penn C. D. and Branigan J. E. *Preliminary Flight Rating Tests of the HAST Propulsion System*. Tech. rep. AFRPL-TR-15-5, 1975.

[19]   Penn C. D. and Branigan J. E. *AQM-81A Firebolt, Tactical Air Command Technical Report*. Tech. rep. Langley AFB VA, 1983.

[20]   Whitmore S. A., Merkley S. L., Walker S. D. and Spurrier Z. S. "Throttled Launch-Assist Hybrid Rocket Motor for an Airborne NanoSat Launch Platform." In: *51st AIAA/SAE/ASEE Joint Propulsion Conference*. Orlando, FL, USA, July 2015.

[21]   Pastrone Dario. "Approaches to Low Fuel Regression Rate in Hybrid Rocket Engines." In: *International Journal of Aerospace Engineering* 2012.1 (2012).

[22]   Austin B. L., Heister S. D., Dambach E. M., Meyer S. E. and Wernimont E. J. "Variable Thrust, Multiple Start Hybrid Motor Solutions for Missile and Space Applications." In: *46th AIAA/ASME/SAE/ASEE Joint Propulsion Conference & Exhibit*. Nashville, TN, USA, July 2010.

[23]   Barato F., Paccagnella E. and Pavarin D. "Explicit Analytical Equations for Single Port Hybrid Rocket Combustion Chamber Sizing." In: *53rd AIAA/SAE/ASEE Joint Propulsion Conference*. Atlanta, GA, USA, July 2017.

[24]   Marxman G. A. , Wooldridge C. E. and Muzzy R. J. "Fundamentals of Hybrid BoundaryLayer Combustion." In: *Progress in Astronautics and Aeronautics* 15 (1964).

[25]   Barato Francesco. "Numerical and Experimental Investigation of Hybrid Rocket Motors Transient Behavior." PhD thesis. CISAS: Space Sciences, Technologies and Measurements, 2013.

[26] Sanford Gordon and Bonnie J. McBride. *Computer Program for Calculation of Complex Chemical Equilibrium Composition and Application*. NASA Reference Publication 1311. October 1994.

[27] Schnerr G. H. and Sauer J. "Physical and Numerical Modeling of Unsteady Cavitation Dynamics"." In: *Fourth International Conference on Multiphase Flow*. New Orleans, LA, USA, 2000.

[28] Nakagawa I. and Nikone S. "Study on the Regression Rate of Paraffn-Based Hybrid Rocket Fuels." In: *Journal of Propulsion and Power* 27.6 (November 2011), pp. 1276–1279.

[29] Franklin B. , Mead J. and B. R. Bornhorst. *Certification Tests of a Hybrid Propulsion System for the Sandpiper Target Missile*. Tech. rep. AFRPL-TR- 69 -73, 1969.

[30] Karabeyoglu M. A., Cantwell B. J. and Zilliac G. "Development of Scalable Space Time Averaged Regression Rate Expressions for Hybrid Rockets." In: *41th Joint Propulsion Conference and Exhibit*. Tucson, AZ, USA, July 2005.

[31] Karabeyoglu M. A., De Zilwa S., Cantwell B. J. and Zilliac G. "Transient Modeling of Hybrid Rocket Low Frequency Instabilities." In: *39th AIAA/ASME/SAE/ASEE Joint Propulsion Conference and Exhibit*. Huntsville, AL, USA, July 2003.

[32] Karabeyoglu M. A., Stevens J., Geyzel D., Cantwell B. J. and Micheletti D. "High Performance Hybrid Upper Stage Motor." In: *47th Joint Propulsion Conference and Exhibit*. San Diego, CA, USA, July August 2011.

[33] Kline S. J. and McClintock F. A. "Describing uncertainties in single-sample experiments." In: *Mechanical Engineering* 75.1 (1953).

[34] Rønningen J. and Husdal J. "Nammo Hybrid Rocket Propulsion TRL Improvement Program." In: *48th AIAA/ASME/SAE/ASEE Joint Propulsion Conference & Exhibit*. Atlanta, GA, USA, July August 2012.

[35] Schmierer C., Kobald M., Steelant J. and Schlechtriem S. "Hybrid Propulsion for a Moon Sample Return Mission." In: *Space Propulsion 2018*. Seville, Spain, May 2018.

[36] Yuasa S., Yamamoto K., Hachiya H., Kitagawa K. and Oowada Y. "Development of a small sounding hybrid rocket with a swirling-oxidizer-type engine." In: *37th Joint Propulsion Conference and Exhibit*. Salt Lake City, UT, USA, July 2001.

[37] Ashley Karp, Barry Nakazono, Joel Benito Manrique, Robert Shotwell, David Vaughan, and George T. Story. "A Hybrid Mars Ascent Vehicle Concept for Low Temperature Storage and Operation." In: *52nd AIAA/SAE/ASEE Joint Propulsion Conference*. Salt Lake City, UT, USA, July 2016.

[38]   Boardman T.A., Carpenter R. L. and Claflin S.E. "A Comparative Study of the Effects of Liquid Versus Gaseous - Oxygen Injection on Combustion Stability in 11-inch-Diameter Hybrid Motors," in: *33rd Joint Propulsion Conference and exhibit*. Seattle, WA, USA, July 1997.

[39]   Cherne Jack M. *MECHANICAL DESIGN OF THE LUNAR MODULE DESCENT ENGINE*. Tech. rep. TRW System.

[40]   Chiaverini M. "Review of Solid Fuel Regression Rate Behavior in Classical and Non classical Hybrid Rocket Motors." In: *Fundamentals of Hybrid Rocket Combustion and Propulsion*. Ed. by Chiaverini M. J. and Kuo K. K. Vol. 218. Progress in Astronautics and Aeronautics. Reston VA: AIAA, 2007.

[41]   Grosse M. "Design Challenges for a Cost Competitive Hybrid Rocket Booster." In: *2TH EUROPEAN CONFERENCE FOR AERONAUTICS AND AEROSPACE SCIENCES*. Brussel, Belgium, July 2007.

[42]   Petrarolo A. , Kobalt M. and Schlechtriem S. "Optical Analysis of the Liquid Layer Combustion of Paraffin-based Hybrid Rocket Fuels." In: *7TH EUROPEAN CONFERENCE FOR AERONAUTICS AND AEROSPACE SCIENCES*. July 2017.

[43]   Pugibet M. and Moutet H. "Utilisation dans les systèmes hybrides de l'eau oxygénée come comburant: On the use of hydrogen peroxide as oxidizer in hybrid systems." In: *La Recherche Aerospatiale* 132 (1969), pp. 15–31.

[44]   Ruffin A., Barato F., Santi M., Paccagnella E., Bellomo N., Miste G. A., Venturelli G. M. and Pavarin D. "Development of a Cavitating Pintle for a Throttleable Hybrid Rocket Motor." In: *7th European Conference for Aerospace Sciences EUCASS*. Milan, Italy, July 2017.

[45]   Ruffin A., Santi M., Paccagnella E., Barato F., Bellomo N., Miste G. A., Venturelli G. M. and Pavarin D. "Development of a Flow Control Valve for a Throttleable Hybrid Rocket Motor and Throttling Fire Tests." In: *2018 Joint Propulsion Conference*. Cincinnati, OH, USA, July 2018.

[46]   Karabeyoglu M.Arif. "Transient combustion in hybrid rockets." PhD thesis. Stanford University, Deptartment of Aeronautics and Astronautics, Stanford, 1998.

[47]   Faenza Martina. "Numerical and Experimental Characterization of Throttleable Hybrid Propulsion Systems." PhD thesis. CISAS: Space Sciences, Technologies and Measurements, 2014.

[48]   Randall L. N. "Rocket Applications of the Cavitating Venturi." In: *American Rocket Society*. Toronto, Canada, June 1951.

[49]   Sheng Z. Cai G., Tian H., Yu N. and Zeng P. "Experimental tests of throttleable H2O2/PE hybrids." In: *51st AIAA/SAE/ASEE Joint Propulsion Conference*. Orlando, FL, USA, July 2015.

[50] Tian H., Zeng P., Yu N and Cai G. "Application of variable area cavitating venturi as a dynamic flow controller." In: *Flow Measurement and Instrumentation 38*. May 2014.

[51] Zeng P., Tian H., Yu N. and Cai G. "Numerical Simulation on Flow in the Variable Area Cavitating Venturi." In: *49th AIAA/ASME/SAE/ASEE Joint Propulsion Conference*. San Jose, CA, USA, July 2013.

[52] Bellomo Nicolas. "Analysis Of Variable Thrust Hybrid Propulsion For Formation Flight Satellites." PhD thesis. CISAS: Space Sciences, Technologies and Measurements, 2012.

[53] Duban P. "The LEX rocket probe (LEX small rocket probe for in-fight testing of ONERA studies of hybrid propulsion, discussing design and program." In: *L'Aeronautique et L'Astronautique* (1968).

[54] Casiano M. J., Hulka J. R. and Yang V. "Liquid-Propellant Rocket Engine Throttling: A Comprehensive Review." In: *45th Joint Propulsion Conference and exhibit*. Denver, CO, USA, August 2009.

[55] Boardman T.A., Abel T.M. , Claflin S.E. and Shaeffer C.W. "Design and test planning for a 200 klbf thrust hybrid rocket motor under the hybrid propulsion demonstration program." In: *33rd Joint Propulsion Conference and exhibit*. Seattle, WA, USA, July 1997.

[56] Whitmore S.A., Peterson Z. W. and Eilers S. D. "Closed-Loop Precision Throttling of a Hybrid Rocket Motor." In: *Journal of Propulsion and Power* 30.2 (2014), pp. 325–336.

[57] Parissenti Guido, Pessana Mario et al. "Throttleable hybrid engine for planetary soft landing." In: *4th European Conference for Aerospace Sciences EUCASS*. Saint Petersburg, RU, July 2011.

DECLARATION

I declare that this thesis has been composed solely by myself and that it has not been submitted, in whole or in part, in any previous application for a degree. Except where states otherwise by reference or acknowledgment, the work presented is entirely my own.

The data presented in this thesis was obtained in experiments carried out by the University of Padova Hybrid Propulsion Group at the experimental test facility of Voltabarozzo. I played a major role in the preparation and execution of the experiments, and the data analysis and interpretation are entirely by own work.

Padova, September 2018

———————————————————

Alessandro Ruffin

ACKNOWLEDGMENTS

RINGRAZIAMENTI

Vorrei ringraziare tutte le persone che mi hanno permesso di e mi hanno aiutato a sviluppare quella serie di abilità tecnico-scientifiche che mi rendono oggi un Ingegnere e una persona migliore rispetto a quello che ero tre anni fa. Ringrazio il mio comitato della tesi:

Il Professor Giampiero Naletto direttore della Scuola di Dottorato del CISAS per la perseveranza e passione con cui dirige e manda avanti la scuola di dottorato.

Il mio Supervisore e collega Ing. Francesco Barato (Cisque) che mi ha seguito in questi tre anni e pienamente consapevole della sua posizione ha svolto un ottimo lavoro.

Il mio Co-Supervisore e coordinatore del gruppo di propulsione spaziale dell'Università degli Studi di Padova, il Professor Daniele Pavarin. Di lui continuo ad apprezzare l'entusiasmo e la passione per le attività che svolgiamo e l'umanità con cui svolge il suo lavoro

Ringrazio l'Ingegner Nicolas Bellomo (Nic) con cui ho avuto l'onore di lavorare a stretto contatto e imparare il mestiere con tutta la meticolosità e precisione richiesta dal caso.

Ringrazio i miei colleghi dottorandi Marco Santi e Enrico Paccagnella con cui ho avuto il piacere e l'onore di lavorare fianco a fianco.

Ringrazio coloro che in questo periodo sono arrivati e sono partiti: Giangi, Giò, Gela, Laura e Guerra.

Ringrazio coloro che "bazzicano" per il cannone a cui occasionalmente ho chiesto e ricevuto sempre le loro opinioni professionali: Marco, Fabio, Paola, Mirko e Selmo.

Ringrazio anche quei fornitori non convenzionali per il loro contributo/aiuto la loro simpatia ed onestà: Scapin, Giacometti e Canevarolo.

Infine voglio porgere un ringraziamento non professionale alla mia famiglia e ai miei amici: Laura, Lucio, Leo, Giulia, Marco, Diego, Gloria, Davide, Irene, Alberto, Miriam e Gianluca.